MODELING AND ANALYSIS OF CHEMILUMINESCENCE SENSING FOR SYNGAS, METHANE AND JET-A COMBUSTION

A Dissertation
Presented to
The Academic Faculty

by

Venkata Narasimham Nori

In Partial Fulfillment
of the Requirements for the Degree
Doctor of Philosophy in the
School of Aerospace Engineering

Georgia Institute of Technology
August 2008

MODELING AND ANALYSIS OF CHEMILUMINESCENCE SENSING FOR SYNGAS, METHANE AND JET-A COMBUSTION

Approved by:

Dr. Jerry M. Seitzman, Advisor
School of Aerospace Engineering
Georgia Institute of Technology

Dr. Suresh Menon
School of Aerospace Engineering
Georgia Institute of Technology

Dr. Greg Huey
School of Earth and Atmospheric Sciences
Georgia Institute of Technology

Dr. Timothy C. Lieuwen
School of Aerospace Enginnering
Georgia Institute of Technology

Dr. Jechiel I. Jagoda
School of Aerospace Engineering
Georgia Institute of Technology

Dr. Nicolas Docquier
Combustion Group
Air Liquide

Date Approved: June 5th 2008

To the One and only One; to the One without a second!
To that from which all objects have come, that in which all objects exist and
that into which all objects merge during destruction!
To the One who is the Ear of the ear, the Mind of the mind, the Speech of speech,
the Life of life and the Eye of the eye!

-The Upanishads

ACKNOWLEDGEMENTS

It fills me with deep sense of gratitude and humility, for this achievement would not have been possible without the support of many beautiful and wonderful people. This is especially true with my advisor who not only had to take the risk of choosing me but also had the additional responsibility of motivating me and making me do things. I simply have no words to thank him enough for providing me a new lease of life, for his support, encouragement and loving guidance. In this regard, I should also mention about my undergraduate advisor, Dr. R. I. Sujith, for his concern and interest in my welfare and for providing me the special boost to start my graduate studies at Georgia Tech.

I would like to thank Dr. Jechiel Jagoda, Dr. Tim Lieuwen, Dr Suresh Menon, Dr. Nicolas Docquier and Dr. Greg Huey for being part of my thesis reading committee and for providing valuable comments and suggestions to improve the quality of my thesis. I would like to specially thank Dr. Greg Huey for accepting to be a part of my thesis committee, in a very short notice. I would also like to take this opportunity to thank my future boss, Dr. Docquier for being very understanding, patient and supportive during the "turbulent" times of my manuscript writing.

I would like to thank all the "people on fire" of the Georgia Tech combustion lab for their help, encouragement and for "keeping the flame burning" in the lab with their enthusiasm. It is with great joy that I would like to introduce my friends (of course, the list is not exhaustive) - JP, Yash,, Nelson, Priya, Thao, Qingguo, Murgi, Surki, Rara, Bobba, Preetham, Santosh S, Santosh H who made my stay at Tech very memorable and full of fun. I would like to thank them all for their help and, teaching me many interesting

things from life to “lift-offs”. I would also like to thank JP for helping me design experiments and for all the interesting discussions. I would also like to sincerely thank Yash for helping me take the high pressure data and, he along with Prabhakaran added color to my nights during the last few busy months of my stay at Tech. I would also like to thank Anne for providing me great starts for the day with her cheerfulness, whenever I slept in the lab. It would be incomplete if I did not thank the many unknown faces who helped me in this journey, called life; for example, the homeless man in the centennial park, who lifted my spirits one day, with his attitude towards life and insightful talk.

I don’t know how to thank my spiritual guide, Parthasarathi Rajagopalachari, who transformed my life, altogether. I practice “Sahaj Marg” meditation under his guidance and it is helping me immensely to develop the correct attitudes to live life happily. I would also like to thank all the members of the Molena retreat center for their love and companionship that I relished every weekend.

My sincere thanks to my roommate Madhav for all the fun we had at home. I heart fully thank Shilpa for her understanding and loving encouragement. I also thank my best buddy SV for his apt and loving suggestions, whenever necessary. I reserve my deepest wishes for my parents and family for their love and inspiration, throughout my life. Coming to the climax of this never ending story, I arrive at the cause of it all: Mr. Creator, who set this up (actually everything) for me…the plot, the theater, the characters, the special effects etc. What can I say…I can only love Him whole heartedly!

TABLE OF CONTENTS

LIST OF TABLES

LIST OF FIGURES

SUMMARY

Naturally occurring flame chemiluminescence, the radiative emission from electronically excited species that are formed in chemical reactions, has received increasing attention for its potential sensor and diagnostic applications in combustors. Since these species are mainly produced in the reaction zone, chemiluminescence can be indicative of the reacting conditions in the flame. A number of studies have used flame chemiluminescence to monitor flame status, and combustor performance. Most of these studies have been experimental, with the relationship between the chemiluminescence and the combustion state determined empirically. However, chemiluminescence modeling has the potential to provide a better understanding of the chemiluminescence processes and their dependence on various combustion operating conditions.

The primary objective of this research was to identify and validate the important chemiluminescence reaction mechanisms for OH*, CH* and CO_2*. To this end, measurements were performed at various operating conditions, primarily in laminar, premixed flames, fueled with methane, syngas (H_2/CO) and Jet-A. The results are compared to 1-d laminar flame simulations employing the chemiluminescence mechanisms. The secondary objective was to use the experiments and validated chemiluminescence reaction mechanisms to evaluate the usefulness of flame chemiluminescence as a combustion diagnostic, particularly for heat release rate and equivalence ratio.

The validation studies were able to identify specific mechanisms for OH*, CH* and CO_2* that produced excellent agreement with the experimental data in most cases.

The mechanisms were able to predict the variation of the chemiluminescence signals with equivalence ratio and, in most cases, preheat but not the variation with pressure. This is attributed in part to inaccuracies in the basic chemical mechanism used in the simulations to predict concentration profiles of the chemiluminescence precursor species. For CH*, lack of accurate quenching data may also contribute. For OH*, thermal excitation and radiative trapping may also be problematic at high pressure, especially near stoichiometric conditions. For CO_2*, trapping and interference from the emissions of other species (such as HCO and H_2O) lead to discrepancies between experiments and simulations at high pressure and in Jet-A flames.

Regarding the utility of chemiluminescence for sensing, a number of observations can be made. It is advisable to use background subtracted chemiluminescence signals for sensing purposes. In syngas-air flames, CO_2* is a reasonable heat release rate marker, at least for very lean conditions, as it is less dependent on equivalence ratio than OH*. For a similar reason, OH* shows some advantage in atmospheric-pressure methane and Jet-A flames in general, while CH* is advantageous at high pressure and very lean conditions at atmospheric pressure. The chemiluminescence intensity ratio CO_2*/OH* is not useful for sensing equivalence ratio in syngas flames, except maybe at very lean conditions. However, the CH*/OH* signal ratio is a promising approach for sensing equivalence ratio at low or very high pressure conditions in hydrocarbon flames. Thermal excitation and self-absorption processes for OH* chemiluminescence can become important for combustors operating at high pressure, high preheat and near stoichiometric conditions.

CHAPTER 1

INTRODUCTION

1.1 Motivation

Monitoring and controlling combustor performance and health is a major challenge because of the harsh environment within the combustor. For understanding combustion and ocmbustors, the spatial and temporal distribution of parameters such as temperature, pressure, equivalence ratio, heat release rate and pollutant levels are of great interest. Robust and reliable diagnostic and sensor systems are even more relevant to future combustors due to the many issues facing modern lean, premixed combustors and the fuel-flexible versions under development. For example in lean premixed combustors, monitoring and control of the combustor operating point is necessary to harness the full benefits of NOx reduction. That these combustors operate near the lean stability limit with the flame more prone to blowout and combustion dynamics further motivates the need for robust control and sensing methodologies. To this end, optical methods have become a popular choice because the measurements are non-intrusive and there are optical interface materials can survive the high temperatures combustor environment. Optical sensors have the added advantage of being quite fast and capable of giving both localized and global information about the combustion process. The fast response of these sensors is particularly useful in monitoring dynamic processes in combustion systems. However, most of the quantitative methods are laser-based, with higher costs, complexity, and maintenance requirements.

Flame chemiluminescence has received renewed attention for its potential sensor applications in combustors. The radiative emissions from electronically excited species that are formed chemically, such as CH*, OH*, C_2* and CO_2* constitute the primary sources of chemiluminescence in hydrocarbon flames [1]. Since these species are mainly produced in the reaction zone, chemiluminescence can be indicative of the reacting conditions in the flame. This idea has led many to explore the use of flame chemiluminescence in practical combustors to monitor flame status, and combustor health and performance. For example, chemiluminescence imaging of excited radicals, an obvious application, is often used for reaction zone marking [2, 3]. Similarly, the ratio of emissions from excited species, such as CH*/OH* or C_2^*/OH^*, show promise for equivalence ratio sensing in both gaseous and liquid fuel systems [4]. For example, it has

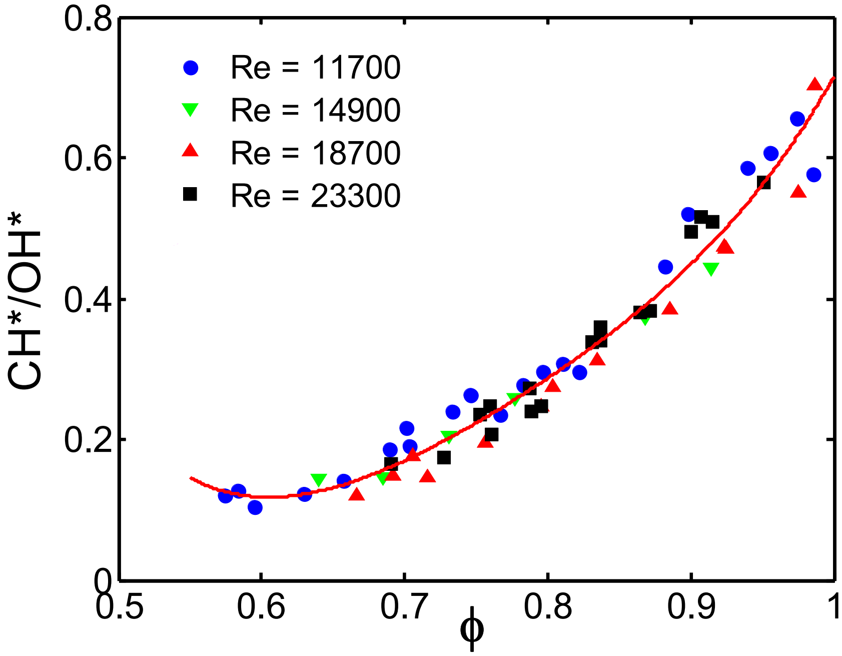

Figure 1.1. Variation of CH^*/OH^* chemiluminescence intensity ratio on equivalence ratio for various inlet axial Re in a swirl combustor [4].

been observed that the ratio of CH*/OH* peak intensities monotonically increases with equivalence ratio in methane flames at atmospheric conditions (Figure 1.1) [4], and hence could be used for sensing equivalence ratio at these conditions. Chemiluminescence has also been employed to characterize temporal fluctuations in global heat release rate and its spatial distribution for applications related to combustion instabilities [5].

Nevertheless, most of these studies have been experimental, with the relationship between the chemiluminescence and the combustion state determined empirically. Thus the relationship between chemiluminescence signals and combustion parameters must be experimentally revisited whenever the operating conditions change in a significant way. Chemiluminescence modelling on the other hand has the potential to provide a better understanding of the chemiluminescence processes and their dependence on various combustion operating conditions. Modeling provides better control for isolating and studying the conditions of interest compared to experiments. Modeling can also be helpful in designing a diagnostic or sensing approach, and interpreting experimental results. The success of the model mainly depends on the accuracy of the reaction mechanisms for the formation of the excited-state species and the associated reaction rates, assuming that the chemiluminescence precursor species are well-estimated by standard combustion models for the particular fuel-oxidizer system of interest. Thus, most of the earlier modeling efforts were intended to identify the chemiluminescence reactions and their rates [6,7] or to understand the relationship between chemiluminescence and flame properties [8,9] using proposed chemiluminescence mechanisms that were not systematically validated. Additionally, these studies examined OH^*, CH^* and C_2^* primarily in methane-air flames. In the case of CO_2^*

chemiluminescence, its relevance to determination of flame properties such as heat release in laminar and turbulent premixed flames was evaluated by Samaniego *et al*. [10] via a numerical investigation without experimental validation using outdated rate constant information for CO_2^* chemiluminescence.

Thus, the objective of this thesis is to identify and validate the important chemiluminescence reactions for OH*, CH* and CO_2* and to study the dependence of flame chemiluminescence on combustion parameters such as pressure, reactant preheat, equivalence ratio, strain and the degree of reactant/product mixing for a range of relevant fuels: methane, syngas and Jet-A. Thus the proposed work will provide direction on the potential sensor applications of flame chemiluminescence. Methane and syngas fuels were chosen in part because of the availability of validated mechanisms, such as GRI Mech 3.0, and because of the extensive application of natural gas in industrial applications, and the great interest in syngas and CH_4/H_2 mixtures for future applications. Jet-A was chosen due to its importance in aircraft engines, and because it involves a significant increase in fuel-chemistry complexity over the other choices.

1.2 Literature Review

Equivalence ratio is one of the important engine parameters that needs to be monitored and controlled both globally and locally, for variations in fuel-air ratio could lead to undesirable consequences such as increased NOx and soot emissions, reduced flame stability and ultimately combustor (acoustic) instabilities that may be detrimental to the .structural integrity of the combustor itself. In this regard, a number of studies in the 1950's [11-13] have laid the foundation for sensing this important parameter among others (such as heat release rate) using flame chemiluminescence. For example, Clark

[13] investigated the dependence of chemiluminescence signals of OH*, CH*, C_2* and CO_2* on fuel type, flow rate and equivalence ratio. It was showed that the ratio of C_2*/CH* chemiluminescence signal intensities could be used for monitoring equivalence ratio in propane-air and ethylene-air flames. Recent studies in both premixed and partially premixed gaseous and liquid fuel systems [4, 14-19] have strengthened the promise for equivalence ratio sensing via ratio of emissions such as CH*/OH* or C_2^*/OH^*. However, these studies only reported empirical correlations for a specific burner and detection system, which may not be generally applicable. Additionally, most of the studies considered flows with simultaneous variations of strain rate, temperature or pressure in addition to equivalence ratio, further limiting the relevance of the findings.

Chemiluminescence emission from OH*, CH*, CO_2* and C_2* have been studied in laminar and turbulent flames, and since the early days it was assumed to be a marker and measure for heat release rate [13]. This was due to the observation that radiation intensity increased linearly with fuel flow rate in both laminar and low-intensity turbulent flames, for other conditions fixed, e.g., at a given equivalence ratio or reactant temperature. This assumption was further strengthened by the work of Price *et al.* [20] and Hurle *et. al* [21] in ethylene-air, turbulent, premixed and diffusion flames when they observed excellent correlation between the time derivative of the C_2* and CH* chemiluminescence light signal strength and the root mean square pressure, as measured by a microphone some distance away from the flame. Subsequent studies used this hypothesis without additional evaluation of the influence of combustion parameters (i.e., equivalence ratio, pressure, temperature, and flame strain rate) on the chemistry of the excited radicals leading to chemiluminescence and its potential link to heat release [22, 23]. This correlation between chemiluminescence rate and acoustic pressure was later verified in laminar flames in steady and unsteady combustion under moderate strain, for fixed conditions such as equivalence ratio, pressure, temperature, and flame strain rate [10,,25]. However in highly turbulent flames or regions with extreme local strain or flame curvature, chemiluminescence can effectively go to zero without flame extinction [26-28]. Hence, the assumption severely fails in such situations and flame chemiluminescence would not be reliable for heat release rate marking.

Thus while flame emission has been used to characterize temporal fluctuations both in overall heat release rate and the spatial distribution of local heat release rate [5,29], care must be taken when interpreting such measurements. For example, when making overall chemiluminescence measurements, it is important to realize that changes in the fuel flow rate and changes in the equivalence ratio independently affect the overall chemiluminescence emission. So, it can be necessary to measure both fuel flow rate and equivalence ratio oscillations to get accurate information about the phase and amplitude of the overall heat release rate fluctuations [28].

As noted previously, these relationships could be studied in detail if validated mechanisms for OH*, CH* and CO_2* chemiluminescence were available. The required mechanism should account for the formation and destruction of the excited state species. There has been considerable work identifying the formation reactions and their rate parameters for OH* and CH*. For these two species, there have been a number of experimental studies in premixed methane air systems including some at high pressure [19,,31] and with purposefully applied strain [30,24]; yet few have focused on validating the chemiluminescence mechanisms [32]. In addition, most of these studies were limited to methane-air mixtures and room temperature conditions. In summary, there is a need for a parametric study over a range of operating conditions such as fuel type, reactant temperature, pressure, dilution, strain, and equivalence ratio on the behavior of flame chemiluminescence, and its relation to heat release rate and equivalence ratio. Such a study would help provide insight into the dependence of chemiluminescence on these parameters and improve interpretation of experimental data.

1.3 Overview of Present Work

The main objective of this thesis is to develop a predictive model for flame chemiluminescence from three sources: OH*, CH* and CO_2*. The secondary objective is to use the validated chemiluminescence reaction models to evaluate the usefulness of flame chemiluminescence as a combustion diagnostic at various operating conditions for gaseous and liquid fuels of importance: viz. methane, syngas and Jet-A.

The approach taken to accomplish the first objective is to evaluate mechanisms and rates identified in the literature for OH*, CH* and CO_2* by comparing the global chemiluminescence yield measured in flame experiments to that predicted by the models. Identifying the appropriate mechanisms includes a literature review of the proposed chemiluminescence formation reactions and their associated rate parameters, as well as identification of the important collisional quenchers and their corresponding rate parameters. For the verification task, it is essential to perform experiments at a range of controlled operating conditions, including: pressure, reactant preheat temperature, equivalence ratio and reactant dilution. The studies are primarily carried out in simple laminar premixed flames, which provide a well-controlled environment for measuring global flame chemiluminescence. They are also more amenable to simulation. Then, the chemiluminescence models are validated by comparing the experiments to simulation results. The simulations are performed for unstrained laminar flames with leading chemical kinetic mechanisms relevant to the above fuels, and the global chemiluminescence yield is calculated using the available chemiluminescence reactions and their rates. The approach to the second objective involves using the validated chemiluminescence models to study the dependence of flame chemiluminescence on combustion parameters such as pressure, reactant preheat, strain equivalence ratio and degree of reactant/product mixing in the above fuels.

The general thesis outline is as follows: Chapter 2 provides necessary background information about flame chemiluminescence and chemiluminescence mechanisms for OH*, CH* and CO_2* excited species including their formation reactions and quenching reactions with their associated rate parameters from the literature. Chapter 3 describes the experimental facilities used in this study, including the burners and the optics necessary for acquiring flame chemiluminescence. Additionally, details of the chemiluminescence modeling approach used to estimate global chemiluminescence yield from the flames are presented in this chapter. The comparisons between the model predictions and experiments are made in Chapter 4 and the most appropriate models are evaluated for OH*, CH* and CO_2* chemiluminescence. The validated models are then used in Chapter 5 to evaluate flame chemiluminescence from these species, for sensing equivalence ratio and heat release rate in premixed flames of a representative syngas mixture and methane at various operating conditions. This chapter also provides estimates of the contribution of thermally produced OH* to the total OH* signal in these flames. The chapter also examines the implications for chemiluminescence sensing if total signals are considered, without background subtraction, simulating chemiluminescence acquired by “single” wavelength detection systems. Finally, Chapter 6 concludes the thesis with a summary and recommendations for further studies.

CHAPTER 2

BACKGROUND

This chapter provides a brief overview of chemiluminescence and the reaction mechanisms responsible for it. In particular, formation reactions, quenching reactions and their appropriate rate parameters established in the literature are presented for OH*, CH* and CO_2*.

2.1 Chemiluminescence

Chemiluminescence, as the name suggests, is the light that is produced as a result of chemical reaction. In other words, it is the spontaneous electromagnetic radiation that is produced when chemically created excited states return to a lower energy state (ground state generally) [1]. Chemiluminescence forms a part of the wider domain of emission spectroscopy. In this thesis, flame emission mainly in the UV-VIS part of the electromagnetic spectrum is considered. In particular, it deals with emission from the excited molecules OH*, CO_2* and CH*. Emission in the visible and ultra-violet regions is generally due to changes in electronic states of the molecule. This change determines the position of the molecular band system as a whole. The position of the individual bands within the band system is determined by the changes in the vibrational energy states of the molecule. The fine line structure of the band (fine structure of the individual bands) on the other hand is determined by the changes in the rotational energy states within the molecule.

The net photon emission due to chemiluminescence from an excited molecule (say OH*) depends on the following steps as illustrated in Figure 2.1: 1) excited state formation via chemical reactions (F), 2) excited state formation via thermal excitation (T), 3) (rapid) collisional quenching reactions that remove the excited state, reducing to its ground electronic configuration non-radiatively (Q), 4) reactive collision with another molecule (R), and 5) spontaneous radiative transitions to the ground state (A).

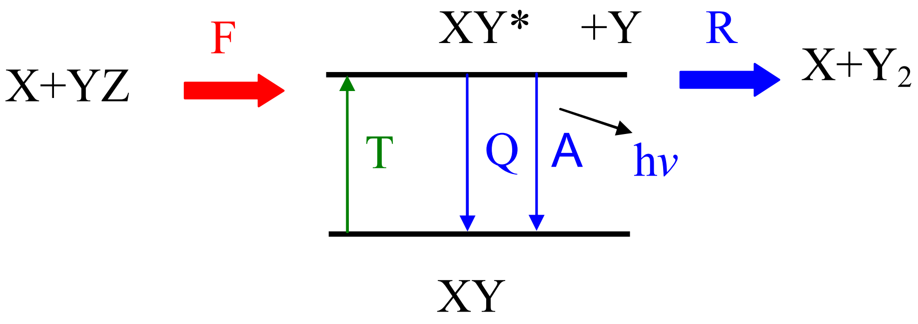

Figure 2.1. General steps involved in a chemiluminescence reaction mechanism.

Often, the whole process is dominated by quenching, with the process limited by formation of the excited state[*]. For these reasons, they can often be assumed to be in quasi-steady state [10], i.e., for an excited state XY^*

$$\frac{d[XY^*]}{dt} \approx 0 = F + T - Q - R - A\,. \tag{1}$$

where F and T represent the production rates of the excited state by chemical and thermal excitation mechanisms; Q, R and A represent the removal rates of the excited state by collisional quenching, reactive quenching, and by spontaneous emission. Thus the

---

[*] This leads to low concentrations for the electronically excited species, which then have little impact on the overall flame chemistry.

concentration of the excited state, [XY*], can be estimated from Eq. (1). The chemiluminescence photon production rate is given by

$$\frac{d[hv]}{dt} = A\,[XY^{*}]\,. \tag{2}$$

The accuracy of chemiluminescence modeling directly depends on the accuracy with which these sub-steps are modeled. All the above steps shall be considered for OH*, CO_2* and CH* chemiluminescence provided that enough information is found in the literature.

2.2 OH* Chemiluminescence

Emission from the electronically excited OH $A^2\Sigma^+$ state (typically denoted OH^* in the flame chemiluminescence literature) near 310 nm is a prominent feature of hydrogen and hydrocarbon flame spectra. OH^* emission and the reactions important in OH^* chemiluminescence have long been studied [33-37]. Collisional quenching and radiative decay rates for OH excited states are largely well known from extensive studies of OH photophysics [38]. For example, the overall Einstein *A* coefficient for the OH $A^2\Sigma^+$ state is given as 1.4×10^6 s^{-1} [38]. It is the formation reactions and rates that have been more difficult to determine.

Experimental efforts to determine the dominant OH* formation steps have primarily taken one of two approaches: 1) flame and 2) shock-tube studies. In flat flame studies of lean and rich (ϕ=1-1.5) $H_2/O_2/N_2$ mixtures [34], the authors assumed partial equilibrium among the flame radicals and were able to conclude that the following three-body reactions were a likely source of the OH* state.

$$O + H + M \rightarrow OH^{*} + M \qquad (R1)$$

$$H + OH + OH \rightarrow OH^{*} + M \qquad (R2)$$

However, the equilibrium relationships between the radicals prevented the assignment of a unique excitation mechanism for OH* formation. Shock tube studies with $H_2/O_2/Ar$ mixtures were undertaken so as to make kinetic measurements far from equilibrium. Most of these studies [36,37,39] strongly indicated that (R1) was the main source of OH* in hydrogen systems. Still, Smith *et al.* [40] suggested an optimized model taking into account both reactions R1 and R2 for hydrogen combustion.

Many of these flame and shock tube studies also attempted to estimate the rate constants for the OH* formation reactions. Because of the more controlled nature of the shock tube studies, their results may be more reliable. In most of these studies, however, the authors reported temperature independent rate constants, with the exception of one shock tube study, where an Arrhenius type rate for R1 was reported [36]. Their rate constant was updated in a later shock tube study [37], though without change in the temperature dependence. It should be noted here that the experimentally determined rate constants are mainly based on OH* chemiluminescence data acquired with detectors coupled to filters with at least full width half maximum (FWHM) of ~10nm.

In combustion of hydrocarbon fuels, OH* formation has been most often attributed to the four-center reaction [1,7, 41-44],

$$CH + O_2 \rightarrow OH^{*} + CO \qquad (R3)$$

with rate constants also usually given without temperature dependence. Kinetic rate parameters for this reaction were determined experimentally, primarily in flames, flow reactors and shock tubes. Recently, the shock tube study of Hall *et al*. [45] was able to provide information on the temperature dependence of this reaction. Table 2.1 summarizes the OH* mechanism and rate constant information, with the rate constant parameters given in a modified Arrhenius form.

Table 2.1. Formation (R) and quenching (Q) reactions and rate constants reported for OH*. Rate coefficients are expressed as $k = A\ T^b \exp(-E_a/RT)$ with E_a in units of cal mol^{-1} and AT^b in cm^{3}mol^{-1}s^{-1} for two body reactions or cm^{6}mol^{-2}s^{-1} for three body reactions (with T in K units).

#	Reaction	A	b	E_a	Ref.
R1	H + O + M ↔ OH* + M	6×10^{14}	0.0	6940	[37]
		3.1×10^{14}	0.0	10,000	[45]
		5.45×10^{12}			[40]
		3.63×10^{13}			[43]
		1.2×10^{13}	0.0	6940	[36]
R2	H + OH + OH ↔ OH* + H_2O	1.45×10^{15}			[40]
R3	CH + O_2 ↔ OH* + CO	3.24×10^{14}	-0.4	4150	[45]
		1.8×10^{11}			[43]
		3.72×10^{10}	0	167.2	[44]
$Q1_{OH}$	OH* + H_2O → OH + H_2O	5.92×10^{12}	0.5	-861	[38]
$Q2_{OH}$	OH* + CO_2 → OH + CO_2	2.75×10^{12}	0.5	-968	[38]
$Q3_{OH}$	OH* + CO → OH + CO	3.23×10^{12}	0.5	-787	[38]
$Q4_{OH}$	OH* + H_2 → OH + H_2	2.95×10^{12}	0.5	-444	[38]
$Q5_{OH}$	OH* + O_2 → OH + O_2	2.10×10^{12}	0.5	-482	[38]
$Q6_{OH}$	OH* + OH →OH + OH	1.50×10^{12}	0.5	0.0	[36]
$Q7_{OH}$	OH* + H → OH + H	1.50×10^{12}	0.5	0.0	[36]
$Q8_{OH}$	OH* + O → OH + O	1.50×10^{12}	0.5	0.0	[36]
$Q9_{OH}$	OH* + N_2 → OH + N_2	1.08×10^{11}	0.5	-1238	[38]
$Q10_{OH}$	OH* + CH_4 → OH + CH_4	3.36×10^{12}	0.5	-635	[38]

It can be seen from Table 2.1 that the R1 rate constant (k_1) reported in. the literature at 1800K varies from 1.72×10^{12} to 8.62×10^{13} cm^3/mol·s, i.e., a variation of approximately 50 times. However, if the most recent rates for R1 are considered, k_1 would vary less, between 5.45×10^{12} and 8.62×10^{13} at 1800 K. Nevertheless, k_1 given in [40] should not be considered as it was lowered to accommodate the contribution of R2 in that study. So, finally k_1 would just vary by ~3 times from 3.63×10^{13} to 8.62×10^{13} at 1800 K, if only recent rates for R1 are considered. Similarly, it can be seen that the rate constant of R3 as reported in literature varies from 3.55×10^{10} to 5×10^{12} $cm^3/mol\cdot s$ at 1800 K. It should be noted that the discrepancy in the absolute rate constant of R1 is lesser than that of R3.

Another important difference between the models is the activation energy assigned for the reactions R1 and R3, which directly impacts the temperature dependence of the reaction rate constants. It should be noted, however, that the activation energy for R1, cited by the various sources is not very high. This implies that the reaction rate constant has weak temperature dependence except at low temperatures (for example, found in flames of lean equivalence ratios). The same is applicable for R3 also.

Table 2.1 also lists the primary quenching collisions in simple $H_2/CO/CH_4$ flames. In lean methane flames with air as the oxidizer, H_2O is the most effective quencher, while CO, CO_2 and O_2 are also important. However, in complex fuel systems such as Jet-A, there might be other quenchers such as alkanes, alcohols and aromatics as they are large molecules that may have significant quenching cross-sections. However, there is little research regarding the OH* quenching rates by these molecules. Another path of destruction of OH*, by chemical reaction, is possible. For example, in the case of H_2 [46-48],

$$OH^* + H_2 \rightarrow H + H_2O$$

Experiments have shown that break up of the $OH(A^2\Sigma^+)$-H_2 Van der Waals cluster produced a significant yield of H atoms [47]. In fact, most recent results conclude that only a small fraction of the products, less than 15%, arise from nonreactive quenching while reactive quenching is the dominant product channel [48]. This approach is expected to be applicable to the collisional quenching of OH* by other partners (H_2O, CO_2 etc.) and for collisional quenching of other excited state species (for example, CH*) as well. The authors speculate that reactive quenching may be the norm in collisional quenching processes with large cross sections (H_2O etc.) [48]. However to date, reactive quenching of OH* is considered only for H_2 while few older studies have termed this pathway insignificant [43]. This aspect of quenching is not considered in this thesis due to lack of sufficient information.

Absorption of the emitted photon by another ground state OH molecule before it reaches a detector is indirectly related to the whole process and can be estimated using the Beer-Lambert relation given by [49,50],

$$\frac{I}{I_o} = \exp\left(- \int_0^l k_\nu p X_{OH} dl \right). \tag{3}$$

where k_v is the spectral absorbance coefficient, p is the pressure, X_{OH} is the absorbing OH mole fraction and l is the absorbing path length. The absorption coefficient, k_v, is a function of temperature and pressure [49]. It can be seen from Eq. 3 that the absorption is maximum when the product $pX_{OH}l$ is maximum. A numerical study in methane-air flames shows that this case corresponds to atmospheric pressure and near-stoichiometric conditions [31]. In methane-air premixed laminar flames at room temperature for different operating pressures (1-10 atm), the self-absorption was estimated to be a maximum of ~15% by the same authors [31], with the maximum absorption coefficient per unit pressure per unit length in the R-branch bandhead of the OH A-X (0,0) band being ~20$atm^{-1}cm^{-1}$ at similar experimental conditions [50]. Self-absorption in high pressure H_2-air flames may be higher, because of higher molar concentrations of OH.

The chemiluminescence emission from excited OH* can also be absorbed by other molecules other than ground state OH. In fact, in a recent shock tube study, the absorption spectra for CO_2 and H_2O were measured between 190 and 320nm in 900-3050 K temperature range and it was found that both CO_2 and H_2O become significant absorbers in the UV region at high pressure and temperature conditions [51]. The absorption cross-section of CO_2 has strong temperature dependence and increases by 4 orders of magnitude at 193nm between 300K and 2000K with significant absorption by CO_2 extending to wavelengths longer than 300nm at 3000 K. At room temperature and pressure conditions, CO_2 and H_2O (primary combustion products) are nearly transparent in this wavelength region (193-320 nm) and thus have been neglected as a source of potential UV attenuation in combustion diagnostics [52].

Thermal excitation is another way of exciting ground state OH molecules to the $A^2\Sigma^+$ state; though it is often considered negligible compared to the chemiluminescence pathway below 2000 K [36]. In a recent study with opposed flow oxy-methane diffusion flames, it was observed that the thermal excitation becomes the dominant mechanism for OH* production at oxygen contents above 35% [32], due to the high temperatures produced. In fact according to that study, for methane burning in pure oxygen, the thermal excitation is estimated to be more than an order of magnitude greater than the chemical excitation. Thermal excitation increases exponentially with temperature. Assuming OH molecules are in thermal equilibrium at temperature T, the ratio of molecules in the OH-A state to that in the ground state is approximately given by:

$$N_{OH(A)} \big/ N_{OH_{tot}} = 0.5\exp(-47{,}000K/T)\,. \tag{4}$$

With this approximation, the thermal [OH*] profile, and subsequently the spontaneous emission from this OH-A state can be calculated in the flames.

2.3 CO_2* Chemiluminescence

The origin and structure of the CO_2^* "blue continuum" emissions (because most of the light emitted is in the blue region of the electromagnetic spectrum) have also been investigated by various groups. However, its mechanism is probably the least understood when compared to OH* and CH* chemiluminescence. In early studies with $H_2/CO/O_2$ flames, shock tubes, and flow reactors, researchers found that the emission intensity was proportional to the product of [CO] and [O] concentrations and concluded that a reaction similar to (R4) was the primary cause of CO_2^* chemiluminescence [53].

$$CO + O \rightarrow CO_2^* \qquad \text{(R4)}$$

Later in a series of low temperature, flow reactor studies, Pravilov *et al.* [54] identified the likely states involved in CO_2^* chemiluminescence.

$$CO(X^1\Sigma^+) + O(^3P) \rightarrow CO_2(^3B_2)$$
$$CO_2(^3B_2) \rightarrow CO_2(^1B_2)$$
$$CO_2(^1B_2) \rightarrow CO_2(X^1\Sigma^+{}_g) + hv$$
$$CO_2(^1B_2) + M \rightarrow CO_2(X^1\Sigma^+{}_g) + M$$

First an intermediate excited triplet state of CO_2 is formed with the reaction of CO and O in their electronic ground states. The triplet state then rapidly transitions to an excited singlet state. The combination of these two steps is equivalent to (R4). The radiative de-excitation of the single state produces the CO_2^* chemiluminescence, with the radiative decay competing with collision quenching reactions. It is through the first step that the emission rate becomes dependent on the concentrations of [CO] and [O]. This study also found that the CO_2^* continuum has a spectral shape that changes only slightly over a range of temperatures.

None of these studies investigated the individual rates for the detailed CO_2^* mechanism described above and further systematic research has to be done to investigate the effect of various collider molecules such as H_2O and CO_2 on CO_2* chemiluminescence. However, one study claims that collisional quenching of CO_2* chemiluminescence with O_2 is highly temperature dependent and the quenching efficiency decreased by a factor of 35 as temperature increased from 206 to 353 K , and becomes negligible at flame temperatures [54]. Hence, rate constant data have only been reported for the overall rate of chemiluminescence emission at different temperatures and wavelengths. The most recent work is the shock tube study in H_2-CO mixtures and review of previous work by Slack *et al.* [55]. They obtained spectrally resolved emission intensities for wavelengths from 250-700 nm and in the temperature range 1300-2700 K. It should be noted that for higher temperatures, interferences to the CO_2^* continuum emission at wavelengths below 450 nm have been seen in carbon monoxide/oxygen systems due to the radiative combination of oxygen atoms and by the radiation resulting from the electronic excitation of O_2 [56].. Moreover, a similar scenario is possible in hydrocarbon flames where emission from other molecules such as HCO, H_2O can overlap with the UV-VIS continuum [57-59] and the CO_2* chemiluminescence signal may be corrupted. As in the earlier study by Pravilov, Slack *et al.* found only a weak dependence of the spectral shape of the continuum emission on the temperature. Using these results, they determined the spectrally integrated rate expression for the CO_2^* chemiluminescence volumetric photon emission rate (in moles of photons),

$$i_{CO_2^*} = 6.8\times10^5 \exp[\frac{-1950K}{T}][CO][O]\frac{mol}{cm^3 \cdot s} \tag{5}$$

They also showed that this expression extrapolates well to the low temperature data of Pravilov. The magnitude and temperature dependence of this expression is different than the earlier results summarized in [53], which were used in a previous CO_2^* modeling study [10].

2.4 CH* Chemiluminescence

The primary CH* emission in the UV-VIS region is due to the $A^2\Delta\rightarrow X^2\Pi$ (at ~431nm) and $B^2\Sigma^-\rightarrow X^2\Pi$ (~390nm) transitions, with the 431 nm band usually dominating [1]. As was the case with OH*, the CH* chemiluminescence mechanism requires: 1) excited state formation reactions and their rates, and 2) collisional quenching and radiative relaxation rates that remove the excited state. Radiative rates and quenching data for CH* by major species of hydrocarbon combustion are available [38], though the quenching information is not as accurate as that for OH*. Various efforts have explored the CH* formation reactions and their corresponding rate parameters. Of the various proposed sources, research has focused on the following.

$$C_2 + OH \rightarrow CH^* + CO \tag{R5}$$

$$C_2H + O \rightarrow CH^* + CO \tag{R6}$$

$$C_2H + O_2 \rightarrow CH^* + CO_2 \tag{R7}$$

Gaydon [1] suggested reaction R5; this was later challenged, first by Brenig [60] and later by Grebe and Homann [61]. Brenig's experiments suggested that CH* formed from the reaction of ground state ethynyl radicals (C_2H) with O atoms, which had been proposed earlier [62]. A recent shock tube study with methane-hydrogen mixtures supports R5 and R6 as the dominant CH* formation pathways for conditions in the range 1200-2300K and 0.6-2.2 atm [63], though with large uncertainties in the rate parameters due to inadequate information on C_2 kinetics. R5 may also be important in high order hydrocarbon (liquid) fuel systems where C_2 is relatively more abundant. Devriendt *et al.* [64] in a pulsed laser photolysis study at low pressure determined the temperature dependence of R6 and concluded that the majority of CH* is produced by that reaction. Moreover, it was demonstrated that addition of excess O_2 actually decreased the CH* yield in the pulsed laser photolysis [64] and the shock tube studies [63], which eliminated the O_2 step (R7) in the analysis.

However, Renlund *et al.* [65] suggested the importance of C_2H with O_2 rather than atomic oxygen (R6). In a recent flash photolysis study of acetylene at low pressure [66], the temperature dependence of R7 was evaluated; additionally the study concluded that R7 could contribute significantly to CH* chemiluminescence in hot flames and under fuel lean conditions. Absolute excited state concentrations of CH* were measured in low pressure methane-air premixed flames, and rate parameters for R6 and R7 were determined [7] and recently reanalyzed [40]. The R6 rate constant was found to be temperature independent, while R7 showed weak temperature dependence.

In this study, four models proposed in the literature (designated by the last author of the reference source) were used to model CH* formation in methane and Jet-A flames.

Each is based on two of the formation reactions (R5-R7); the reaction rate parameters associated with each are listed in Table 2.2.

Table 2.2. Chemiluminescence reaction mechanism to model CH* formation. Rate coefficients are expressed as $k=AT^b exp(-E_a/RT)$ with E_a in units of cal mol^{-1} and AT^b in cm^{3}mol^{-1}s^{-1} for two body reactions or cm^{6}mol^{-2}s^{-1} for three body reactions (with T in K units). Einstein A coefficient for CH* is 1.85×10^6 s^{-1}[38].

#	Reaction	*A*	*b*	E_a	Ref
R5	$C_2 + OH \leftrightarrow CH^* + CO$	2×10^{14}	0	0	[63]
R6	$C_2H + O \leftrightarrow CH^* + CO$	$2.5(\pm0.8) \times 10^{12}$	0	0	[40]
		5.2×10^{11}	0	2600	[63]
		$1.08(\pm0.4) \times 10^{13}$	0a	0	[64]
		$6.023(\pm3.0) \times 10^{12}$	0	457	[66]
R7	$C_2H + O_2 \leftrightarrow CH^* + CO_2$	$3.2(\pm1.0) \times 10^{11}$	0	1599	[40]
		$2.17(\pm0.8) \times 10^{10}$	0	0	[64]
		6.023×10^{-4}	4.4	-2285	[66]
$Q1_{CH}$	$CH^* + H_2O \leftrightarrow CH +$	5.3×10^{13}	0	0	[38]
$Q2_{CH}$	$CH^* + CO_2 \leftrightarrow CH + CO_2$	2.41×10^{-1}	4.3	-1694	[38]
$Q3_{CH}$	$CH^* + CO \leftrightarrow CH + CO$	2.44×10^{12}	0.5	0	[38]
$Q4_{CH}$	$CH^* + H_2 \leftrightarrow CH + H_2$	1.47×10^{14}	0	1361	[38]
$Q5_{CH}$	$CH^* + O_2 \leftrightarrow CH + O_2$	2.48×10^{6}	2.14	-1720	[38]
$Q6_{CH}$	$CH^* + N_2 \leftrightarrow CH + N_2$	3.03×10^{2}	3.4	-381	[38]
$Q7_{CH}$	$CH^* + CH_4 \rightarrow CH + CH_4$	1.73×10^{13}	0	167	[38]

From the data listed in Table 2.2, the R6 rate constants (k_6) reported in the literature varies from $2.5–10.8\times10^{12}$ cm^3/mol·s at 1800K, i.e., by approximately 4 times. Similarly, the rate constant of R7 as reported in the literature varies from $2.17–24\times10^{10}$ cm^3/mol·s at 1800 K, by approximately 10 times. It should be noted that the discrepancy in the absolute rate constant of R6 is less than that of R7. It is also interesting to note that the ratio of rate constants (k_6/k_7) has a large variation, from 12 to 500 at 1800 K. For two of the models [40, 64], the ratio (k_6/k_7) is almost constant while it decreases by a factor of four in the other model [66] in the temperature range 1400-

1900 K. This has a direct bearing in the relative contributions of R6 and R7 to the CH* chemiluminescence yield.

Table 2.2 also lists the primary collisional quenchers in simple H_2/CO/CH_4 flames. In lean methane-air flames, N_2 is the dominant quencher of CH* while H_2O and CO_2 are also important. However as noted for OH* in complex fuel systems (such as Jet-A), large hydrocarbons may be important. Collisional quenching of excited CH molecule by alcohols and alkane molecules was recently studied in the temperature range 297-653 K [67]. Heptane (C_7H_{16}) and butyl alcohol (C_4H_9OH) were the largest alkane and the alcohol molecules considered. It was found that the quenching rate increased with temperature for the collisional partners studied. It was also observed that the quenching of CH* by some molecules does not follow the Arrhenius relation, the same conclusion as a previous study [68]. It was generally found that the quenching rate constants of CH(A) increases with the number of carbon atoms in the alkane or alcohol molecule. Also, the quenching rate constant of CH(A) with alkane or alcohol is an order of magnitude higher in comparison to that of O_2 [67]. Clearly, this is an important aspect that should be considered when modeling CH* chemiluminescence in higher hydrocarbon flames. Moreover, the CH* quenching with colliders such as N_2 and H_2O that have significant concentrations in typical flames, is not very accurate [38], in spite of a recent investigation [69]. Similarly as in the case of the OH(A) state [46-48], the possibility of reactive quenching of CH(A) state cannot be ruled out, even though the CH(X) state is usually found to be more reactive than the CH(A) state [70]. Unfortunately, very few studies have focused in this area of reactive quenching for CH*.

Absorption of the emitted photon by a ground state CH molecule is also theoretically possible, as was with the excited OH* molecule. However, in typical flame environments, particularly lean systems, the self-absorption mechanism is practically insignificant due to the very low concentration of ground state CH(X) molecules and its occurrence only in the thin reaction zone [31]. In other words, if Eq. (3) was used for CH* self-absorption, both l and X_{CH} are extremely small for ground state CH molecules. Nevertheless, the emitted photons can be absorbed by other molecules such as CO_2 and H_2O [51].

Another mechanism to produce CH* molecules is thermal (collisional) excitation from ground state CH. In a recent study of opposed flow oxy-methane diffusion flames, it was observed that the thermal excitation contributes less than 30% of the total chemiluminescence signal [32]. However, for low oxygen content, thermal production of excited CH (A) molecules is practically negligible. Assuming CH molecules are in thermal equilibrium at temperature T, the ratio of molecules in the CH(A) state to that in the ground state is approximately given by:

$$N_{CH(A)} \big/ N_{CH_{tot}} = \exp(-33{,}401K/T). \tag{6}$$

With this approximation, the thermal [CH*] population, and subsequently the spontaneous emission from the CH(A) state can be calculated. Nevertheless, in most conditions, thermal excitation of ground state CH (X) is negligible compared to that produced chemically. The reasons for this cause are identical to that cited for self-absorption viz. very small concentrations of ground state CH molecules and its occurrence in a narrow region of the flame. It has to be noted that unlike OH, CH does not exist in the product gases for lean combustion and therefore, exists in regions of lower temperature, which further discourages thermal CH* production.

In summary, there is a discrepancy in the information on the formation reactions of the excited state for OH* or CH* and their associated rate parameters, with the quenching reactions and rates known to reasonable accuracy. However for CO_2*, it has to be noted that the only quantitative model in the literature is simplified and does not consider individual formation or quenching reactions and rates. The quasi-steady state assumption for the excited molecules is incorporated in the chemiluminescence modeling approach used here and presented in detail in the next chapter for OH*, CH* and CO_2* chemiluminescence modeling.

CHAPTER 3

MEASUREMENT AND MODELING APPROACHES

The details of the various combustors used for acquiring flame chemiluminescence spectra and the data reduction procedure to extract CO_2*, OH* and CH* chemiluminescence signals from the raw spectrum are described in detail in the first section of this chapter. A brief description of the modeling efforts, the leading kinetic models considered and the procedure for comparing the experimental results with the numerical simulation are discussed in the subsequent section. Finally, various sources of uncertainties associated with the measurements are presented.

3.1 Experimental Setup

Experiments were conducted to validate existing chemiluminescence mechanisms for CO_2*, OH* and CH*. To check the accuracy and robustness of the different mechanisms, experiments were systematically carried out by varying important combustor parameters such as equivalence ratio, pressure, reactant preheat, dilution and fuel type. Each experimental facility employed broadly consists of two subsystems: 1) the burner and 2) the flame chemiluminescence detection system, including collection/imaging optics and detector. The burners are further classified based on the fuel type and the operating pressure. Based on this classification, detailed descriptions of the experimental facilities and the data reduction procedure are presented in the following sections.

3.1.1 Burners

Chemiluminescence spectra were obtained in premixed gaseous (syngas mixtures and methane) and liquid fuel (Jet-A) systems. The gaseous fuels investigated in this study are: 1) H_2-CO syngas system and 2) methane (the primary component of natural gas). Jet-A, a liquid fuel, is relevant in aeropropulsion. The gaseous fuels were studied at atmospheric and elevated pressure, while the Jet-A experiments were limited to atmospheric pressure. Descriptions of the atmospheric facilities are presented first, followed by the elevated pressure facility.

3.1.1.1 Atmospheric Pressure

Atmospheric experiments with syngas mixtures were conducted in a facility that was previously used for laminar flame speed measurements [71] as shown in Figure 3.1. The desired syngas mixture is first prepared using a bank of calibrated rotameters, one for each gas in the mixture. The fuel mixture is split into two flows after mixing thoroughly with the desired amount of fuel passing through another rotameter (calibrated for the particular fuel composition) and the remainder flared in a diffusion flame. Finally, the required quantity of air is added, and the mixture goes to the burner. The burner is a straight cylindrical stainless steel tube with an inner diameter of 4.5 mm, the length chosen to ensure the flow is laminar and the exit velocity profile fully developed. The rotameters used for the flow rate measurements were calibrated with a bubble flow meter to ±1% accuracy, implying a maximum error of 2 % in equivalence ratio. To study the effects of preheating, the reactants are heated by electrical resistance tape wound around the burner tube. The desired reactant temperature (temporarily measured at the center of the burner exit by a type-K thermocouple, TC_1) is achieved by regulating the surface temperature of the burner with a temperature controller based on the feedback of a second thermocouple, TC_2. The mixture temperature at the exit of the burner has a nearly uniform radial profile ($\Delta T \approx 3\text{-}5$ K). The data presented here correspond to mixtures with H_2:CO volumetric ratios of 95:5, 50:50 and 33:67. Additionally for the H_2:CO =50:50 mixture, two further cases were studied: reactant preheating to ~500K and 20% dilution with CO_2.

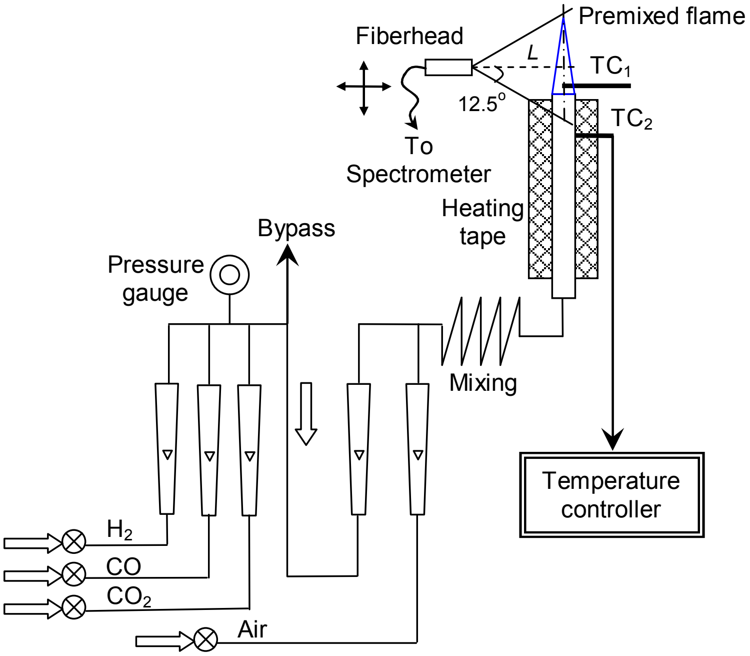

Figure 3.1. Schematic of the laminar flame experimental setup for syngas fuel mixtures.

For methane, chemiluminescence spectra were also acquired in simple laminar jet flame, as well as a swirl-stabilized combustor. The laminar burner (Figure 3.2a) is a again a straight cylindrical stainless steel tube, with the length sufficient to ensure a fully developed laminar exit velocity profile. The average velocity used was at least five times greater than the estimated laminar flame speed. A burner diameter of 25 mm was used for mixtures with equivalence ratio (Φ) less than 0.75, and 18 mm otherwise. Additionally,

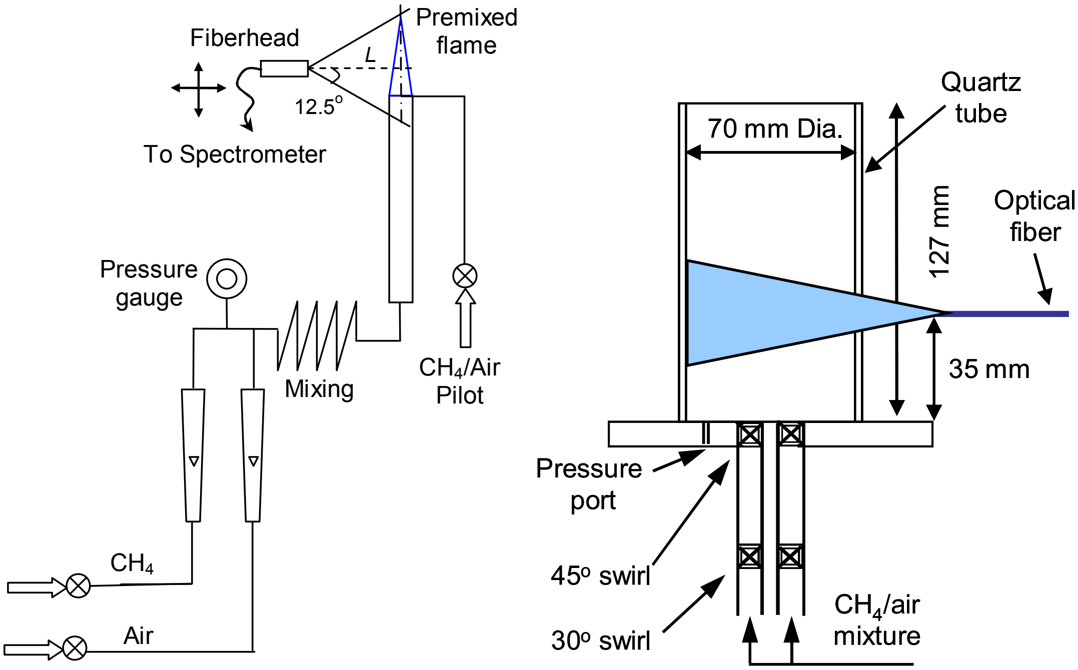

(a) (b)

Figure 3.2. Experimental schematic of a) laminar and b) swirl-stabilized methane combustors. Methane-air pilot was used to stabilize laminar flames in 25 mm OD burner.

a methane-air pilot was used to stabilize the flames for the larger burner diameter case. Calibrated rotameters monitored the methane and air flow rates with ±1% accuracy, or a ~1.5% uncertainty in equivalence ratio. The swirl combustor (shown in Figure 3.2b) was employed in an earlier chemiluminesence study [4]; it has a (theoretical) swirl number of 0.66. The combustor is a dump type configuration with the cylindrical dump plane being 70 mm in diameter and 127 mm long. The quartz walls of the test section facilitate detection of ultraviolet (UV) flame emission. The data presented here correspond to a bulk average (cold) velocity of 4-5 m/s in the test section. For similar combustors, the turbulent flame structure is usually either in the corrugated flamelet or thin reaction zone regime.

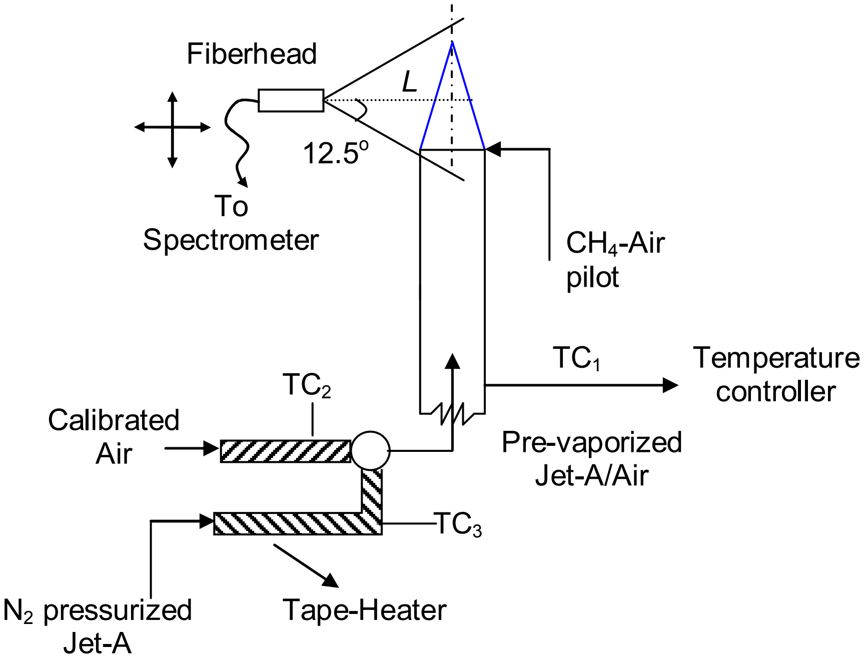

Figure 3.3. Schematic of Jet-A experimental setup (TC=thermocouple). Methane-air pilot was used to stabilize flames in the 25 mm OD burner.

Jet-A flame chemiluminescence data was acquired in an atmospheric laminar burner. Jet-A, being a liquid fuel, was first vaporized and then mixed with air to obtain a laminar, prevaporized, premixed flame. As shown in Figure 3.3, the liquid fuel, pressurized with N_2 and monitored with a calibrated rotameter, is vaporized in a straight tube maintained at a wall temperature of 573 K. Mixing occurs with air preheated to ~393 K to prevent fuel condensation. Further heating of the mixture is controlled by feedback from a thermocouple placed close to the burner exit. The heating is achieved with electrical resistance tape surrounding the burner tube, which had a diameter of 25 mm for mixtures with equivalence ratio (Φ) less than 0.7, and 10 mm otherwise. The fuel rotameter had ± 3% accuracy, resulting in a maximum error of 3.3% in equivalence ratio.

3.1.1.2 High Pressure Facility

The schematic of the high pressure experimental facility is shown in Figure 3.4a. It was previously used for laminar flame speed measurement at elevated pressure for syngas mixtures [71,72] and more details on the facility can be found in these references. The burner is a smoothly contoured nozzle with high contraction ratio, which ensures steady laminar flow even at the relatively high Reynolds number (based on the burner exit diameter *D*) characteristic of high pressure systems. The exit diameter of the burner is 6 mm, with a corresponding contraction ratio of 61. The flame is stabilized by a sintered plate-stabilized pilot around the rim of the nozzle exit.

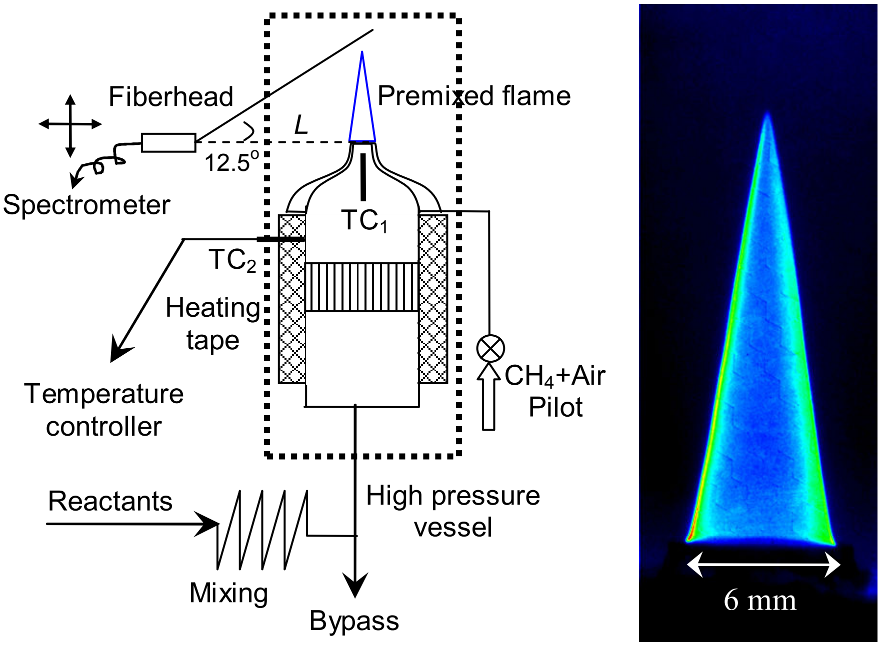

(a) (b)

Figure 3.4. (a) Schematic high pressure Bunsen flame experimental setup (TC=thermocouple). (b) Typical image of flame emission at 15 atm and 600 K preheat temperature (80:20 H_2/CO fuel mixture, 10:90 O_2:He oxidizer).

The reactant mixture, with desired composition and flow rate, is prepared in a similar fashion to the atmospheric pressure syngas facility. This mixture is sent through a plenum after mixing thoroughly, and is preheated by electrical resistance tape wrapped around the plenum. Ceramic flow straighteners in the plenum remove any unsteadiness in the incoming flow. The contoured nozzle is attached at the end of the plenum. The reactant temperature is monitored by a type-K thermocouple, TC_1 placed 2.5 cm upstream of the nozzle exit, at the center of the burner. Once the desired reactant temperature is achieved, the surface temperature of the plenum is regulated and held constant by a temperature controller based on the feedback given by a second thermocouple TC_2. The entire system is placed in a high pressure vessel with a N_2 coflow. The vessel is designed for 30 atm and has optical access suitable for chemiluminescence spectra acquisition. A sample image of the recorded flame emission at elevated pressure and temperature condition for a typical fuel mixture is shown in Figure 3.4b.

It should be noted that laminar flames for lean H_2:CO and methane mixtures at elevated pressure have a propensity to develop spontaneous wrinkles on the flame surface primarily due to hydrodynamic and thermo-diffusive instabilities. So, N_2 in the oxidizer (air) was replaced with helium (He) to suppress the formation of flame surface instabilities [73]. Addition of He improves the thermal and mass diffusivity of the reactant fuel mixture, and increases the flame thickness and Lewis number (*Le*). It has been previously noted that replacing N_2 with He does affect the flame temperature, but does not affect the fundamental chemistry [73]. An O_2/He mixture with 1:9 volumetric ratio for syngas and 1:5 volumetric ratio for methane was chosen for all the test conditions considered in this study. Experiments were performed in a syngas mixture of H_2:CO=33:67 and methane at pressures of 5 atm and 10 atm.

3.1.2 Detection System

The optical emission from both atmospheric and high pressure systems was detected with a fiber-optic based collection system coupled to an imaging spectrometer. The fiber collection array consisted of four bundles, each bundle having three 200μm fused silica fibers with a numerical aperture of 0.22. The outlet end of the fibers were located at the entrance slit of a 300 mm imaging spectrometer (Acton Spectra-Pro 300i, 300 grooves/mm grating), with a 16-bit, 1024×256 intensified CCD camera (PI-MAX, 25 mm intensifier) at the exit plane that was used to detect and record the flame emission spectrum. The grating dispersion allowed simultaneous capture of the ultraviolet and visible optical emission spectrum in the range of ~260–540 nm. The resolution of the spectrometer (with the entrance slit width set to 100 μm) was ~2 nm; this includes both dispersion and diffraction effects. This value was determined from the full-width at half-maximum intensity for diffusely scattered light from a 633 nm He-Ne laser beam. In most cases, 10 to 25 exposures were acquired at each operating condition. For most of the atmospheric pressure syngas and turbulent methane studies, the camera exposure time was 100 ms and intensifier gain was 80. However, variable exposure times (Δt_E) ranging from 150 to 2000 ms, and a gain of 200 were used to improve the signal-to-noise ratio in the high pressure experiments. These settings were also used for comparison purposes in selected sygnas atmospheric studies and in all the laminar atmospheric methane experiments. Spectra acquired without the burner operating were used to subtract the dark camera and room light background from each exposure.

Example spectra for stoichiometric syngas and rich methane flames are shown in Figure 3.5. The OH* and CH* bands, and the broadband CO_2* emission are indicated.* The OH* signal, S_{OH*}, was found by integrating the (0,0) band emission over a 10 nm bandwidth centered at the band peak (~309 nm). First however, the continuum background underneath the OH* band was estimated by fitting the region neighboring the OH* band with a cubic polynomial and subtracted from the spectra. The CH* signal, S_{CH*}, was found in a similar fashion using a 10 nm bandwidth around the 430 nm CH band. Instead of using the complete broadband CO_2* emission, a small portion at 375nm, separated from both the OH* and CH* emission, was used to represent the CO_2* signal, S_{CO_2*}. While no spectral integration was used for this signal, the spectrometer resolution results in an effective spectral integration of 375±1nm. The choice of 10 nm for integration bandwith was somewhat arbitrary, though it matches the spectral resolution of interference filters used in chemiluminescence sensing applications. Analysis of the data with 5 and 20 nm bandwidths did not change the results presented in Chapters 4 and 5 in a significant way. For example, S_{OH*} changed by a multiplicative constant that was independent of operating conditions.

---

* Two C_2* bands can also be seen for the rich methane flame; for lean methane combustion, the C_2* features are much less pronounced.

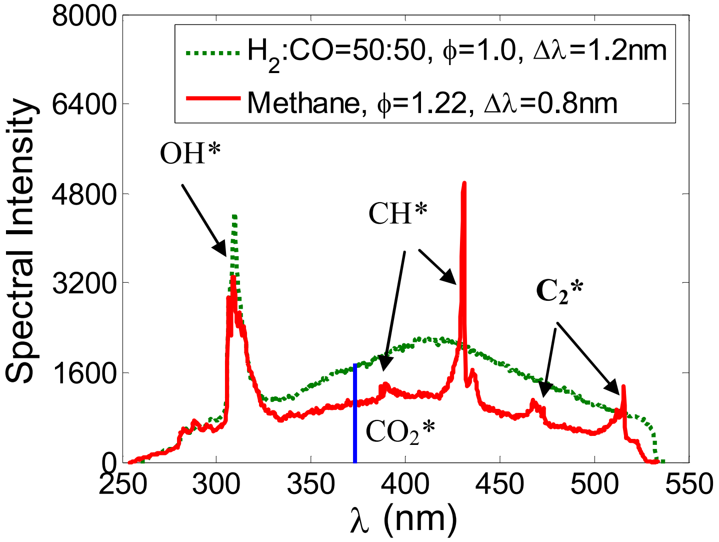

Figure 3.5. Flame spectra from methane and syngas flames: spectra shown were recorded with higher resolution than the validation data reported in this thesis.

In order to compare the absolute chemiluminescence data to the computational results, it is necessary to relate the total emission, P_c (photons s^{-1}) to the detector signal S_c (counts) for an excited-state species *c*. The detector signal S_c is given by

$$S_c = P_c \frac{\Omega}{4\pi} R_{\lambda c} \Delta t_E \cong P_c \frac{\pi D^2 / 4L^2}{4\pi} R_{\lambda c} \Delta t_E \qquad (7)$$

where Ω is the collection solid angle, $R_{\lambda c}$ (counts/photon) is the wavelength dependent responsivity of the overall detection system and Δt_E is the exposure time of the camera. The distance from the optical fibers to the emission source, *L*, determines the solid angle, which is approximately given by $\pi D^2/4L^2$, where *D* is the diameter of the fiber core.

The burners had different collection arrangements because of the inherent differences in their flow fields. In all the cases, the fiber was used to collect chemiluminescence signals without any lenses placed in front. While lenses can be used to restrict the collection volume and thus localize the measured region, this is not necessary for capturing global chemiluminescence data. For the swirl combustor used for the methane measurements, the fiber was placed at a fixed location about 95 mm away from the combustor wall and 35 mm above the base of the combustor. This allowed the fiber to collect light from most of the flame region. Due to the swirl-stabilization, the size of the flame did not change greatly with changes in fuel-air ratio. As the laminar syngas and methane flames have a conical structure, the total flame chemiluminescence was most efficiently captured by moving the fiber along a line perpendicular to the flame axis. In the high pressure set-up, the optical fiber is placed on a horizontal traverse outside the pressure vessel and is aligned such that the line of sight of the fiber passes through the center of the burner. The fiber is vertically fixed at the same level as the nozzle exit. The distance from the flame to the fiber was chosen such that the entire flame cone was within the collection solid angle of the fiber, and in most of the flames, far enough such that the chemiluminescence signal intensity approximately followed the inverse square law or in other words was proportional to the solid angle of the flame as seen by the fiber. At this distance L, all points in the flame subtend a very small angle at the fiber head and are approximately equidistant from the fiber head. This distance is obviously related to the extent of the flame and is achieved at $L \geq 10h$, where h is the flame height. In simple laminar premixed flames, the flame height is proportional to the total volumetric flow rate and it is expected that flame chemiluminescence normalized with total flow rate be a constant for a given equivalence ratio irrespective of the total flow rate. The acquired chemilumiescence data should be consistent with this observation. The above approach will help in correcting for changes in solid angle and flow rate (flame height) variations and thus help in comparing data at various conditions (including geometry). For example,

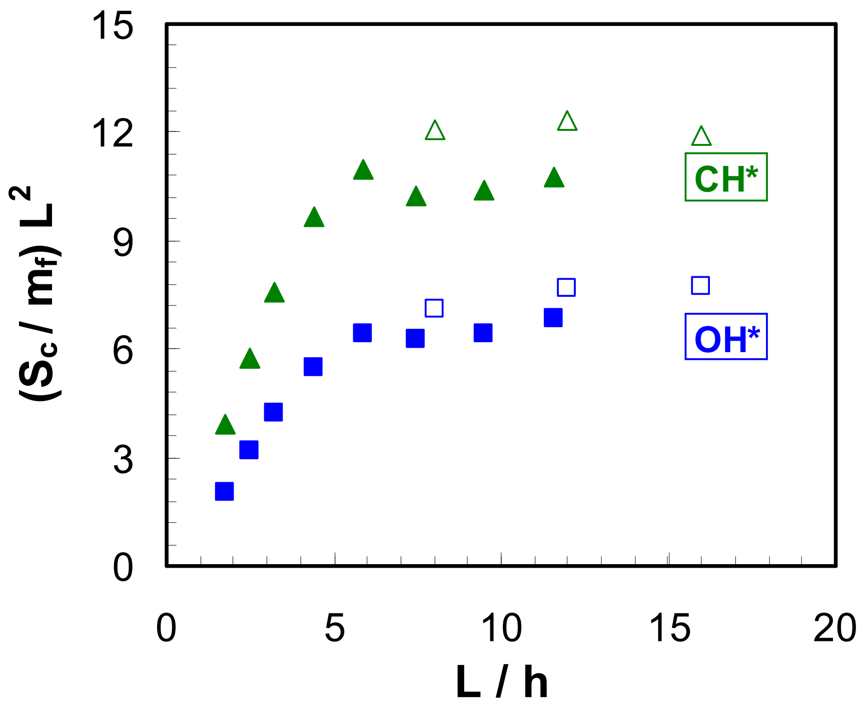

Figure 3.6. Normalized OH* and CH* chemiluminescence signal variation with the normalized distance of the fiber from the flame. Open symbols (lower flow rate), Closed symbols (higher flow rate).

in a near stoichiometric Jet-A flame with two different total flow rates, the CH* and OH* signals normalized with fuel mass flow rate (Figure 3.6) reach an almost constant value at *L~10h*. It is interesting to observe that the normalized chemiluminescence signals increase ~3 times over the range of L/h values considered. A similar trend is observed for the syngas and methane laminar flames. The results indicate that this is a robust approach that would eliminate the dependence of signals on flame height and therefore on total flowrates. However, if you are sufficiently far away from the flame, the fiber can be fixed and chemiluminescence signals can be acquired irrespective of the flame height variations. This approach was used in some of the high pressure experiments where the flame heights varied from 12-18 mm and the fiber was always horizontally positioned at a distance L = 200 mm, satisfying the condition $L \geq 10h$ for all cases. The fiber being at a fixed distance from the flame implies a constant solid angle, which eliminates the need to correct the data for variations in solid angle etc. and the data can be compared as it is. However, being very far away from the flame results in lower signal intensities which has to be compensated by acquiring data at higher intensifier gain and/or exposure settings.

3.2 Chemiluminescence Modeling

As noted previously, the goal of this work is to validate the existing chemiluminescence kinetic mechanisms for OH*, CH* and CO_2* before using the validated models to predict the dependence of chemiluminescence on important combustion flow variables. To accomplish this, the OH*, CH* and CO_2* chemiluminescence mechanisms listed in Table 2.1 and Table 2.2 (Chapter 2) were used in conjunction with standard simulations tools for simple premixed flames.

OH*, CH^* and CO_2* chemiluminescence were modeled in the syngas, methane and Jet-A flames over a range of lean to stoichiometric equivalence ratios. Detailed chemical kinetic calculations were performed for one-dimensional, adiabatic, unstrained flames with the PREMIX algorithm of the CHEMKIN 4.1 package. For adiabatic, opposed and strained flames, the OPPDIFF tool from the same software package was used. For simulating product recirculation, a reactor network, as shown in Figure 3.7, was employed that combined a chemical equilibrium solver, a non-reacting gas mixer and PREMIX. Equilibrium products at a given equivalence ratio are mixed with a known mass of fresh reactants; then laminar flame calculations (using PREMIX) are carried out with the resulting mixture.

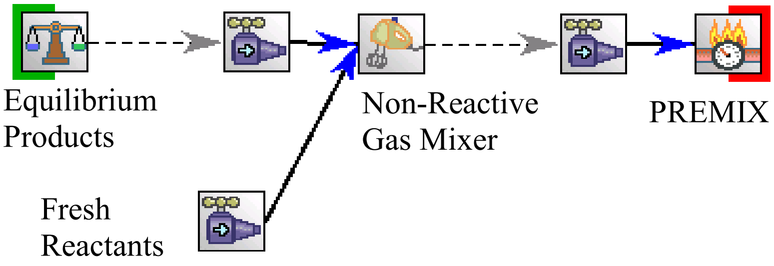

Figure 3.7. CHEMKIN block diagram for simulating EGR.

For simulating the flames, four reaction mechanisms are utilized in this study: (1) GRI Mech 3.0 [74], (2) the C_1 mechanism of Li *et al*. [75], (3) the C_1-C_3 San Diego mechanism [76] and (4) a reduced mechanism for Jet-A by Elliott *et al*. [77]. The GRI Mech 3.0 mechanism was used for methane-air and syngas-air mixtures. The GRI mechanism has been tested and validated extensively for methane and natural gas combustion over a range of pressures and temperatures. It consists of 325 elementary chemical reactions with associated rate coefficients and thermochemical properties for the 53 species involved. The C_1 mechanism is a hierarchically developed, detailed kinetic mechanism for oxy-hydrogen and C_1 species (e.g., CO, CH_2O and CH_3OH). It consists of 85 elementary reactions and 21 species with associated rate coefficients and thermochemical data. This mechanism was specifically used for validating the high pressure syngas experiments as the oxidizer included helium (He), which is not present in the GRI Mech 3.0 mechanism. For the same reason, the San Diego C_1-C_3 mechanism was preferred over the GRI Mech 3.0 mechanism for validating the high pressure methane experiments. The mechanism, relevant to flames, high-temperature ignition and detonations for various C_1-C_3 fuels, consists of 235 elementary reactions and 46 species (including helium). The fourth mechanism was developed for oxidation of kerosene type fuels using a novel genetic algorithm approach for detailed mechanism reduction and optimization. The mechanism uses a surrogate mixture of 89% n-decane and 11% toluene, to represent the Jet-A fuel chemically. The reduced mechanism comprises 167 elementary reactions and 63 species with associated rate coefficients and thermochemical data. In all the flame simulations, a converged solution was obtained by setting the grid properties such as the gradient and curvature to be 0.1, to accurately resolve the thin reaction zones in flames. Multi-component diffusion and Soret effects (thermal diffusion) are included in both PREMIX and OPPDIFF simulations, since they can be important, especially in fuels with even moderate levels of hydrogen.

There are two basic approaches that can be taken in coupling the chemiluminescence mechanisms to the standard simulation: (1) adding the chemiluminescence formation and quenching reactions into the detailed chemical mechanism before carrying out the simulation, or (2) post-processing the standard simulation results. In flames, as mentioned earlier (Chapter 2), the electronically excited species concentrations are typically quite small compared to the ground-state concentrations, and the quasi-steady state approximation can be used for the excited-state concentration to post-process the results. For example, under this assumption, the concentration of OH^* (e.g., moles/cm^3) is given by

$$[OH^*] = \frac{k_1[O][H][M] + k_2[H][OH][OH] + k_3[CH][O_2]}{\sum_j k_j[M_j] + A} \tag{8}$$

where k_1, k_2 and k_3 are the rate constants for the three suggested formation reactions (R1-R3), k_j is the quenching rate constant for OH^* by species j, $[M_j]$ is the concentration of the quencher, and A is the Einstein coefficient for spontaneous emission for the OH A→X transition. (Note: the spontaneous emission rate is typically insignificant compared to the collisional quenching). Thus the OH^* concentration can be calculated from the local concentrations of the other species and the temperature, i.e., from the results of the basic flame simulation. Results from an example calculation for a 50:50 mixture (by volume) of H_2:CO with stoichiometric air are shown in Figure 3.8. A single formation reaction reaction (R1), with the rate constant from [37], was used in this example to calculate $[OH^*]$. The peak [OH*] for this syngas fuel is at least eight orders of magnitude lower than those of the other species involved in the [OH*] reactions. Similar results can be observed at high pressure and high temperature conditions for syngas mixtures.

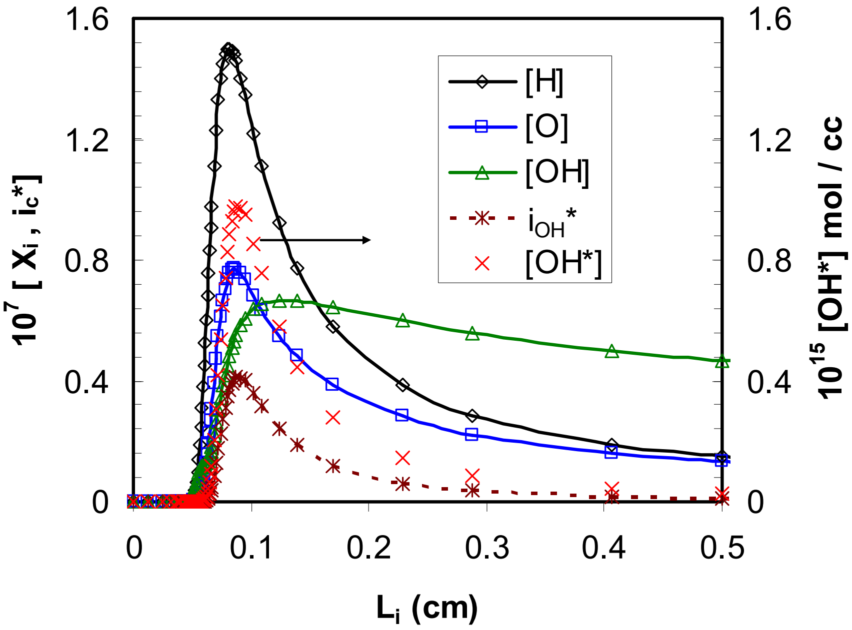

Figure 3.8. Sample CHEMKIN output for stoichiometric H_2:CO=50:50 syngas-air mixture at atmospheric (P=1atm) and non-preheated (T=298K) conditions. $[X_i]$ (mol cm^{-3}) denotes species concentrations and i_{OH}* (mol cm^{-3} s^{-1}) represents the volumetric photon emission rate for OH*.

For methane-air mixtures, however, the peak of the excited state OH* concentration is only about 5-6 orders of magnitude below most of the other species involved in its reactions (at all stoichiometries, pressure and preheat conditions considered). The only exception is [CH], with a peak value that is 2-3 orders of magnitude above [OH*]. Results from an example calculation for a stoichiometric methane-air mixture at elevated pressure and preheat temperature are shown in Figure 3.9. In this example, formation reactions R1 and R3 are used in tandem, with the rate constants from [37] and [45], used to calculate [OH*]. Using a similar analysis as above, i.e., the quasi-steady state approximation, the concentration of CH* in hydrocarbon flames can be estimated by

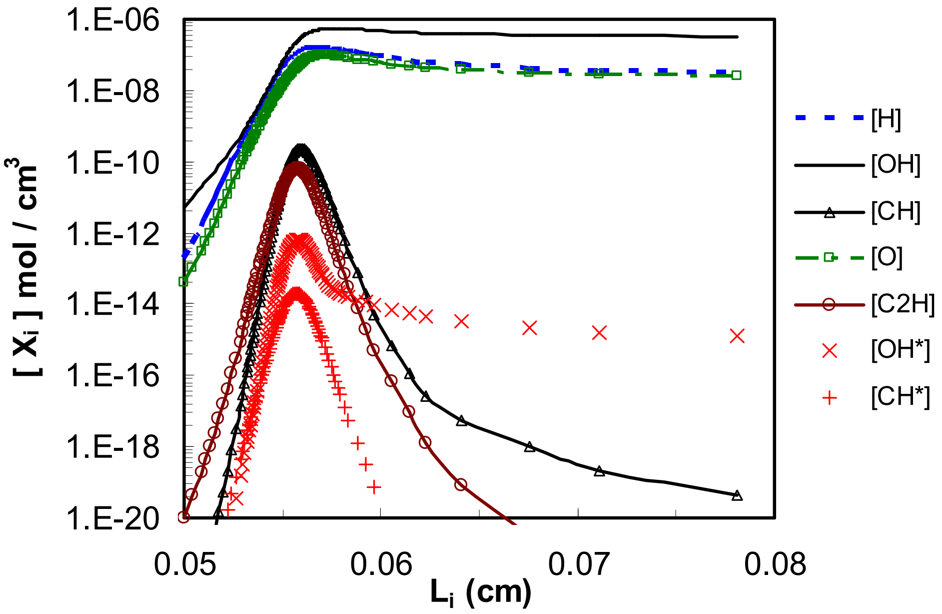

Figure 3.9. Sample CHEMKIN output for stoichiometric methane-air mixture at 15 atm and 698 K preheat condition.

$$[CH^*] = \frac{k_6[C_2H][O] + k_7[C_2H][O_2]}{\sum_j k_j[M_j] + A} \tag{9}$$

where k_6 and k_7 are the rate constants for the formation reactions (R6-R7), k_j is now the quenching rate constant for CH* by species j, and A is spontaneous emission coefficient for the CH $A^2\Delta$ - $X^2\Pi$ transition. It can be see in Figure 3.9 for a stoichiometric methane-air mixture that the excited state [CH*] is at least 3-6 orders of magnitude smaller than most of the species involved in its reaction mechanism, justifying the post processing approach for CH*. In other words, including the formation and quenching reactions for CH* in the simulation would not significantly alter the primary combustion chemistry. Therefore, OH* and CH* chemiluminescence intensities were determined by post-processing the Chemkin output with the rate parameters given in Chapter 2 (Table 2.1 and Table 2.2).

Next, the volumetric photon emission rate i_c(mole-photons cm^{-3} s^{-1}) for the chemiluminescence from species c (e.g., OH* or CH*) is given by

$$i_c = A_{kl}[C^*] \tag{10}$$

where A_{kl} is an effective band Einstein A coefficient based on the vibrational bands included in the detection bandwidth. Figure 3.8 also includes the calculation of i_{OH^*}; most of the OH* emission is seen to occur in the narrow primary reaction zone (where the peak heat release occurs), though it also extends into the product gas region.

For CO_2*, the literature does not provide individual rates for the formation, quenching and emission rates. Rather, the quasi-steady assumption was used to justify the volumetric photon emission rate given in Eq. (5). Thus for the available CO_2^* chemiluminescence model, post-processing is a necessity. However, the rate given in Eq. (5) is for the spectrally integrated emission. For combustion sensing applications, limiting the spectral detection bandwidth for the CO_2^* continuum provides several advantages. For example, detection in the near ultraviolet can be used to reduce interferences due to broadband radiation from thermal sources, e.g., combustor walls. Similarly, it is important to choose a detection wavelength that isolates the CO_2^* chemiluminescence from the other species. For these reasons, we identified 375 nm as a promising detection wavelength. A previous study reached a similar conclusion [78]. Spectral data at 375 nm for CO_2* was extracted from the spectral data provided by Slack *et al.* [55], and using similar analysis detailed in their paper, spectral photon emission rate at 375 nm was determined as given by the following expression.

$$i'_{CO_2^*} = 3.3(\pm 0.3)\times 10^3 \exp[\frac{-2300K}{T}][CO][O]\frac{mol}{cm^3 \cdot s \cdot nm} \qquad (11)$$

Since the CO_2^* spectrum is relatively flat in a region of at least ±5 nm around this wavelength [55], the photon emission rate can be approximated by $i_{CO_2^*} = i'_{CO_2^*} \times \Delta\lambda$, where $\Delta\lambda$ is the spectral integration extent of the detected emission.

In order to compare the model results (for OH^*, CH* and CO_2^*) to the global flame chemiluminescence data from the experiments, it is necessary to calculate the spatially integrated chemiluminescence. Thus the profiles through the 1-d simulated flames were integrated according to

$$I_c = \int_0^{L_i} i_c dx \qquad (12)$$

where I_c is the emission intensity for species *c*, and L_i is the integration length, which should be much greater than the flame thickness. L_i can also be chosen such that it corresponds to a combustor residence time. In such cases, the residence time is (arbitrarily) calculated with respect to the location in the flame where the heat release first reaches 1% of its peak value. The emission intensity (photons cm^{-2} s^{-1}) is related to the total chemiluminescence emission P_c (photons s^{-1}) produced by the flame through the relation,

$$P_c = I_c A_f = I_c\left(\frac{\dot{m}}{\rho_u S_L}\right) \tag{13}$$

where A_f is the flame surface area, $\dot{m}$ is the mass flow rate through the flame, ρ_u is the reactant density and S_L is the laminar flame speed. Alternatively, the chemiluminescence normalized by the fuel mass flow rate is given by

$$\frac{P_c}{\dot{m}_f} = I_c\left(\frac{1+\dot{m}_a/\dot{m}_f}{\rho_u S_L}\right) \tag{14}$$

where $\dot{m}_a$ and $\dot{m}_f$ are the air and fuel mass flow rates.

3.3 Measurement Uncertainties

In this section, the uncertainties in all the measured quantities, especially the *normalized* chemiluminescence OH*, CH* and CO_2* signals, are outlined. The main contributors to experimental uncertainties are related to flow metering and the camera detection system. The main source of systematic error comes from assuming the flame (an extended light source) is a point source.

First, the uncertainty due to flow metering is considered. Based on this uncertainty, the error in equivalence ratio can be estimated. This can also be used to estimate the uncertainty in the normalized chemiluminescence signal based on fuel mass flow rate. The flow metering system is a bank of rotameters, each for one gas, except in the case of liquid Jet-A fuel. For the gaseous systems, these rotameters are calibrated with a bubble flow meter or wet test meter to ± 1% accuracy for each gas and pressure condition, i.e., correction factors are not used either for molecular weight or density. The liquid fuel flowrate was calibrated indirectly by measuring the mass of the liquid and the volumetric flowrate was deduced based on its density to an accuracy of $\pm$ 3%. For the high pressure experiments, the reactant mixture bypass was calibrated by a Gilibrator-2 bubble flow meter, which has an error of ~ $\pm$ 7%. The combined standard uncertainty of any measured quantity is estimated by "root-sum-of-squares" (RSS) method. For example, the standard uncertainty (or standard deviation) on the equivalence ratio is estimated to be $\pm\sqrt{1^2+1^2+1^2}$ % for a two-component fuel mixture, i.e, two fuels and one oxidizer - hence, the total uncertainty is the sum of three uncertainties. In the case of the Jet-A flames, the uncertainty on the equivalence ratio is estimated to be $\pm\sqrt{3^2+1^2}$ % or ± 3.2 %. At elevated pressure, the equivalence ratio uncertainty is found to be ± 2% for syngas and $\pm\sqrt{3}$ % for methane experiments, but the total flow rate of the mixture is only known to within ± 7%.

The OH*, CH* and CO_2* chemiluminescence intensities are extracted from background subtracted flame spectra. The uncertainty in estimating the background for OH* and CH* bands (with a cubic polynomial) would lead to a maximum uncertainty of ~5% in S_{OH*} and S_{CH*}. As mentioned in an earlier section, typically 10-25 exposures or frames are recorded and the reported chemiluminescence intensities are based on the average of these images. In the atmospheric syngas systems, with low gain settings (80), the fluctuations of the OH* and CO_2* chemiluminescence signals (on a per frame basis) from the average intensity (based on all frames) were higher for very lean equivalence ratios ($\phi<0.7$) and especially for the CO_2* signal for high H_2 mixtures. Similarly in case of methane flames, higher levels of noise were observed for CH* and CO_2* chemiluminescence in lean mixtures. However, the high pressure experiments with syngas and methane were performed with higher gain (200) and camera exposure settings, and the errors were considerably lesser. Still, the uncertainties increased at very lean equivalence ratios. In Jet-A flames, the uncertainties were in general lower due to higher signals resulting from combustion of heavy hydrocarbon fuel components. The uncertainty (e_c) in the mean chemiluminescence signal intensity is calculated from

$$e_c = \left(\pm \frac{\sigma(\%)}{\sqrt{n}} * CLF \right) \tag{15}$$

where σ is the standard deviation, n is is the number of measurements, and *CLF* (confidence level factor) is assumed to be 1.96 for a 95% confidence. Table 3.1 presents the worst case uncertainties in mean OH*, CH* and CO_2* chemiluminescence signals for various fuels and operating conditions investigated in the present study. Hence, the maximum combined standard uncertainty on the chemiluminescence signals normalized with fuel mass flow rate would be $\pm\sqrt{e_c^2 + e_f^2}$, where e_c and e_f are the uncertainties in the chemiluminescence signal and fuel flow rate respectively. This results in a ± 5% uncertainty for the normalized chemiluminescence signals, for most of the operating conditions, except for very lean cases where this uncertainty could increase to as much as ± 10%. However, as can be observed in Figure 3.6, the experimental variation in the normalized chemiluminescence signal in the range of values taken by *L/h* (~8-12) can be as much as ± 15% even for near stoichiometric flames where the chemiluminescence signal intensities are high (and thus the signal-to-noise ratio is high).

Table 3.1. Worst case uncertainty in mean chemiluminescence signals and fuel mass flow rate in the experimental conditions investigated.

P(atm), T (K)	**Fuel / Oxidizer**	**CO_2* (%)**	**OH* (%)**	**CH* (%)**	**e_f (%)**
1atm, 298 K, ϕ=0.6	H_2:CO=95:5 / air	11.2	1.2		1.4
1atm, 298 K, ϕ=0.6	H_2:CO=50:50 / air	4	1.6		1.4
1atm, 298 K, ϕ=0.7	H_2:CO=33:67 / air	1.8	1.2		1.4
1atm, 498 K, ϕ=0.6	H_2:CO=50:50 / air	1.9	0.6		1.4
1atm, 298 K, ϕ=0.65	H_2:CO:CO_2=40:40:20 / air	3	2.2		1.7
5atm, 298 K, ϕ=0.7	H_2:CO=33:67 / O_2:He=1:9	2	3.5		1.4
5atm, 598 K, ϕ=0.8	H_2:CO=33:67 / O_2:He=1:9	1.4	1		1.4
1atm, 450 K, ϕ=0.73	Jet-A / air	2.7	2.7	4	3
1atm, 298 K, ϕ=0.6	Methane / air	6.5	1	15	1
10atm, 298K, ϕ=0.73	Methane / O_2:He=1:5	4.5	1.4	7	1
5atm, 598K, ϕ=0.64	Methane / O_2:He=1:5	3.3	1	2.9	1

CHAPTER 4

SYNGAS MODELING VALIDATION

As detailed in Chapter 2 (Table 2.1), two of the OH* formation reactions (R1 and R2) involve hydrogen chemistry, while the third (R3) arises only in hydrocarbon systems. So experiments were carried out first for H_2:CO (syngas) fuel mixtures to test the chemiluminescence mechanisms and rates of formation reactions R1 and R2. In addition to OH*, CO_2* is the other prominent emitter in the ultraviolet and visible region of the electromagnetic spectrum in simple syngas fuel mixtures. Thus this chapter presents a research effort with an aim of identifying the important chemiluminescence formation reactions and their kinetic parameters, for the excited species OH* and CO_2* in typical syngas flames. The validation experiments were carried out in laminar flames, and the robustness of the chemiluminescence mechanisms were tested by examining various operating conditions such as equivalence ratio, reactant preheat, pressure and fuel composition.

Experimental chemiluminescence signals are compared to the numerical simulation results for validation. The photochemistry for OH* and CO_2* chemiluminescence is first validated in flames with various mixtures of H_2-CO-CO_2 (syngas) fuels and air at atmospheric pressure (Section 4.1). Then results are presented for elevated pressures (Section 4.1), performed for a more limited set of syngas fuel compositions with an oxidizer composed of a 1:9 mixture of oxygen and helium instead of air. As potential sources of uncertainty in the validations, estimates of the contribution of thermally excited OH* (Section 4.3) and OH* self-absorption (Section 4.4).are also presented.

4.1 Atmospheric Pressure Validation

Chemiluminescence data was acquired in three syngas fuel mixtures: H_2:CO volumetric ratios of 95:5, 50:50 and 33:67 premixed with air and exiting a straight tube burner. For the 50:50 mixture, reactant preheating to ~500K and 20% dilution of the fuel with CO_2 was used to further test the mechanisms. Additionally for better comparison to the high pressure results, data at atmospheric conditions was acquired in the contoured laminar burner with high intensifier gain (200) for the 95:5 and 50:50 syngas mixtures, and with the collection fiber placed such that L/h~10.

As noted in Chapter 3, the measured and simulated chemiluminescence signals are compared after being spatially integrated over the flame. Thus it is important to determine the proper integration length (L_i) for the simulations (see Eq. 12). For the syngas flames, the size of the region captured by the optical fiber is ~20-50 mm, depending on the distance from the fiber to the flame. However, the part of the optical collection region that includes the reaction zone and hot flame gases (locations where chemiluminescence might be expected to be produced) ranges from ~6-12 mm downstream of the flame. Since the "experimental" integration length varies from flame to flame (and within a single flame), the question arises, what is the sensitivity of the simulated chemiluminescence signal to the integration length.

Example simulation results for an atmospheric H_2:CO=95:5 mixture at $\phi = 0.8$ are shown in Figure 4.1. The simulation uses the R1 formation reaction with the rate constant from [37]. The figure shows spatially integrated heat release rate (Q), and I_{OH^*} and $I_{CO_2^*}$

signals as a function of the integration distance through the 1-d flame. The origin for the integration was chosen to be the start of the primary reaction zone, defined to be the point where the heat release rises to 1% of its peak value. The profiles are normalized by the integrated value achieved at 30 mm. Most of the OH* signal occurs coincident with the heat release. While the heat release rises first, the integrated OH* chemiluminescence approaches a plateau value slightly earlier, within a few millimeters after the start of the reaction zone. On a relative basis, the CO_2* chemiluminescence extends farther into the post-flame burnout zone (the extended region of low heat release).

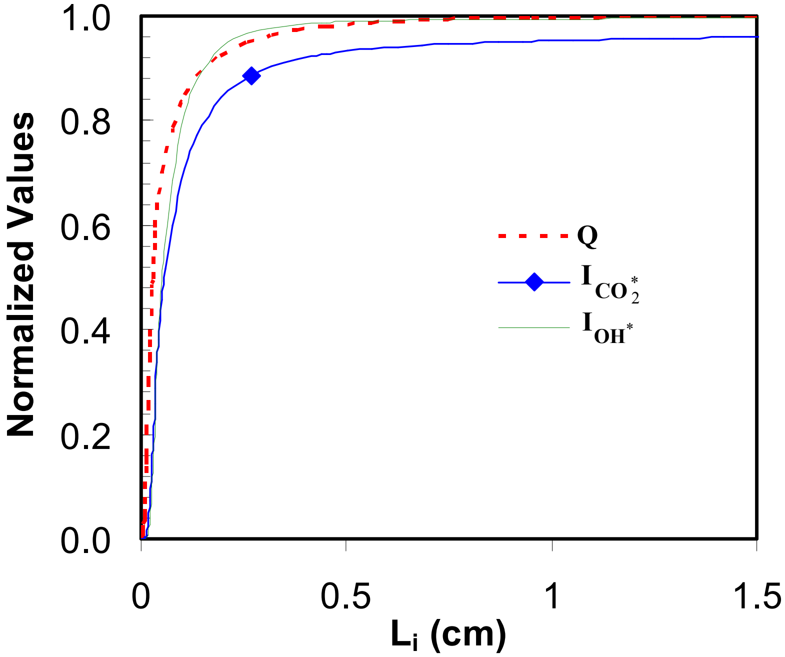

Figure 4.1. Simulation results of normalized integrated heat release rate, normalized OH* and normalized CO_2* chemiluminescence signal profiles.

Still, there is little change in the integrated chemiluminescence signals for L_i=6-12 mm. For I_{OH^*}, the change is less than 1%, while for $I_{CO_2^*}$ the variation is closer to 2%. Thus, the simulation results will only be weakly dependent on the choice of an integration distance between 6 and 12 mm for this type of flame, i.e., where most of the chemiluminescence occurs in the primary reaction zone. Similar results were obtained for other lean mixtures. For a given fuel composition, the trend seen is that moving to a leaner mixture causes the plateau in the integrated chemiluminescence to become more coincident with the primary reaction zone. For an increasing fraction of CO in the fuel, the OH* and CO_2* chemiluminescence signals extend farther from the primary heat release zone, with the CO_2* signal effected more. For mixtures very close to stoichiometric, a more significant sensitivity to the integration length was observed, because a greater fraction of the chemiluminescence is produced in the *high temperature* product gases. For the same H_2:CO=95:5 mixture at $\phi = 1$, I_{OH*} changes by 3% for L_i ranging from 6-12mm, while for I_{CO2*} the variation is nearly 9%. Since the lean cases showed little sensitivity to the choice of integration length, an L_i=10 mm was chosen for the comparisons as it best matches the actual region imaged in the stoichiometric cases.

We begin by considering the ratio of chemiluminescence intensities from CO_2^* and OH^*. From Eqs. (1) and (7), the measured chemiluminescence signal ratio is related to the simulated ratio through the expression

$$\frac{S_{CO^*_2}}{S_{OH^*}} = \frac{R_{\lambda,CO_2^*}}{R_{\lambda,OH^*}} \frac{I_{CO_2^*}}{I_{OH^*}} = C_{\det} \frac{I_{CO_2^*}}{I_{OH^*}} \qquad (16)$$

Thus, the measured ratios are seen to be independent of many of the optical parameters of the experimental setup, such as the detector/spectrometer settings and collection solid angle, as well as the total flame size (or flame area or mass flow rate). In the ideal case, the measured ratio should only differ from the computed emission intensity ratio ($I_{CO_2^*}/I_{OH*}$) due to the change in the detection system responsivity with wavelength. Thus if the chemiluminescence simulation predictions are accurate, the results should differ from the experimental data only by a single multiplicative constant (C_{det}) that is independent of experimental conditions, including H_2:CO mixture ratio, equivalence ratio and addition of diluents. Therefore, experimental and predicted chemiluminescence ratios are compared first.

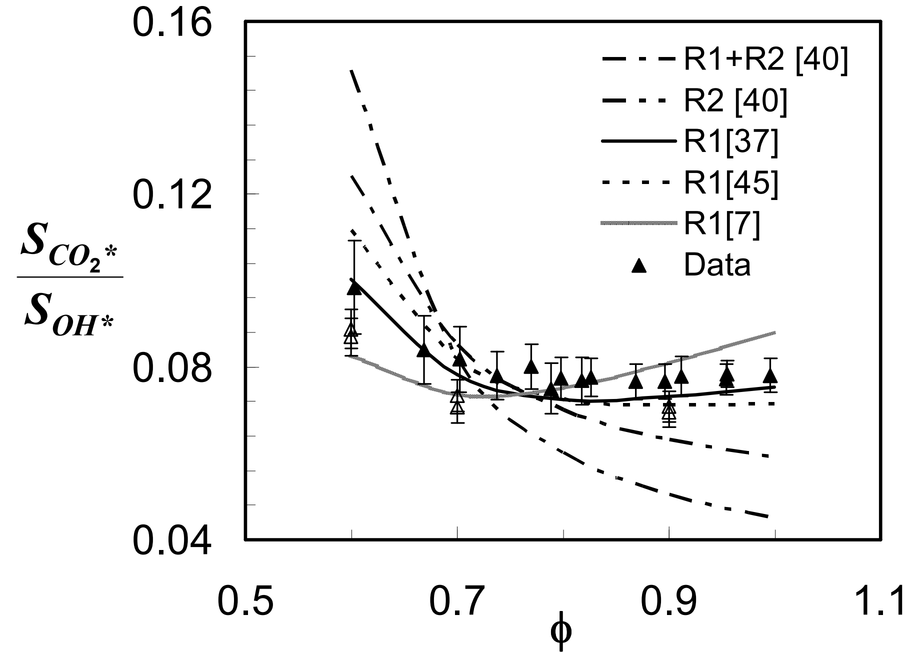

Figure 4.2. OH* mechanism validation: chemiluminescence intensity ratio predictions and experimental data in H_2:CO=50:50 syngas mixture. Simple tube burner (closed symbols); contour burner (open symbols).

Figure 4.2 shows a comparison of experimental and simulation results for the five different OH* chemiluminescence mechanisms and the one CO_2* global mechanism. The first mechanism uses both reactions R1 and R2, while the second uses only R2. Both use the rate constants proposed by Smith *et al.* [40] from low-pressure flame studies. The third, fourth and fifth mechanisms include only R1. The third uses the rate constant originally proposed by Petersen [37] from shock tube results, while the fourth uses a “reoptimized” higher activation energy (E_a) rate constant from a later study by the same group [45]. The fifth mechanism uses a temperature independent rate constant proposed by Smith [7]. The figure presents results for a 50:50 H_2:CO fuel without CO_2 dilution and with room temperature reactants. In this comparison, C_{det} for each mechanism was chosen to match the experimental ratio by minimizing the global least square difference between the simulation and experimental results.

The variation of chemiluminescence ratio with equivalence ratio is poorly predicted by the first mechanism based on the two formation steps with no temperature dependence in the rate constants. The second mechanism with only R2 provides even worse results. The simulation results with these OH* mechanisms increase too rapidly as the mixture is made leaner. The third, fourth and the fifth mechanisms, employing only reaction R1 provide greatly improved results. The sole differentiator is the activation energy E_a: zero (fifth mechanism), 6940 cal (third mechanism) and 10,000 cal (fourth mechanism). Furthermore, it can be seen in Figure 4.2 that the simulations with the highest E_a [45] tend to over predict the ratio at the leanest conditions, while the mechanism with E_a=0 [7] under predicts the ratio. Overall, the mechanism with intermediate E_a [37] provides the best results. For example at ϕ=0.6, the high E_a simulations *over* predict the experimental data by 27%; the mechanism with no temperature dependence *under* predicts by as much as 25%; the intermediate E_a simulations are within 8% of the experimental ratio.

The other fuel mixtures and conditions tested lead to similar conclusions. First, mechanisms without the R2 formation reaction, but with a temperature dependent rate constant for R1 provide reasonable matches to the experiments.[*] It is highly unlikely that R2 becomes significant at other important conditions. For example, the contribution from R1 should become even more dominant at higher pressures since the concentration of the third-body, [*M*], are likely to increase faster than the radical concentrations. Thus we restrict our attention to R1 mechanisms in the remaining portion of this study.[†] Second, a higher activation energy for R1 decreases the OH* signal in the leaner equivalence ratios owing to lower temperatures in this range. In other words, a temperature independent rate constant would predict more OH* at leaner equivalence ratios than the rate constant with a higher (positive) activation energy. Third, the intermediate E_a value given in [37] provides the best overall match to the chemiluminescence ratios for lean mixtures. The one exception to this is the high H_2 fuel composition (95:5), where the higher activation energy [45] provides a slightly better match over most of the equivalence ratio range.

The predictive capability of the chosen OH* and CO_2* mechanisms is further evidenced in Figure 4.3, where the comparison of the simulations and experiments is shown for all the syngas flames. The top portion of the figure compares the absolute values of the ratios, while the lower portion displays the relative deviation between the simulations and experiments, defined as

$$\text{Relative Deviation} = \frac{C_{\text{det}}\left(I_{CO_2^*}/I_{OH^*}\right) - S_{CO_2^*}/S_{OH^*}}{S_{CO_2^*}/S_{OH^*}} \; . \qquad (17)$$

---

[*] Adding a temperature dependent rate constant for R2 does not produce agreement with the data.

[†] This is the reason for choosing R1 for the results presented in Figure 4.1.

In the results shown in Figure 4.3, a single value of C_{det} (=20) was used for all the cases. The simulations are able to accurately predict the experimental results, with deviations of less than ±10% for most of the cases, despite the large change in the ratio between cases. The exception is the near-stoichiometric results for the high H_2 case (95:5), where the predictions systematically fall below the experimental results by slightly more (~15-20%).

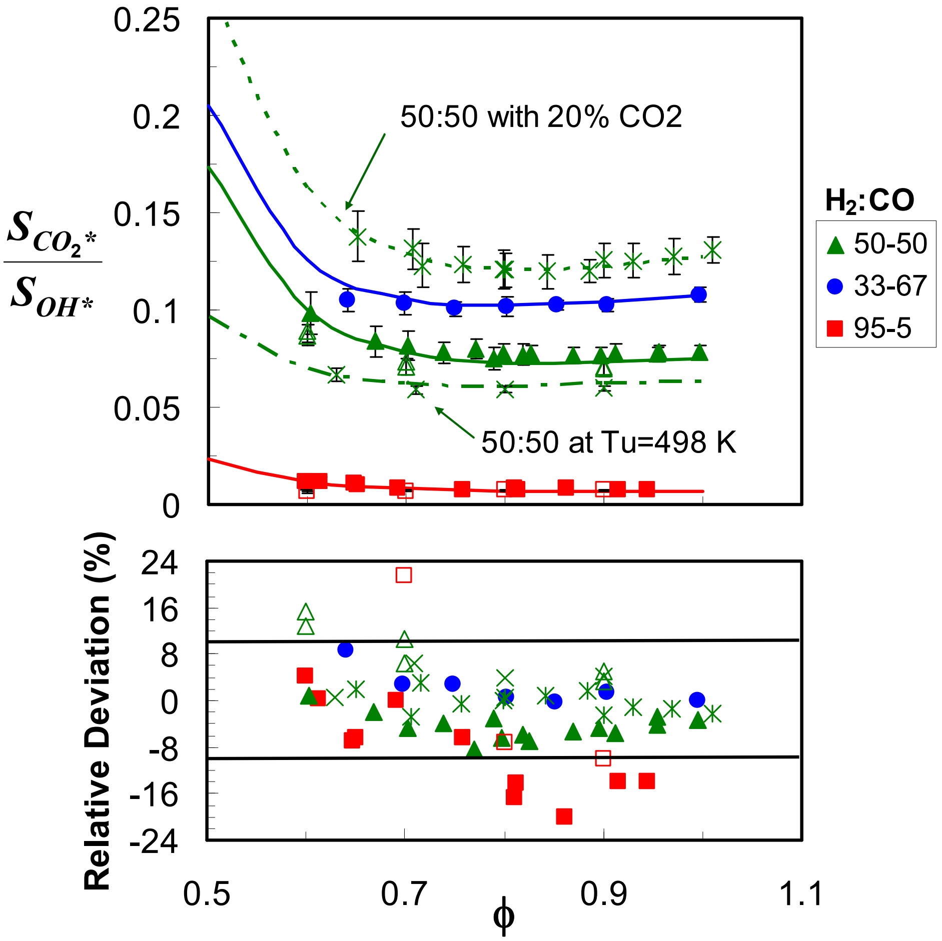

Figure 4.3. Chemiluminescence ratios in syngas flames (above). Relative deviation between experimental data and simulated ratios, ±10% error levels are indicated by the horizontal lines (below). Simple tube burner (closed symbols); contoured burner (open symbols).

As noted above, data were acquired in a different (contoured) laminar burner (and at high intensifier gain) for two mixtures (open symbols in Figure 4.3). Other than a single data point for the 95:5 mixture at ϕ=0.6, where the simulation deviates from the experimental data by as much as ~85%, the overall agreement between the simulation results and the experimental data is again quite good.

While the chemiluminescence ratios provide some measure of validation for the OH* and CO_2* simulations, it is possible that an error common to both cancels out, producing the good agreement with the experiments. Therefore, the individual OH* and CO_2* chemiluminescence signals are also examined. The 1-d flame simulations used here, however, can not provide absolute emission intensity given that they contain no information on flame area. From Eq (16), it is clear that one can compare the experiments and simulations by normalizing the signals with the fuel mass flow rates. Since the syngas mixtures actually contain two fuels, and because the CO_2* originates from the carbon monoxide fuel while the OH* is formed indirectly from the hydrogen, we choose to normalize the two chemiluminescence signals with their respective fuels (OH* with $\dot{m}_{H_2}$ and CO_2* with $\dot{m}_{CO}$). In this context, the absolute chemiluminescence signal rate ($\dot{S}_c$) for a given chemiluminescence species c is related to the 1-d simulation results, according to Eqs. (7) and (14), as follows.

$$\frac{S_c/\Delta t_E}{\dot{m}_c} = \frac{\dot{S}_c}{\dot{m}_c} \approx \frac{C_c}{L^2} \left\{ \frac{1+{}^{\dot{m}_a}\!/\!_{\dot{m}_f}}{\chi_c \rho_u S_L} \right\} I_c \tag{18}$$

Here $\dot{m}_c$ and χ_c are the mass flow rate of fuel and the mole fraction of either H_2 or CO in the fuel corresponding to species c, the change in solid angle Ω as the fiber was moved is modeled as a simple $1/L^2$ variation, and all the constants (or variables held constant) are combined into the value C_c. With Eq. 18, the simulation results can now be compared to the experimental results for total chemiluminescence signals.

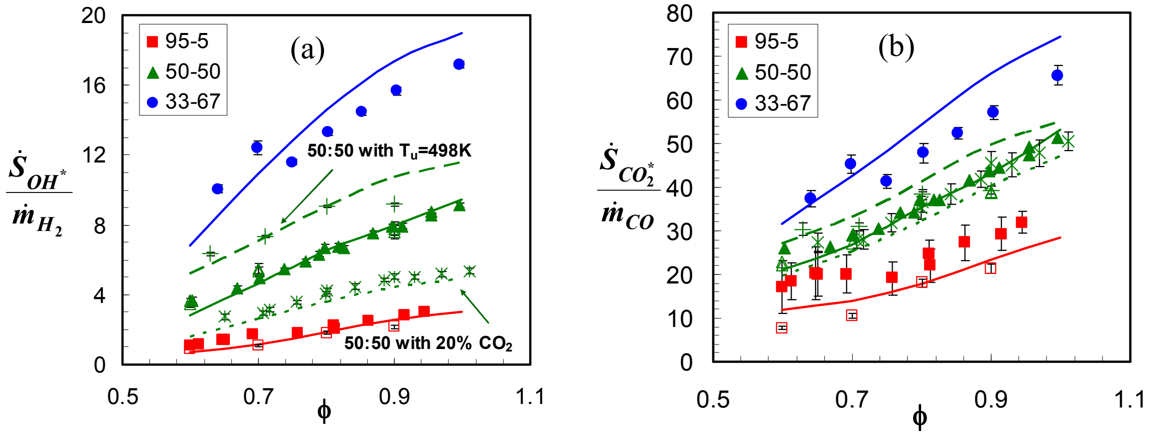

Figure 4.4. Comparison between measured and simulated normalized chemiluminescence for a) OH* emission and b) CO_2* emission for syngas flames. Simple tube burner (closed symbols); contoured burner (open symbols).

Results are shown in Figure 4.4a for the normalized OH* signals for the various syngas fuel compositions. Note that the normalized signal varies by a factor of 20 across the range of equivalence ratios and fuel compositions investigated. The OH* chemiluminescence mechanism accurately simulates the measured OH* emission signals for the different H_2:CO compositions (within 10-15%), except for the very lean regime of the flames with very high H_2 content, where the simulatation under predicts some of the data by almost 50% at Φ=0.6. The agreement is similarly quite good for the preheated and CO_2 diluted cases.

The CO_2* results are shown in Figure 4.4b. The CO_2* mechanism predicts the baseline H_2:CO=50:50 case and its dilution and preheat variants reasonably well. It is interesting to note that while the addition of CO_2 as a diluent lowers the OH* chemiluminescence noticeably, the simulatation correctly predicts the minor change seen in the CO_2^* signal. Similarly, preheating the reactants has less effect on chemiluminescence from CO_2^* than from OH*. This is expected, given the smaller activation energy in the CO_2^* mechanism. As with the OH* mechanism, the CO_2^* simulations for the high H_2 case produce deviations reaching nearly 50% for $\phi<0.7$.

If only the experimental data with from the straight tube burner with lower intensifier gain is considered, both mechanisms under predict the high H_2 case by similar levels; thus the ratio remains approximately correct (as was seen in Figure 4.3). The CO_2^* mechanism, however, shows larger discrepancies than the OH* mechanism closer to stoichiometric conditions. This explains the larger relative deviations seen in the chemiluminescence ratios for the high H_2 case above $\phi>0.8$. The fact that both mechanisms systematically deviate considerably from the experiments at lean conditions for high H_2 fuels suggests a single source of error. This could be partly due to the inconsistencies in choosing the distances between the fiber and the flame for the straight tube syngas experiments.[*] Another possibility is the accuracy of the basic simulation approach, i.e., using a 1-d simulatation and GRI Mech 3.0 to simulate the laminar Bunsen flame speed and concentration profiles for a high H_2 fuel where the high diffusivity of H_2 can be important. In fact in a previous study, it was found that the experimentally measured flame speed for the H_2:CO=95:5 case was under predicted by the same mechanism by as much as 40% at $\phi = 0.6$ [71]. Thus based on the overall results, it can be concluded that the mechanisms for chemiluminescence from CO_2^* (Eq. 11) and OH^*

---

[*] In this experimental approach, the chemiluminescence signal intensities depend on the distance between the fiber and the flame as shown in Figure 3.6.

(employing only R1 with E_a=6940 cal/mol) in atmospheric flames of H_2/CO mixtures are validated, at least for the range of conditions examined here.

4.2 Elevated Pressure Validation

Experiments were performed at 5 and 10 atm with laminar syngas flames in the high pressure experimental facility. Flame chemiluminescence was acquired from a H_2:CO=50:50 mixture at 10 atm with 598 K reactant preheat conditions in the lean equivalence ratio range. At the same pressure and temperature, four syngas mixtures viz H_2:CO volumetric ratios of 40:60, 50:50, 60:40 and 80:20 were studied at a fixed equivalence ratio of 0.6 to investigate the variation of flame chemiluminescence with hydrogen content of the syngas mixture. A H_2:CO=33:67 mixture was studied at 5 atm for effects of preheat on flame chemiluminescence. The experiments were performed with a O_2:He=1:9 mixture as oxidizer. For these cases, the simulations employed the C1 mechanism [75] as GRI Mech 3.0 does not include helium.

The syngas flames were 2-4 exit diameters (or 12-24 mm) tall. The size of the circular region captured by the optical fiber at the burner plane is approximately two times the height of the flame. Because the data cover a significant variation in size, it is again important to consider the sensitivity of the simulations to the integration length before comparing their results to the experimental data. Example simulation results for a 10 atm, 598 K preheated H_2:CO=50:50 mixture at ϕ = 0.8 are shown in Figure 4.5. The simulatation uses the R1 formation reaction with the rate constant from [37]. The figure shows spatially integrated heat release rate, and I_{OH^*} and $I_{CO_2^*}$ signals as a function of the integration distance through the 1-d flame. The profiles are normalized by the integrated value achieved at L_i ~5 cm. The high pressure flame is significantly thinner compared to

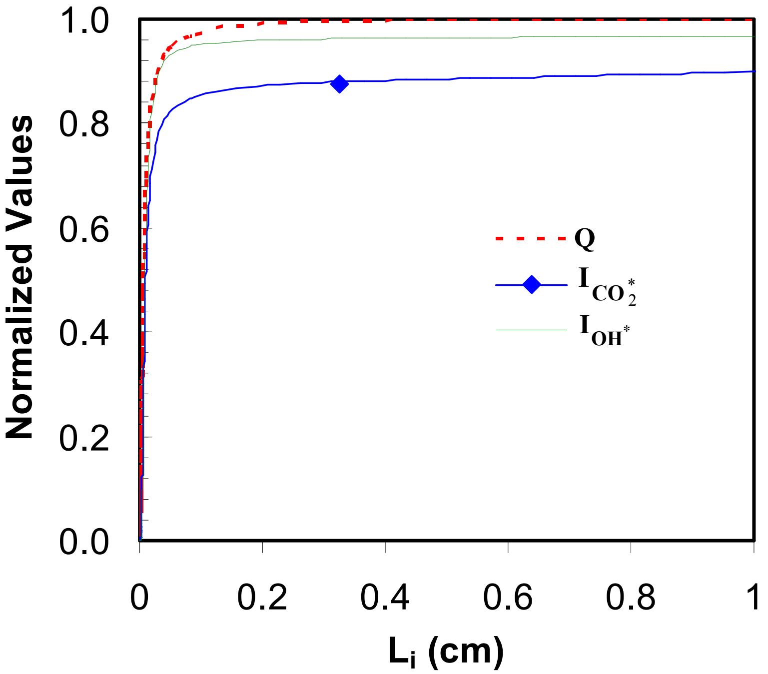

Figure 4.5. Simulation results of normalized integrated heat release rate, normalized OH* and CO_2* chemiluminescence signal profiles at 10atm and 598K conditions.

its atmospheric counterpart (Figure 4.1). Although the three profiles rise almost simultaneously, the heat release plateaus first, within a few millimeters after the start of the reaction zone, and 99% of heat release is completed within 1 mm. On a relative basis, the CO_2* chemiluminescence extends farther into the post-flame burnout zone (the extended region of low heat release).

This extended signal region can be seen in chemiluminescence images acquired with a UV-sensitive ICCD camera, which thus produces images of combined OH* and CO_2* chemiluminescence. One such image for a 10 atm, 598 K preheated H_2:CO=50:50 mixture at $\phi = 0.9$ is shown in Figure 4.6a. Most of the OH* and CO_2* chemiluminescence signal comes from the reaction zone (white region). Radial profiles of the signal intensity are shown in Figure 4.6b. Horizontal cuts at two locations along the flame height from the base of the burner, one at 20% and the other at 80% of the

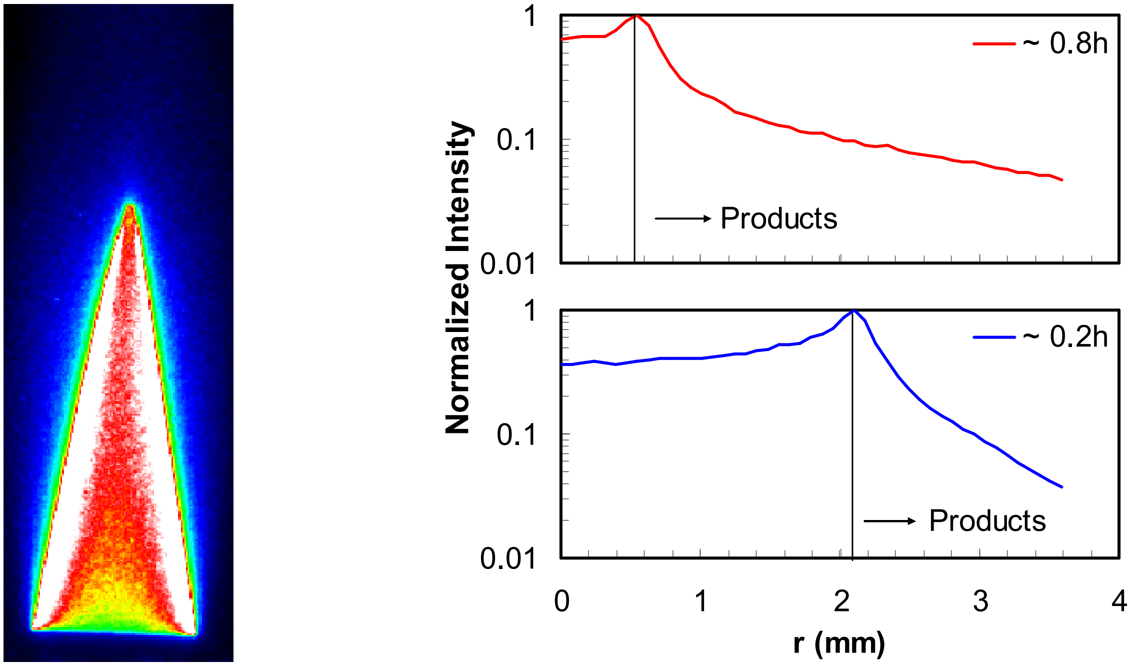

(a) (b)

Figure 4.6. Chemiluminescence image analysis for a H_2:CO=50:50 flame at 10 atm, 598 K and ϕ=0.9. (a) Raw image (burner diameter is 6 mm) and b) radial (line-of-sight integrated) intensity profiles at 20% and 80% of the flame height.

flame height are shown. The burner radius is 3 mm. In each of the plots in Figure 4.6b, the peaks corresponds roughly with the flame location, and the product gases exist primarily to the right of this peak. From the results corresponding to 20% of the flame height, it can be seen that the signal intensity drops to ~3.5% of the peak 1.4 mm from the flame, probably due to mixing with the colder nitrogen coflow. Similarly for the 80% height, the intensity drops to ~4.5% of the peak signal 3 mm from the flame. The decrease of signal at this location is less steep due to the signal contributions from the exhaust gases that emanate from the lower regions of the flame. It should be noted that most of the spatially integrated chemiluminescence is contributed by the lower portion of the flame, owing to its conical shape. Hence, from experiments, it can be concluded that an integration distance of ~5 mm should be sufficient to capture most of the product zone emission.

Revisiting Figure 4.5, it can be seen that there is not much change in the integrated chemiluminescence signals for L_i=5-10 mm. I_{OH*} remains practically constant while I_{CO_2*} changes by less than 1%. Thus, the simulatation results will only be weakly dependent on the choice of an integration distance between 5 and 10 mm for this case, where most of the signal comes from the reaction zone. The situation is similar for the other lean H_2:CO=50:50 mixtures and for the H_2:CO=33:67 flames at 5 atm. For near stoichiometric mixtures, a greater fraction of the chemiluminescence is produced in the high temperature product gases, similar to the results observed for atmospheric pressure. For the same H_2:CO=50:50 mixture at ϕ=1, I_{OH*} changes by 3% for L_i ranging from 5-10 mm, while the I_{CO_2*} variation is closer to 6%. Since the lean cases showed little sensitivity to the choice of integration length, an L_i=10 mm was chosen since it more closely matches the stoichiometric cases.

The CO_2*/OH* chemiluminescence intensity ratio is considered first, for the reasons cited earlier. OH* chemiluminescence was simulated with two different models for the R1 rate constant; one is a temperature independent rate constant [7], while the other employs the activation energy from [37]. Results for a H_2:CO=50:50 mixture at 10 atm and reactant preheat of 598 K are shown in Figure 4.7. The C_{det} for each mechanism was chosen by minimizing the global least square difference between the experimental and simulation results[*] As in the low pressure case, the mechanism with the temperature dependent constant does an excellent job of matching the data, while the temperature independent mechanism produces a slight disagreement at the very lean and the near stoichiometric equivalence ratios. The remaining comparisons therefore consider only the temperature dependent rate constant.

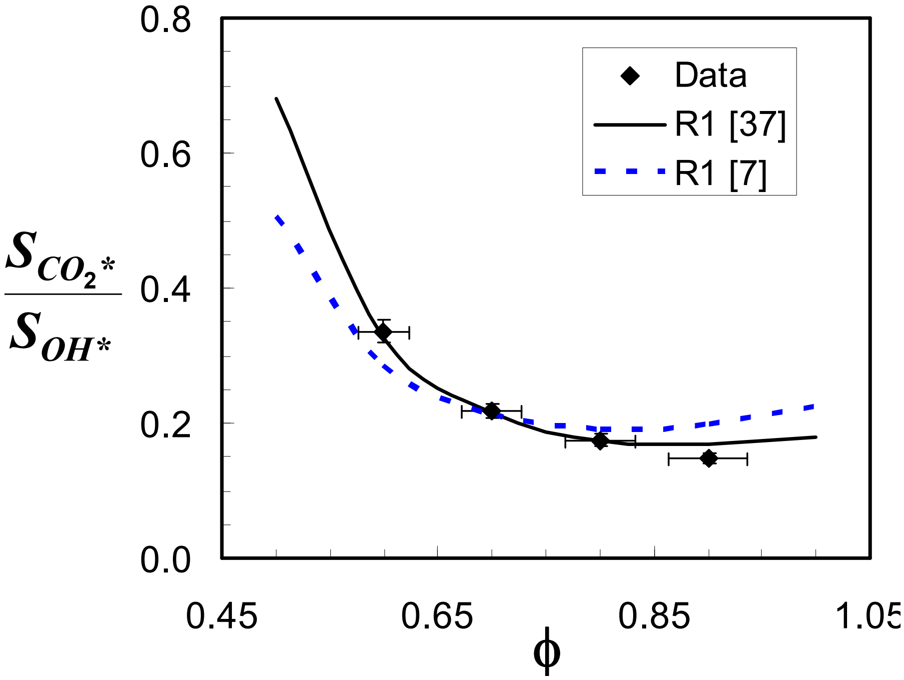

Figure 4.7. OH* mechanism validation in syngas flames at elevated pressure. Chemiluminescence intensity ratio predictions and experimental data for H_2:CO=50:50 mixture at 10 atm and 598 K reactant preheat.

The predictive capability of the chosen OH* and CO_2* mechanism is further evidenced in Figure 4.8, where the comparison of the simulations and experiments is shown for all the high pressure conditions. It can be seen that the simulations are able to accurately predict the experimental results, with deviations of less than ± 10% for most of

---

[*] As described in the previous section, the simulation results should differ from the experimental data by a single multiplicative constant due to the unknown responsivity of the detection system.

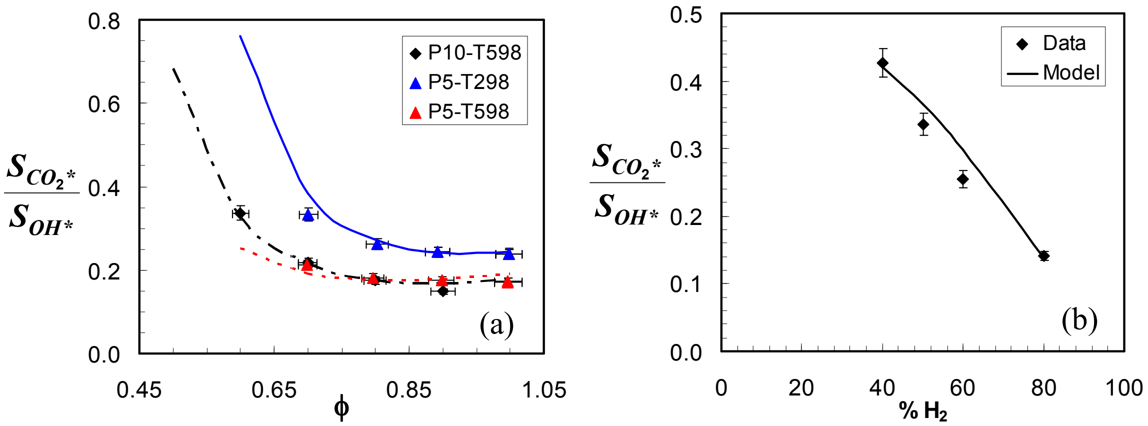

Figure 4.8. CO_2*/OH* chemiluminescence intensity ratios (a) in H_2:CO=50:50 (10 atm) and H_2:CO=33:67 (5 atm) mixtures, (b) at ϕ=0.6 for 10 atm and 598 K preheat .

most of the cases. It should be noted however, that C_{det}=32 was used for the 10 atm case, while an ~18% higher value (C_{det}=38) was used for the 5 atm results. Other than this anomaly, the overall agreement between the simulatation results and experiments is excellent. Another observation is that C_{det} was almost 60% higher than the value obtained at atmospheric conditions. This either implies that C_{det} is a function of pressure or that there may be a systematic error in the basic chemical mechanisms used to predict the chemiluminescence precursors, especially in the helium mixtures employed for the high pressure conditions. The focus on helium is because both the GRI Mech 3.0 and C1 mechanisms produce OH* and CO_2* chemiluminescence predictions that are quite similar at various pressure and preheat conditions for syngas-air flames. It is also possible that there was a systematic change in the detection system that resulted in the apparent discrepancy of ~18% in the value of C_{det}, though this is considered less likely.

Normalized OH* and CO_2* chemiluminescence signals are again considered to further investigate the accuracy of the OH* and CO_2* mechanisms. For reasons cited earlier, OH* and CO_2* chemiluminescence signals are normalized with the reactant mass flow rates of H_2 and CO respectively. The simulation results and the experiments are compared through the expression in Eq. 18. Results for normalized OH* and CO_2* chemiluminescence as a function of equivalence ratio are shown in Figure 4.9 for a H_2:CO=50:50 syngas mixture at 10 atm and 598 K reactant preheat. The normalized experimental OH* and CO_2* chemiluminescence signals are predicted to within 5% (except for the richest OH* data point, which is within 8%); this can be characterized as excellent agreement.

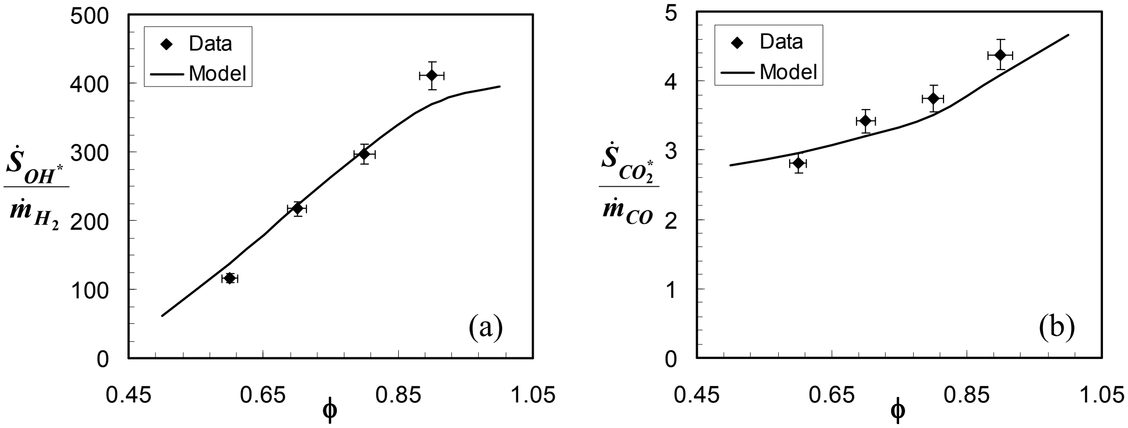

Figure 4.9. Measured and simulatated normalized chemiluminescence for (a) OH* and (b) CO_2* for a H_2:CO=50:50 syngas mixture at 10 atm and 598 K reactant preheat.

Returning to the issue of the change in the scaling constant, C_{det}, for the chemiluminescence intensity ratios at high pressure compared to atmospheric conditions, we can investigate it further by examining the normalized signals for OH* and CO_2*. As the high pressure experiments are conducted in the contoured burner with intensifier gain of 200, we consider only results from the atmospheric experiments with the same burner and gain setting, i.e., the H_2:CO=50:50 mixture. C_{OH*}, (the scaling constant required to match the normalized experimental OH* signal to the simulation) decreased 9 times from the 1 atm (air) to high pressure (He) case, while the scaling constant for CO_2* decreased by 5.5 times. Some of the possible explanations are: 1) the simulations with He are overpredicting I_{OH^*} and $I_{CO_2^*}$; 2) the overprediction is due problems with the basic chemical mechanism at high pressure; 3) the experimental signals are attenuated due to absorption in the flame gases at high pressure; and 4) there is a systematic change in the detection system responsivity between the low and high pressure cases. The last option is not likely, as the detection system, flame sizes, and collection solid angles were nearly the same in both cases. The third option, absorption is addressed in a following section. The second and first explanations are possible, but would require the simulations to correctly model the equivalence ratio dependence at both low and high pressure.

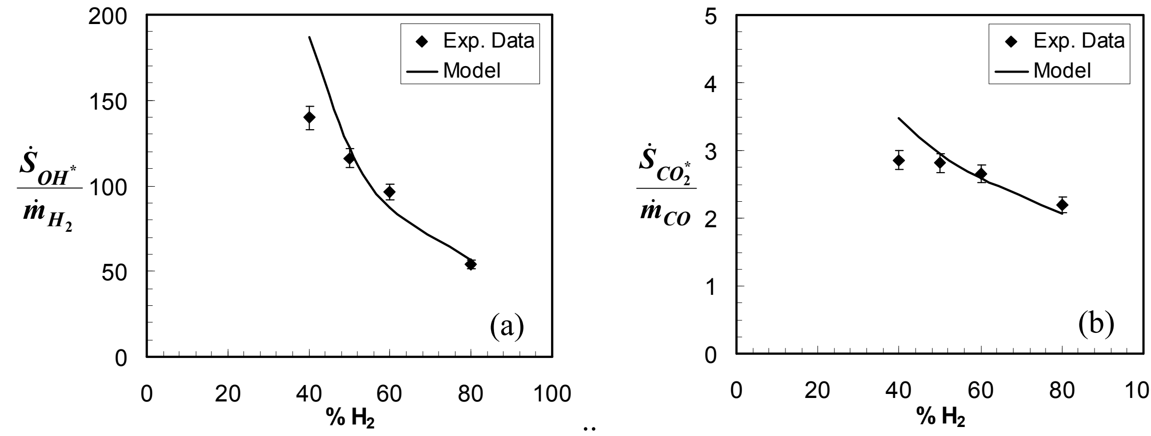

Figure 4.10. Measured and simulated normalized chemiluminescence at ϕ=0.6 for (a) OH* and (b) CO_2* in H_2:CO syngas mixtures with 40%, 50%, 60% and 80% Hydrogen, at 10atm and 598 K reactant preheat conditions.

Validation for different fuel compositions at high pressure is considered next. Results for the variation of normalized chemiluminescence with hydrogen content in the syngas mixture at the same operating conditions are given in Figure 4.10 for ϕ=0.6. The OH* and CO_2* simulations agree well with the experimental data, predicting them to within 5%, except for the 40% H_2 mixture, where the simulations over predict the data by 25%. The flame height for this mixture was only ~6 mm, i.e., just one burner diameter.

Even though the measure flame speed for this mixture [72] was within 5% of the value predicted by the C1 reaction mechanism, such a compact flame could be considerably affected by curvature, which could result in a reduction of the chemiluminescence signals [26,10]. However, it is interesting to observe that the CO_2*/OH* chemiluminescence ratio for this case was well predicted by the simulations (see Figure 4.8). The OH* and CO_2* signals were over-predicted by the same extent, thus not affecting the CO_2*/OH* ratio. Unfortunately, similar analysis could not be performed with the experimental data for the H_2:CO=33:67 mixture at 5 atm due to lack of reliable H_2 and CO mass flowrate data. Nevertheless, it can be concluded that the chosen OH* and CO_2* mechanisms can be considered validated at elevated pressure and preheat conditions, with the caveat that the pressure dependence may not be adequately modeled.

4.3 Thermal OH* Contribution

The above validations assume that the only contribution to the OH* signal is due to OH created in its electronically excited state through chemical reactions. Another possibility is that ground state OH is collisional excited. This is denoted thermal OH*. The relative contribution of thermally OH* to the total OH* signal is computed for the syngas flames experimentally investigated in order to evaluate its potential for systematic errors in the validation experiments. For all the syngas mixtures tested, the spatially integrated (10 mm) thermal OH* is determined at two extreme equivalence ratios: ϕ=0.7 and 1.0, using Eq. 4 (Chapter 2). The results are shown in Table 4.1. With contributions typically under a few tenths of a percent, and always less than two percent, it can be concluded that the effect of thermal OH* is negligible in the syngas validation experiments.

Table 4.1. Thermal OH* contribution (as percentage of the total OH* signal) in experimental syngas flames.

Syngas Mixture (H_2/CO) and Oxidizer	Operating Conditions	% Thermal OH (L_i=10mm)	
		ϕ = 0.7	ϕ = 1.0
95-5 (Air)	1 atm, 300 K	0.13	1.73
50-50 (Air)	1 atm, 300 K	0.3	1.28
33-67 (Air)	1 atm, 300 K	0.23	1.02
50-50 (Air)	1 atm, 500 K	0.5	1.72
50-50 (O_2/He)	10 atm, 600 K	0.27	5
33-67 (O_2/He)	5 atm, 300 K	<0.1	0.5
33-67 (O_2/He)	5 atm, 600 K	0.13	1.6

4.4 Self-Absorption of OH*Emission

If a molecule can emit light going from an excited state to a lower energy state, then the lower state can also be excited by light at the same wavelength, which lead to absorption. The self-absorption by ground state OH will lead to a decrease in the observed OH* signal. The importance of self-absorption is determined for the syngas mixtures at the different operating conditions used here. Estimates of the amount of self-absorption are calculated with Eq. 3 (Chapter 2) at two equivalence ratios: ϕ=0.7 and 1.0. A path length of 5 mm was chosen for the comparison, after which it was assumed that [OH] concentration rapidly decreased due to entrainment with cold gases surrounding our jet flames. Theses results are presented in Table 4.2. Self-absorption is less than a 10% effect at most conditions, though at high pressure and preheat conditions, it can be come more signficant. For example in the H_2:CO=50:50 syngas fuel at 10 atm and 600 K, almost 20% of the signal is absorbed for the stoichiometric case (the high flame temperature at ϕ=1 leads to high OH equilibrium concentrations). At lower pressures and lean flames, self-absorption is generally less than a few percent. Thus we conclude that the large change in C_{OH*} observed at high pressures is not primarily due to self-absorption. There is some chance that it could be due to absorption by some other species. Similarly, there may be some absorption of the CO_2* chemiluminescence by CO_2 or other molecules (Chapter 2). However, it is not likely that the absorption is large, as it would be due to a broadband absorber.

Table 4.2. Fraction of OH* signal absorbed in experimental syngas flames.

Syngas Mixture (H_2/CO) and Oxidizer	Operating Conditions	% Absorption (L_i=5mm)	
		$\phi = 1.0$	$\phi = 0.7$
95-5 (Air)	1 atm, 300 K	8.4	4
50-50 (Air)	1 atm, 300 K	6	3.6
33-67 (Air)	1 atm, 300 K	5	3
50-50 (Air)	1 atm, 500 K	7.5	5
50-50 (O_2/He)	10 atm, 600 K	19	8
33-67 (O_2/He)	5 atm, 300 K	7	3
33-67 (O_2/He)	5 atm, 600 K	12	7

In summary for syngas fuels, mechanism for both OH* and CO_2* chemiluminescence have been validated. For CO_2*, the global mechanism given in Eq. (11) (for 375 nm detection) provides excellent results for changes in equivalence ratio (at least for lean flames), preheat temperature and dilution. For OH*, R1 appears to be the predominant production pathway, and the temperature dependence of the rate constant given in [37] produces accurate results. While both the OH* and CO_2* mechanisms produced generally excellent agreement with the experiments, the scaling constant used for matching the simulation results with experimental data changed with pressure. This is likely due, at least in part, to inaccuracies in the basic chemical mechanisms used to simulate the laminar flames at high pressure. Another likely source for the discrepancies is radiative trapping (absorption) of the ultraviolet emissions by CO_2 and H_2O at high pressures. Thermal production and self absorption of OH* are not significant in the validation experiments.

CHAPTER 5

HYDROCARBON FUEL VALIDATIONS

This chapter continues from the foundation laid in the previous chapter, with a goal of identifying the important chemiluminescence formation reactions, and appropriate rate constants, for OH*, CO_2* and now CH* in lean hydrocarbon combustion. The validation experiments were carried out primarily in laminar flames, though swirl combustor data for methane are presented for atmospheric conditions. First, validation results in methane flames (Section 5.1) are presented at atmospheric pressure (Section 5.1.1) and elevated pressure (Section 5.1.2). In each section, results of OH* and CO_2* chemiluminescence mechanisms are discussed followed by validation results for the CH* mechanisms. Possible uncertainties associated with thermal excitation for OH* and CH* are also presented along with a discussion on self-absorption (Sections 5.1.3-5.1.5). Finally, chemiluminescence from all three species are studied in laminar premixed, prevaporized Jet-A flames (Section 5.2).

5.1 Methane Validation

5.1.1 Atmospheric Pressure

With the chemiluminescence mechanisms validated for H_2-CO fuels in the previous chapter, the next step is consideration of additional mechanisms and species for hydrocarbon combustion. This includes addition of the R3 formation reaction ($CH+O_2 \rightarrow OH^*+CH$, Table 2.1) to the OH* mechanism, and a study of the CH* chemiluminescence mechanisms (Table 2.2). These studies focused on methane due to its wide-spread usage and well-studied kinetics. The methane data were acquired in laminar jet flames and a turbulent, swirl combustor. Thus, these experiments are not only a test of the validity of the modeling for laminar flames, but to some extent their applicability to more complex systems. Additionally, the laminar methane flame data is used for determining the ratios of the rate constants for R1 and R3 (i.e. k_1/k_3), by comparing them with the laminar syngas flame data.

5.1.1.1 CO_2* and OH* Chemiluminescence

The sensitivity of the simulation results to the integration length is illustrated in Figure 5.1 for a $\phi = 0.8$ methane-air flame. For this comparison, the simulation employed the R1 OH* formation reaction with the rate constant from [37] (the step validated in the previous section) and R3 with the rate constant from [45]. As before, the spatially integrated heat release rate, and OH* and CO_2* intensities are shown as a function of spatial integration length (top axis) through the 1-d flame. The corresponding flow times are shown on the bottom axis. The origin for the integration is, as before, the start of the reaction zone. In addition, the values were normalized by the integrated value achieved at 33 mm (14 ms).

While the heat release begins first, the integrated OH* chemiluminescence rises more rapidly, suggesting that most of the OH* chemiluminescence occurs within the primary reaction zone. It plateaus quickly, within ~1 ms or 2.5 mm after the start of the reaction zone. Thus there is little change (<1%) in I_{OH^*} with longer integration distances (or times). On a relative basis, the CO_2* chemiluminescence extends farther into the post-flame burnout zone due to the formation of CO_2* via recombination of CO and O atoms in the near-equilibrium hot products. Therefore, $I_{CO_2^*}$ increases by ~15% if the integration distance (time) is increased to 12 mm (5 ms). Similar results are found for other lean mixtures. For mixtures very close to stoichiometric, there is a more significant sensitivity to integration distance. At ϕ=1, I_{OH*} changes by 3% for L_i=2.5-12 mm (t=1-5 ms), while $I_{CO_2}*$ increases by nearly 33%. Thus, the CO_2* simulation results are somewhat dependent on the integration choice, and it can be expected that the comparison between the simulations and experiments may worsen near stoichiometric conditions, mainly due to uncertainty in predicting $I_{CO_2}*$.

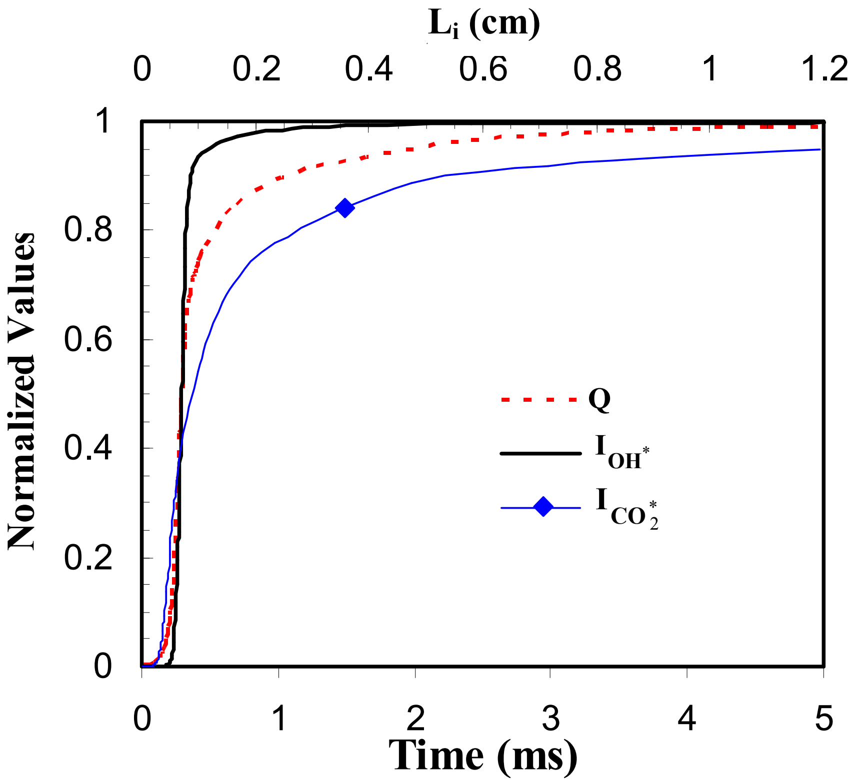

Figure 5.1. Simulation results of normalized integrated heat release rate, normalized integrated OH* and CO_2* chemiluminescence signal profiles.

For the laminar jet flames, an integration length L_i=10 mm was used.* In the swirl combustor, an integration length *per se* cannot be defined as the streamlines are convoluted due to turbulence. However, the nominal residence time (t_R) can be used to determine the appropriate integration time. The light is collected from a conical region that changes little with equivalence ratio and is nominally 52 mm in diameter at the center plane of the combustor. As the bulk cold flow velocity in the combustor is ~5 m/s, it can be estimated that the product gases would be moving through the combustor at ~25 m/s. This gives a residence time of ~2 ms in the combustor, which is the value used for the validation comparisons.

As before, the chemiluminescence ratios are compared first. It should be noted that many of the earlier studies indicated R3 as the main contributor of OH* in hydrocarbon flames and most researchers have assigned R3 a temperature independent rate constant except for the recent shock tube study [45], which suggested a weak dependence at flame temperature conditions. Thus two rate constants for the $CH+O_2$ reaction (given in Table 2.1) were considered; one of which is temperature dependent. Results are shown for the laminar and turbulent swirl flames in Figure 5.2. The uncertainty in the experimental data is indicated by the error bars, which represent a ±1σ deviation in the rms of the data. .

The results for the swirl flame are shown in Figure 5.2a. The maximum uncertainty in the chemiluminescence intensity and equivalence ratios was approximately ±12% and ±1.5%. The best match is provided by the rate constant suggested in [7], with a

---

*The same value used for the atmospheric syngas flames.

worst case deviation from the experimental data of 25%, which occurs near the lean blow out limit of the combustor and at the near stoichiometric condition. Even the simulation results using R3 [45] predict within 15% for most of the experimental data and are at least as accurate again near the lean blow out limit of the combustor and the near stoichiometric conditions. Both the simulations and experiment show a relatively small change in the chemiluminescence ratio with stoichiometry over the range $0.7<\phi<1$.

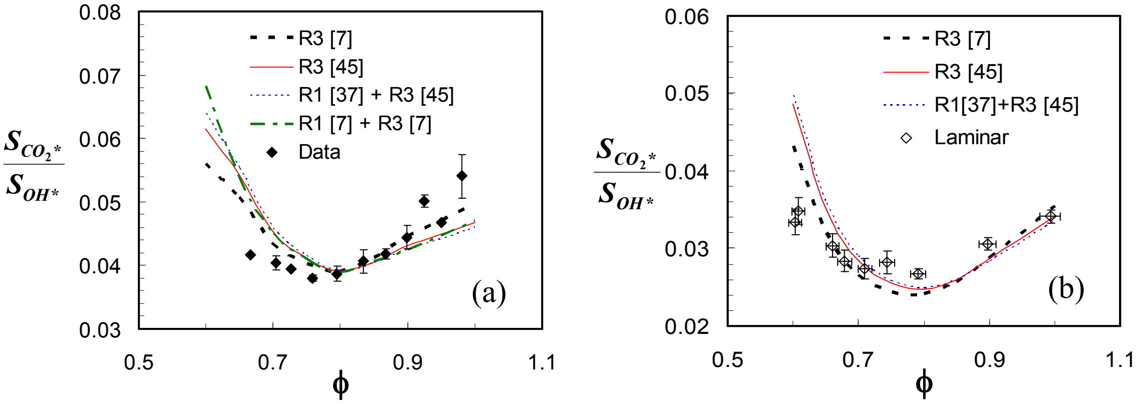

Figure 5.2. OH* model validation: chemiluminescence intensity ratio predictions in (a) swirl combustor and (b) laminar methane flames at p=1 atm and 298 K.

It is interesting to note that the temperature independent rate constant [7] for R3 alone does a remarkable job of predicting the data, even better than the rate constant given in [45]. However, it should be noted that with the current experimental capability, only the relative levels of the chemiluminescent species can be measured as opposed to the absolute levels provided by the mechanisms. A best fit for the simulation using the rate constant from [7] was obtained with $C_{\text{det}}=5.7$ (the values for the other case [45] was $C_{\text{det}}=144$). The large change in C_{det} from the syngas results ($C_{\text{det}}=20.1$) suggests some inaccuracy in the pre-exponential factors estimated in the original references. The results also show that R3 alone would nearly suffice to model OH* emission under the current operating conditions. According to the simulations, formation reaction R1 contributes

6–9% of the total OH* chemiluminescence in the range of equivalence ratios studied here. Thus, R1 should still be included.

If the rate constants for R1 and R3 from Smith *et al.* [7] are used, it can be seen that the model prediction closely follows the other mechanisms. However in that case, R1 contributes significantly, about 44–50% of the total OH* signal. In the hot product exhaust, where the CH radicals are essentially absent, the OH* signal is produced via the recombination of O and H (R1), but the experimentally observed emission is very weak there compared to that produced from CH in the reaction zone. Thus, the R1 and R3 rate constants from Smith *et al*. [7] can be considered invalid even though the overall model predictions for the signal ratio differ little from the other mechanisms.

The chemiluminescence intensity ratios from the atmospheric *laminar* methane flames are shown in Figure 5.2b. The same rate constants considered for the turbulent flames are again employed here, except for the Smith *et al*. [7] values. The model predictions are again similar; for $\phi>0.6$, all the mechanisms predict the data within 5-10%. For $\phi<0.8$, the predictions from the two mechanisms using R1 [37] and R3 [45] estimated from the shock tube studies consistently deviate by 10–15% from the predictions using the temperature independent R3 [7] alone. This latter mechanism produces excellent agreement with the data over the whole range except at $\phi=0.6$, where the predictions are higher than the experimental data by 25%. For the other mechanisms, the deviation from the experiments is ~45% at $\phi=0.6$. Therefore, considering the results from the *swirl* and *laminar* flames, a temperature independent R3 rate constant combined with the R1 mechanism from the syngas validation appears to be a good choice for modeling OH* in hydrocarbon fuel combustion.

This conclusion is tested by normalizing the chemiluminescence signals with the mass flow rate of fuel (Eq. 19) and comparing to the predictions for two mechanisms: 1) R3 alone with a temperature independent rate constant, and 2) R3 with a temperature dependent rate constant [45] and combined with the validated R1 mechanism [37].

$$\frac{S_{OH^*}/\Delta t_E}{\dot{m}_f} = \frac{\dot{S}_{OH^*}}{\dot{m}_f} \approx \frac{C_{OH^*}}{L^2}\left\{\frac{1+{}^{\dot{m}_a}\!/\!_{\dot{m}_f}}{\rho_u S_L}\right\} I_{OH^*} \tag{19}$$

The results for both the laminar and swirl methane flames are displayed in Figure 5.3a. As noted above, the integration distance/time should not have a large influence on the results of the comparisons. The normalized OH* signals obtained from the laminar flames are scaled by a single multiplicative constant to account for experimental differences in order to match the swirl data. As seen in Figure 5.3a, both mechanisms are able to simulate the measured normalized OH* signals within the experimental scatter. However, at the leaner equivalence ratios, both mechanisms consistently under-predict the experimental data, thus causing the higher chemiluminescence ratios seen in Figure 5.2. Nevertheless, the simulations are in excellent agreement with the experiments. This makes it difficult to identify the correct temperature dependence for R3.

The normalized results for CO_2* emission in both the atmospheric laminar and swirl methane burners are displayed in Figure 5.3b. As with the OH* data, the laminar flame CO_2* data are scaled by a single multiplicative constant to match the swirl combustor results. The CO_2^* predictions, like the OH* predictions, are within the experimental uncertainty over most of the ϕ range. As the CO_2* emission is more sensitive than OH* emission to the integration distance/time, there can be a noticeable

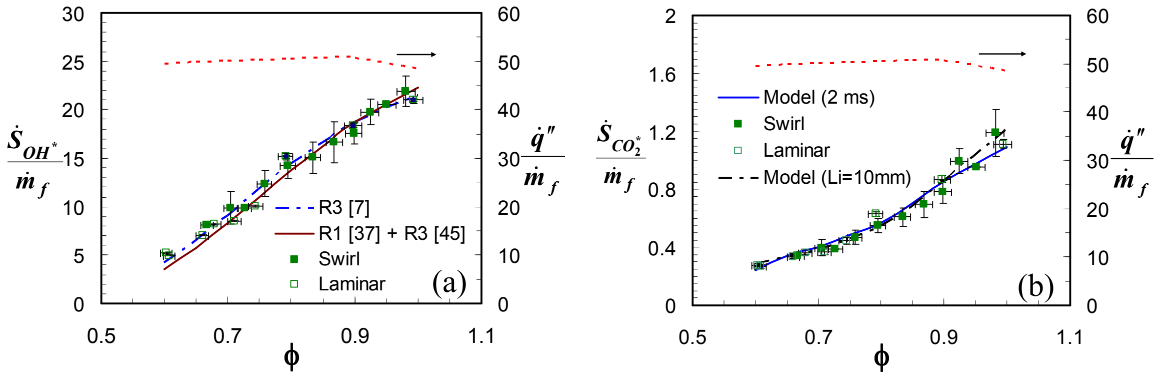

Figure 5.3. Comparison between measured and simulated normalized chemiluminescence for a) OH* emission and b) CO_2* emission in methane flames.

change due to this parameter. The difference between the two can be clearly observed in the simulation results for the near stoichiometric conditions in Figure 5.3b. At this condition, the simulations with the reduced integration (2 ms) fall below the longer (10 mm ≈ 4 ms) simulations by about 12%. Still, we can conclude that the chemiluminescence mechanisms identified here are reasonably accurate and can be used with appropriate chemical kinetic mechanisms to analyze the chemiluminescence signals from CO_2^* and OH^* in flames with H_2/CO/CH_4 fuels, and possibly with other simple hydrocarbons (at least for the atmospheric conditions tested up to this point in the thesis).

It is also interesting to note the variation in normalized chemiluminescence signal with changes in equivalence ratio. Over the range investigated, the normalized OH* signal increases nearly linearly with ϕ, while the CO_2* signal appears to have a higher (power law) dependence. Figure 5.3 also shows the normalized heat release rate determined from the simulations; as expected, it is almost independent of equivalence ratio for lean mixtures. Thus it can be concluded that while the OH* and CO_2* signals are correlated to the flame's heat release, the relationship varies with equivalence ratio.

Finally, the agreement between the swirl combustor data and the laminar results (data and simulations) is quite remarkable. Clearly the swirl combustor is turbulent. As noted in Chapter 3, the turbulent combustion can be characterized as either corrugated flamelets or thin reaction zones. Thus the similarity between the laminar and turbulent results suggests the turbulence effects on the flame, at least in this case, do not strongly alter the dependence of the chemiluminescence on equivalence ratio.

5.1.1.2 Relationship between the rate constants of R1 and R3

At this juncture, it is appropriate to further explore the laminar methane and syngas data to establish a relationship between the rate constants of R1 and R3. For this comparison to be meaningful, the OH* signals (for both syngas and methane flames) were acquired with an identical intensifier gain setting of 200. Modifying Eq. (19), we find

$$\frac{S_{OH^*}/\Delta t_E}{\dot{m}_f} = \frac{\dot{S}_{OH^*}}{\dot{m}_f} \approx \frac{C_{OH^*}}{L^2}\left\{\frac{1+{}^{\dot{m}_a}\!/\!{}_{\dot{m}_f}}{\rho_u S_L}\right\} I_{OH^*} \approx C_{OH^*}\left(\int_0^{l_f} k_1 f + \beta\int_0^{l_f} k_3 g\right) h \tag{20}$$

where *f* and *g* are functions of species concentrations related to R1 and R3 chemistry and *h* is a function of experimental factors such as solid angle, detector settings, flame speed, fuel-air ratio etc. In general, k_1 and k_3 are functions of temperature and hence vary along the flame axis. The idea is that if the model predictions are correct, the multiplicative constant C_{OH^*} should be the same in scaling both syngas and methane simulations in order to match the experimental data, for a given factor β. This would indirectly give the relative scaling between the rate constants for R1 and R3. In syngas flames, $g = 0$, as OH* is [CH] is essentially zero, and C_{OH^*} can be estimated. Using the same C_{OH^*} to match the methane experimental data should yield β, and $k_3\beta$ can be considered as the new rate constant for R_3.

With the rate constant for R1 [37] and R3 [45] in Eq. (20) and matching the experimental data yields β~0.36. So, k_3 [45] has to be reduced to $k_3\beta$ to match the experimental data. This establishes the relative scaling of the rate constants of R1 and R3. or in other words, the ratio k_1/k_3 is determined. Similarly, if the temperature independent rate constant for R1 [7] was used in Eq. (20), then β would be ~ 4.7, i.e., in this case k_3 [7] has to be increased to match the experimental data. Here, a constant k_1/k_3~43 is obtained. If a temperature range 1500-1800 K is considered, where most of the OH* is produced (for all the lean fuel-air mixtures), and the new value for k_3 used, the ratio k_1/k_3 varies over ~37-47 for rate constants k_1[37] and k_3[45]. Interestingly, this ratio is 43 if the temperature independent rate constants were considered. This ratio k_1/k_3 can be considered universal and can be used in other hydrocarbon fired combustors for estimating OH* chemiluminescence.

At this point, it would be interesting to consider the range of values taken by k_1 and k_3, and based on the above analysis try to determine this range of values more accurately. A temperature of 1800 K shall be considered without loss of generality. In the literature k_1 varies from 3.36×10^{13} to 8.62×10^{13} $\text{cm}^6/\text{mol}^2/\text{s}$ (a factor of 3) at 1800 K and is known with better accuracy than k_3, whose predicted value changes by at least two orders of magnitude at the same temperature. So, assuming k_1/k_3 ~ 47, and k_1 to be in the above range of values, k_3 is estimated to be in the range 7.15×10^{11}–1.83×10^{12} $\text{cm}^3/\text{mol/s}$ at 1800 K.

Based on the above analysis, both temperature dependent and independent rate constants for R1 and R3 can be assigned as given in Table 5.1. The temperature dependent rates were derived from Petersen *et al,* [37,45] and this mechanism is denoted the Petersen-hybrid from now on. Similarly the temperature independent rates were derived from Smith *et al*. [7] and shall be identified as the Smith-hybrid in the thesis. Both these derived mechanisms excellently predict OH* chemiluminescence in atmospheric methane-air flames. These derived mechanisms shall be further investigated when validating experimental data at elevated pressure and preheat conditions.

Table 5.1. Suggested OH* formation reactions and their rates. Rate coefficients are expressed as $k=AT^b exp(-E_a/RT)$ with E_a in units of cal mol^{-1} and AT^b in cm^{3}mol^{-1}s^{-1} for two body reactions or cm^{6}mol^{-2}s^{-1} for three body reactions (with T in K units).

#	Reaction	*A*	*b*	E_a	Ref.
R1	$H + O + M \leftrightarrow OH^* + M$	6×10^{14}	0.0	6940	Petersen Hybrid
		3.63×10^{13}	0.0	0.0	Smith Hybrid
R3	$CH + O_2 \leftrightarrow OH^* + CO$	1.17×10^{14}	-0.4	4150	Petersen Hybrid
		8.47×10^{11}	0.0	0.0	Smith Hybrid

5.1.1.3 CH* Chemiluminescence

Methane flames provide a good opportunity for validating CH* chemiluminescence mechanisms for hydrocarbon systems, primarily due to the availability of a well-validated combustion mechanism for methane. In this section, the reported chemiluminescence mechanisms for CH* are examined and validated with experimental data.

In this study, four mechanisms proposed in the literature (designated by the last author of the reference source) were used to model CH* in methane flames. Each is based on two of the formation reactions (R5-R7); the reaction rate parameters associated with each are listed in Table 2.2. Of the four proposed CH* mechanisms considered, three (Peeters [64], Carl [66] and Smith [40) are based on formation steps R6 and R7. The Peeters mechanism has temperature independent rate constants, while the Carl mechanism is an updated version that adds temperature dependence to both formation rates but matches the large rate constant ratio, k_2/k_3~500, of Peeters at ~650 K. However, it should be noted that k_2/k_3 in the Peeters mechanism is a constant, while in the Carl mechanism the ratio varies from 420 at 700 K to 15 at 2000 K. The Smith mechanism includes temperature dependence only for the O_2 step, and has a much lower k_2/k_3 value decreasing from 25 to 12 for the same 700-2000 K range. On the other hand, the fourth mechanism (Petersen [64]) uses R5 and R6. To use R5 with the GRI mechanism requires the addition of reactions for the production and destruction of C_2, as outlined in the same reference.

As with OH* and CO_2* chemiluminescence, CH* chemiluminescence was acquired both in atmospheric-pressure laminar and swirl burners. Earlier, a residence time of ~2 ms was established for comparisons to the swirl burner, while an integration length of 10 mm was used for the laminar flame case. For comparing simulated CH* chemiluminescence to the data, however, it is sufficient to use one integration length (10 mm ≈ 4 ms) in both burners. This is due to the fact that CH* is formed only in the narrow region where C_2H or C_2 is present, i.e., in the primary reaction zone for the lean methane-air flames.

As before, we start by examining chemiluminescence signal ratios. As the OH* chemiluminescence is almost completely associated with the primary reaction, like CH*, it as chosen for the ratio comparison. Also as the OH* chemiluminescence mechanism

(Table 5.1) was validated above, the CH*/OH* ratio comparison should directly reveal the accuracy of the CH* mechanisms considered. The measured chemiluminescence signal ratio is related to the simulated value through the expression below.

$$\frac{S_{CH*}}{S_{OH*}} = C_{\det}\frac{I_{CH*}}{I_{OH*}} \tag{21}$$

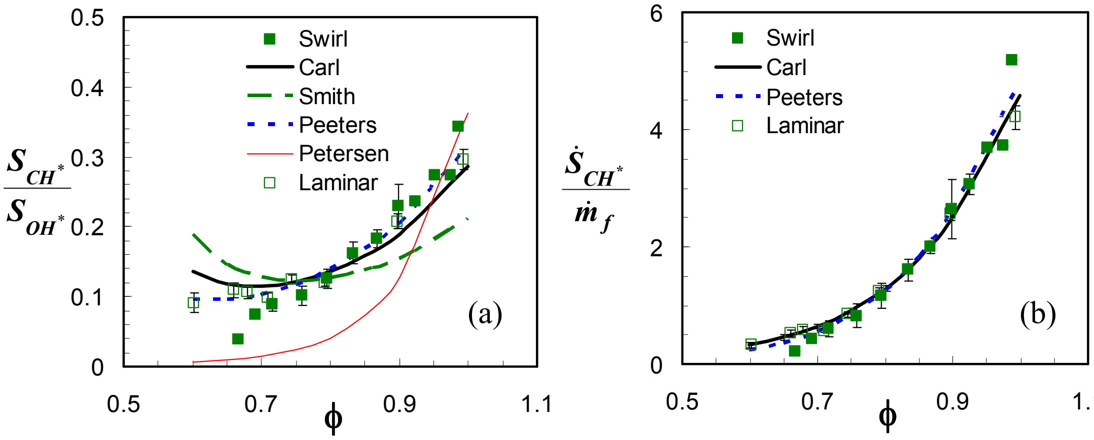

Figure 5.4. Comparison between experimental results and model predictions for a) CH*/OH* chemiluminescence intensity ratio and b) normalized CH* emission in methane flames at 1 atm and 298 K.

Results for the CH*/OH* chemiluminescene ratio are shown for the swirl burner and laminar jet flames in Figure 5.4a. First, it is worth noting the excellent agreement between the laminar and swirl flame results, except near the lean blow out limit of the swirl combustor. The figure also includes the simulation results for the four mechanisms. The simulation results for each were multiplied with a chosen $C_{\det}$ such that the least square difference (across the ϕ range) is minimized. The best agreement with the experimental data is provided by the Peeters mechanism, which matches the laminar data across the complete range within the experimental uncertainty, and it matches the swirl data except near its lean blowout limit. The mechanism that includes the C_2 formation step (Petersen) provides the poorest overall match. It should be noted here that the lack of accurate rate kinetic information for C_2 formation and destruction reactions could be a significant cause for this disagreement. The somewhat poorer comparison produced by the Smith mechanism argues against its lower k_2/k_3 ratio. The Smith mechanism significantly over predicts the data, especially for $\phi<0.8$. The Carl mechanism does a reasonable job for $\phi>0.85$, but over predicts the data for lean mixtures. Thus both the Petersen and Smith mechanisms can be eliminated without further investigation.

The relatively good agreement between the Peeters and Carl mechanisms is further investigated by considering the variation of normalized CH* chemiluminescence signal with equivalence ratio as shown in Figure 5.4b. Experimental and simulated CH* chemiluminescence signals, normalized by fuel flow rate, used for the validation can be compared using Eq. (19) (replacing OH* with CH* values). The simulation results for each were multiplied with a given C_{CH*} in order to minimize the overall deviations (the least square difference).[*] With this scaling, the agreement between the Peeters and Carl mechanisms is even more pronounced, in spite of the inherent differences in the temperature dependence of the reaction rate constants for R6 and R7.

The agreement between the Peeters and Carl mechanisms, with their different temperature dependence for k_2/k_3 occurs due to a offsetting change in the concentration ratio $[O]/[O_2]$ and k_2/k_3 for the Carl mechanisms in the methane flames studied. For the Peeters mechanism, R2 dominates CH* production in the lean (atmospheric) methane flames, and the formation of CH* is essentially given by $k_{2,P}[C_2H][O]$. For the Carl

---

[*] This does not provide validation of the absolute values for the reaction rate constants, since the absolute responsivity of the detection system are not known.

values ($k_{2,C}$ and $k_{3,C}$), both reactions are important; thus the ratio of the CH* chemiluminescence for the two mechanisms scales like $\frac{k_{2,P}}{k_{2,C}} \bigg/ \left(1+\frac{k_{3,C}}{k_{2,C}}\frac{[O_2]}{[O]}\right)$. Since $k_{2,P}/k_{2,C}$ is a constant (~1.8), the two mechanisms will give the same result if k_2/k_3 for the Carl mechanism varies with temperature in a similar fashion to $[O_2]/[O]$, which turns out to be the case in our flames.

In summary, the best agreement with the experimental results is provided by the Peeters (temperature independent) rate constants, though simulations with the Carl (temperature dependent) rate constants are nearly as good. Overall, the results suggest that either the Carl or Peeters mechanisms could be used to predict CH* chemiluminescence in atmospheric methane-air flames.

5.1.2 Elevated Pressure

Experimental measurements of flame chemiluminescence at elevated pressure can help in evaluating the robustness of the chemiluminescence mechanisms, and in the case of OH* and CH*, may also help in differentiating the best candidates determined in the atmospheric experiments. Therefore, data was acquired in 5 and 10 atm laminar methane flames. OH*, CH* and CO_2* chemiluminenscence was acquired at room temperature conditions at both pressures, and with 598 K reactant preheat at 5 atm. As with the syngas experiments, a O_2:He oxidizer mixture (1:5) was used to aid in flame stabilization at high pressure conditions. The San Diego mechanism [76], which includes helium, was used instead of GRI Mech 3.0, to simulate the flames.

5.1.2.1 CO_2* and OH* Chemiluminescence

As in the previous cases, the sensitivity of the simulated chemiluminescence signals to integration length is examined first. Example results for ϕ=0.8 are shown in Figure 5.5. The OH* chemiluminescence is simulated with the R1 and R3 rate constants given in Table 5.1, with the values normalized by the integrated value achieved at 5 cm downstream of the reaction zone.

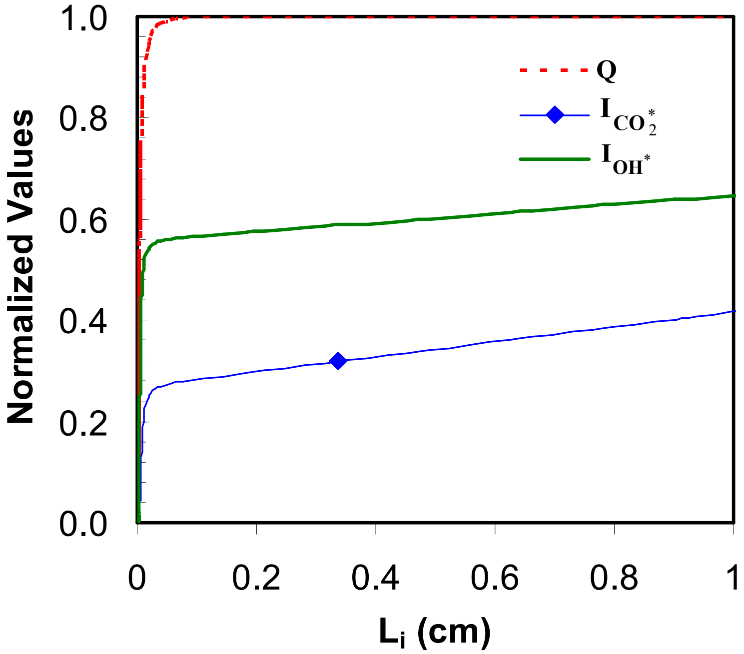

Figure 5.5. Simulation results of normalized integrated heat release rate, normalized integrated OH* and CO_2* chemiluminescence signal profiles in a methane flame at 10 atm and room temperature conditions. The equivalence ratio is 0.8.

High pressure flames are generally characterized by extremely thin reaction zones, and this can be clearly inferred from the heat release rate profile in Figure 5.5. The heat release approaches a plateau value, within a few hundred micrometers after the start of the reaction zone. The reaction zone is also thinner than that of the high pressure syngas flame presented in the last chapter. In high pressure methane flames, the post-flame product gases are a source of both OH* and CO_2* chemiluminescence, due to the formation of OH* via R1 (O+H+M) and CO_2* via CO+O.

To aid in determining the integration length for the simulations, flame chemiluminescence images were also acquired with the same ICCD camera employed in the high pressure syngas experiments. Now, however, the intensity at any pixel is potentially due to a combination of all three sources (OH*, CH* and CO_2*). As the product zone's contribution to the total OH* and CO_2* chemiluminescence signal significantly increases for near stoichiometric flames, a methane flame image for a 10 atm, 298 K and ϕ=0.97 is shown in Figure 5.6a. The raw image shows a much more significant contribution (to the total OH*and CO_2* signals) from the hot products, especially for regions near the flame tip. Horizontal cuts at two locations along the flame height are shown in Figure 5.6b, one at 20% and the other at 80% of the flame height. In each of the plots, the peaks indicate the approximate flame location. From the results lower in the flame, the signal intensity is seen to drop to ~4% of the peak value at 2 mm from the flame. For the higher location, the intensity drops much less rapidly, only to ~30% of the peak signal at 3.6 mm from the flame. This clearly confirms the contribution of the hot product region to the total chemiluminescence signal particularly for near stoichiometric flames.

It can also be inferred that an integration distance of 5 mm for the lower half of the flame and at least 10 mm for the upper half of the flame would include most of the exhaust regions where OH* and CO_2* chemiluminescence signals are produced. For L_i=5−10 mm; I_{OH*} changes by about 4%, while I_{CO2*} change by nearly 6%. Still, this can be characterized as a mild dependence on integration distance between 5 and 10 mm.

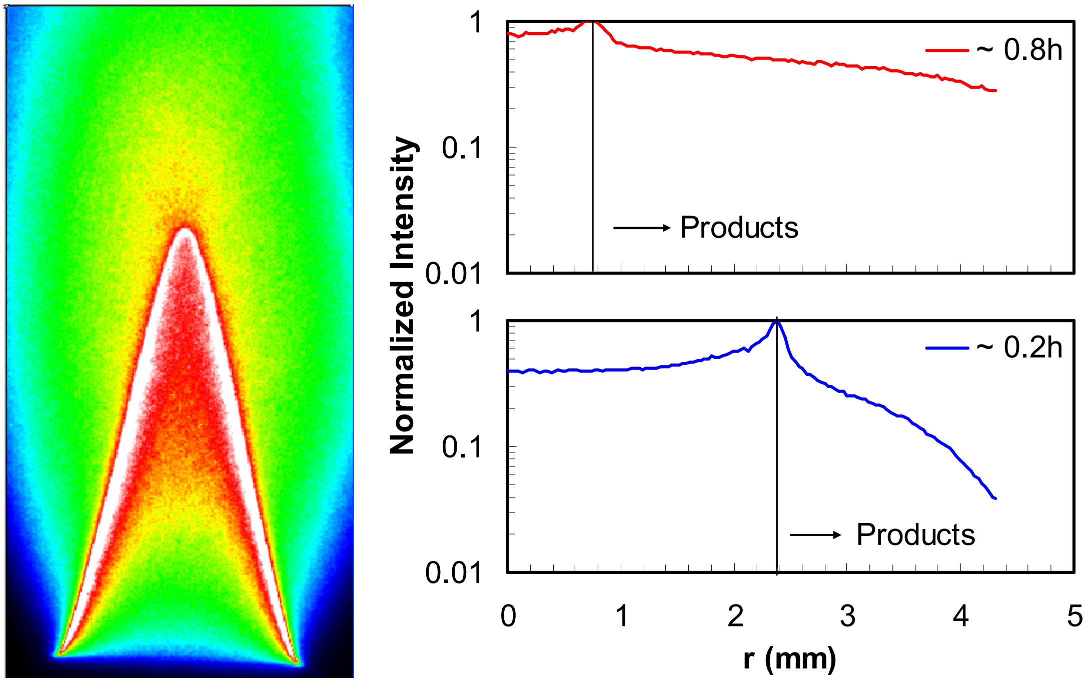

(a) (b)

Figure 5.6. Chemiluminescence image analysis for a methane flame at 10 atm, 298 K and ϕ=0.97. (a) Raw image (burner diameter is 6 mm) and b) radial (line of sight) Intensity profiles from the burner center axis, at 20% and 80% of the flame height.

Similar results are found for other lean mixtures and for the flames at 5 atm. For near stoichiometric mixtures, a greater fraction of the chemiluminescence is produced in the high temperature product gases, similar to that observed in atmospheric conditions. At ϕ=1, and at identical operating conditions, I_{OH*} changes by about 8% for L_i ranging from 5–10 mm, while I_{CO2*} increases by about 9%. Since the lean cases showed little sensitivity to the choice of integration length, an L_i of 10 mm was chosen for the high pressure validations.

For the comparisons to the high pressure data, OH* chemiluminescence was modeled with two mechanisms, both include R1 and R3. The mechanisms are given in Table 5.3 and the difference lies in whether both R1 and R3 have temperature independent rate constants (Smith hybrid) or temperature dependent rate constants (Petersen hybrid). Again, only one mechanism for CO_2* is considered.

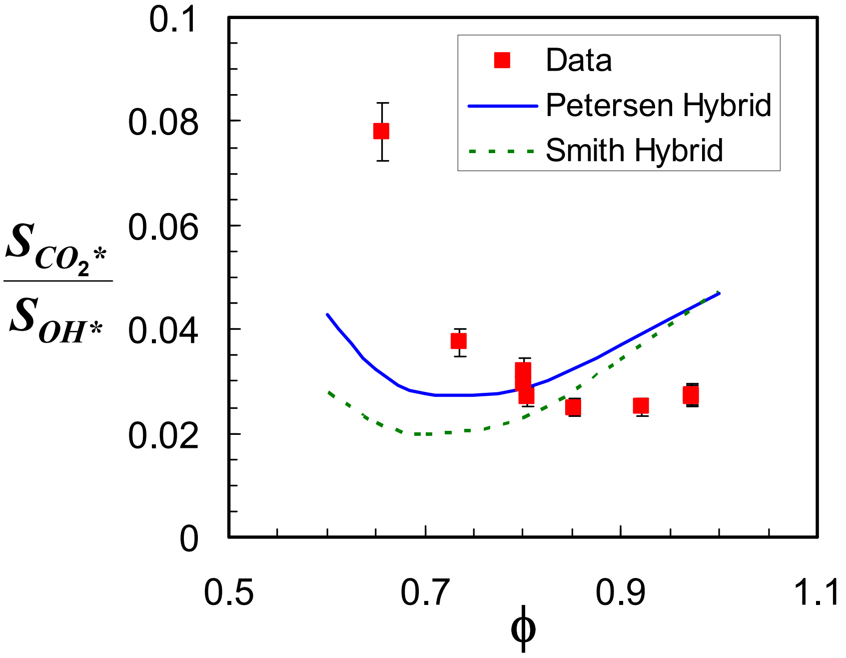

Figure 5.7. OH* model validation in methane flames at elevated pressure conditions: chemiluminescence intensity ratio predictions for flames at p=10 atm and 298 K.

Results for the CO_2*/OH* chemiluminescence ratio in a methane flame at 10 atm and 298 K are shown in Figure 5.7. The two simulation results are multiplied by values of C_{det} such that they match for a stoichiometric mixture. It can be seen that none of the mechanisms seem to predict the equivalence ratio variation of the CO_2*/OH* chemiluminescence intensity ratio. The experiments depict almost a monotonic decrease while the models predict a non-monotonic variation of the CO_2*/OH* ratio. While the results point out to the possibility of errors in the OH* or CO_2* mechanisms, the chemiluminescence signals have to be considered separately to determine where the problem lies. For this reason, the OH* and CO_2* chemiluminescence signals were normalized with the fuel mass flow rate, and the results are shown in Figure 5.8.

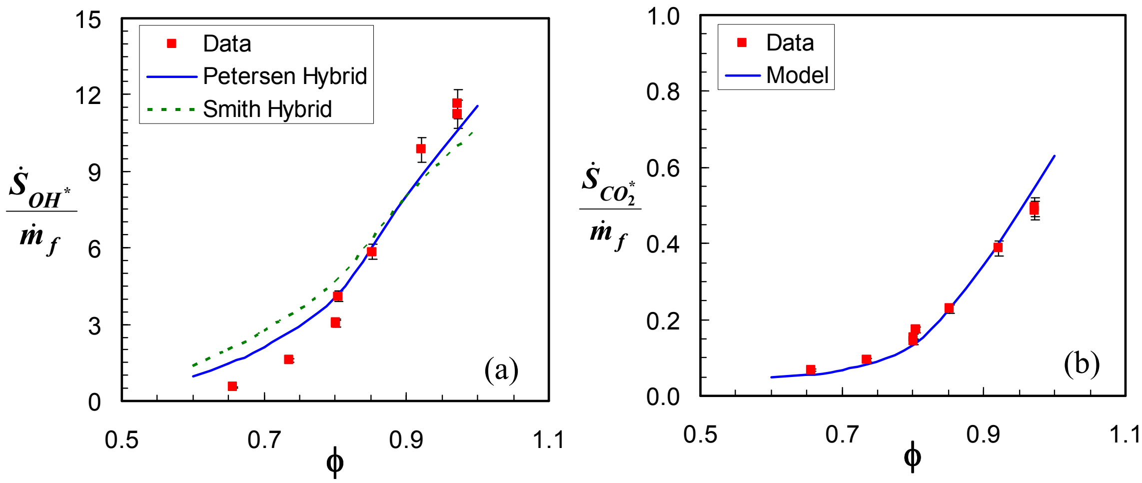

Figure 5.8. OH* mechanism validation in methane flames at elevated pressure conditions: (a) normalized OH* emission and (b) CO_2* emission for flames at 10 atm and 300 K reactants.

First, it can be seen that both OH* mechanisms are less accurate at these conditions but the Petersen hybrid mechanism provides better predictions than the Smith hybrid, likely due to the temperature dependent rates it employs for R1 and R3. On the other hand there is excellent agreement between the simulations and the experiments for the CO_2* chemiluminescence. So, it is most likely the inability of the OH* mechanism to predict OH* chemiluminescence accurately that caused the discrepancy in the CO_2*/OH* chemiluminescence intensity ratio results as presented in Figure 5.7. The measured OH* variation with ϕ is more dramatic than predicted by either mechanism.

Comparisons for the simulations (with the Petersen hybrid OH* mechanism) with all the methane experimental data obtained at high pressure are shown in Figure 5.9 (CO_2*/OH* ratio) and Figure 5.10 (normalized signals). For the ratios, a value of 10 was used for the scaling constant C_{det}. The simulated ratios are in poor agreement with the experimental data; not only do they have the wrong trend with ϕ, they do not display the correct pressure dependence. The experiments indicate a negligible effect of pressure and

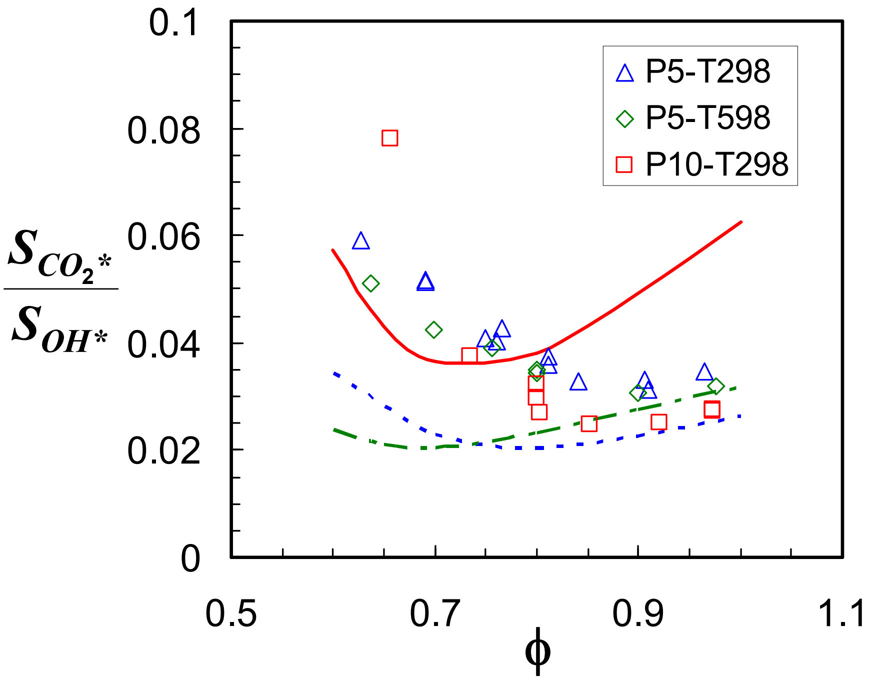

Figure 5.9. CO_2*/OH* chemiluminescence intensity ratios in methane flames at elevated pressure. Experimental data represented by symbols and simulation results depicted by lines: dashed line for 5 atm-298 K cases, dot dashed line for 5 atm-598 K case and solid line for 10 atm-298 K case.

preheat on the CO_2*/OH* chemiluminescence intensity ratio at these conditions.

Results for the normalized OH* and CO_2* chemiluminescence signals are shown in Figure 5.10. The OH* and CO_2* simulations were scaled by single values for C_{OH*} and C_{CO2*}, chosen to match the 10 atm-298 K experimental data. Both the OH* and CO_2* simulation results deviate significantly from the experimental behavior. While the trend with ϕ is qualitatively correct, both the OH* and CO_2* simulations fail to capture the pressure or preheat dependence. The OH* mechanism fails most for the preheated case, where the predictions are off by ~100%. On the other hand, the CO_2* mechanism shows little pressure dependence, unlike the experiments. It is interesting to note that reactant preheat has little effect on the measured OH* and CO_2* chemiluminescence at 5 atm.

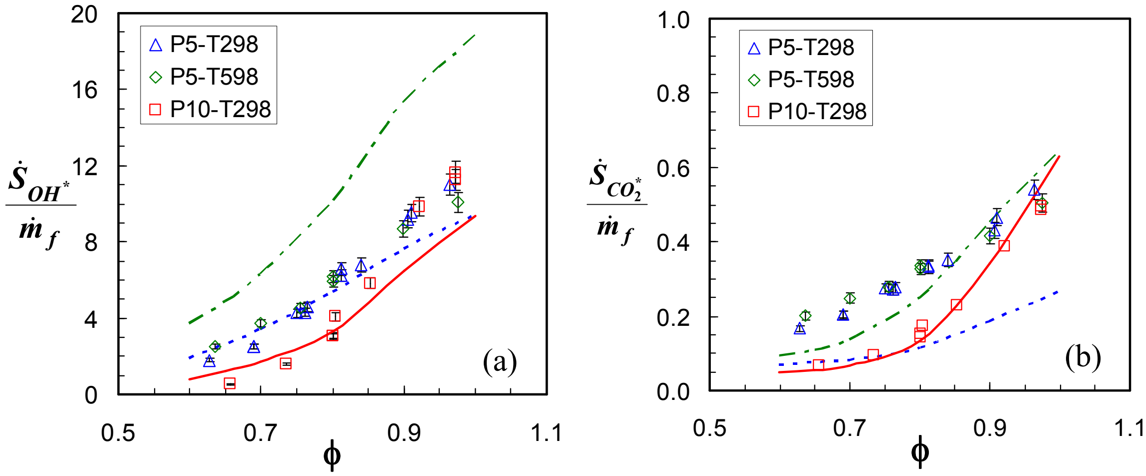

Figure 5.10. Normalized chemiluminescence signals in methane flames at elevated pressure: (a) OH* emission and (b) CO_2* emission. Experimental data represented by symbols and model predictions depicted by lines: dashed line for 5 atm-298 K cases, dot dashed line for 5 atm-598 K case and solid line for 10 atm-298 K case.

This discrepancy between the simulations and experimental data may be due to several causes. In the case of OH* for the room temperature conditions, the increase in OH* signal near stoichiometric conditions may be due to thermally produced OH*. Self-absorption of OH* by ground state OH molecules may become important at high pressure conditions and this aspect shall be further discussed in Section 5.5. As mentioned in Chapter 2, the ultraviolet OH* emission can also be absorbed by other molecules such as CO_2 and H_2O at high pressures. For the preheated case, the San Diego mechanism also consistently over predicts flame speeds by over 20% as compared to the experiments. So, there is a possibility that the mechanism might be over predicting the precursor species for OH* formation such as O, H, O_2 and CH, and this would directly impact the integrated chemiluminescence intensities. Also as significant fractions of both OH* and CO_2* are produced in the exhaust zone at high pressure according to the models, any difference in experimental conditions in the product gas zone such as product gas cooling

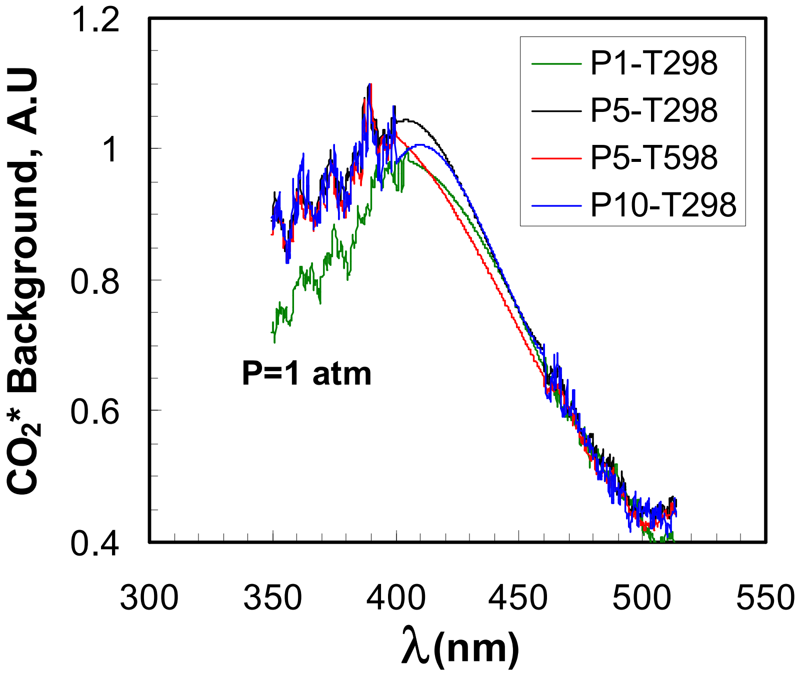

Figure 5.11. Spectral shape of the CO_2* continuum in methane flames at various pressure conditions at ϕ~075.

by N_2 entrainment could severly effect the measured OH* and CO_2* signals. Moreover, the results for CO_2* could also be explained if absorption of the CO_2* signal by the ground state was signficant. It is also possible that the CO_2* signal at 375 nm might be corrupted by other emitters such as HCO or water [57-59].

This can be partially verified by considering the "continuum" near the vicinity of 375 nm for the experiments considered. The "CO_2* background" for an equivalence ratio of 0.8 is considered for all the pressure conditions, and the results for scaled "CO_2* background" is shown in Figure 5.11. The spectral shape of the continuum at elevated pressure conditions is different than at atmospheric pressure. Moreover, there are clear, distinct peaks in the spectra near the vicinity of 375 nm, for all operating conditions which might suggest that other emitters are superimposed on the continuum.

It is also worth investigating the basic reaction mechanism (San Diego [76]) for methane combustion used here. The normalized OH* and CO_2* signals predicted by the San Diego mechanism are compared to those from GRI Mech 3.0 in Figure 5.12. GRI Mech 3.0 always predicts a higher OH* chemiluminescence signal than the San Diego mechanism. Additionally, the OH* signals predicted by the mechanisms do not have the same pressure or preheat temperature dependence. For example at 1 atm, OH* signal predicted by San Diego mechanism has to be multiplied by ~2.2 to match the GRI Mech results while this multiplicative constant changes to ~1.5 at 5 and 10 atm. So, it is possible that a similar phenomenon is explains the high pressure methane-O_2/He flames used here. In case of normalized CO_2* signal, the mechanisms produce excellent agreement at high pressure conditions but they differ significantly at atmospheric conditions. This suggests that both mechanisms predict the same CO and O profiles, but differ in their CH and H profiles.

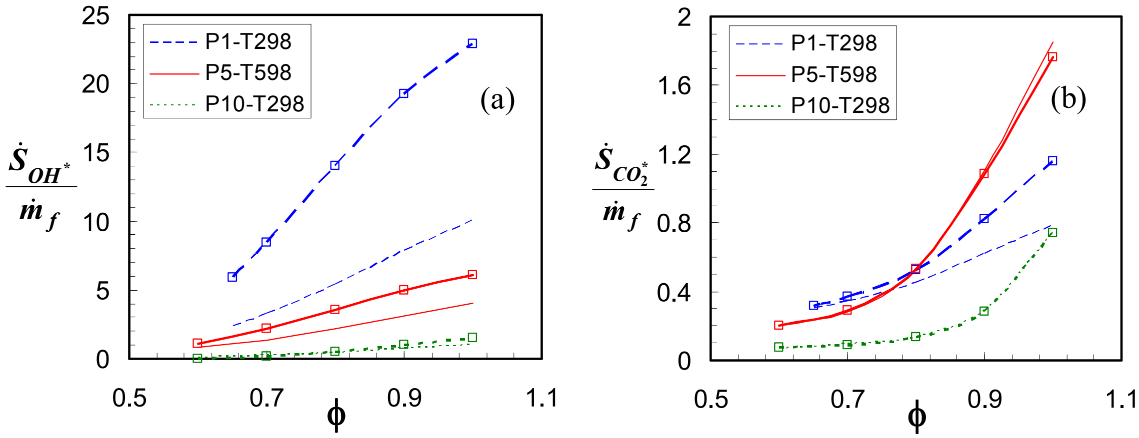

Figure 5.12. OH* and CO_2* model predictions with San Diego (lines) and GRI Mech 3.0 (lines with symbols) reaction mechanisms in methane air flames at various pressure and temperature conditions.

So, in conclusion, the Petersen hybrid mechanism can be used to qualitatively predict OH* chemiluminescence in methane flames at high pressure and preheat conditions. The CO_2* mechanism is not able to predict the intensity at 375 nm, possibly due to interferences (emission and absorption) from other species. Also further investigation into the production and destruction of CO_2* at various operating conditions may be required. However, both OH* and CO_2* mechanisms can be used to reasonably predict the chemiluminescence signals' equivalence ratio variation.

5.1.2.2 CH* Chemiluminescence

As CH* chemiluminescene occurs only in the reaction zone, any integration length (L_i) that exceeds the reaction zone thickness should be sufficient for modeling purposes. So, an integrated length L_i=10 mm was used as with the case of CO_2* and OH* chemiluminescence models. The CH*/OH* ratios at 10 atm and 298 K are shown in Figure 5.13a. The simulations use the Petersen hybrid mechanism for OH*, and the Peeters and Carl mechanisms for CH*. The Carl mechanism appears to better predict the

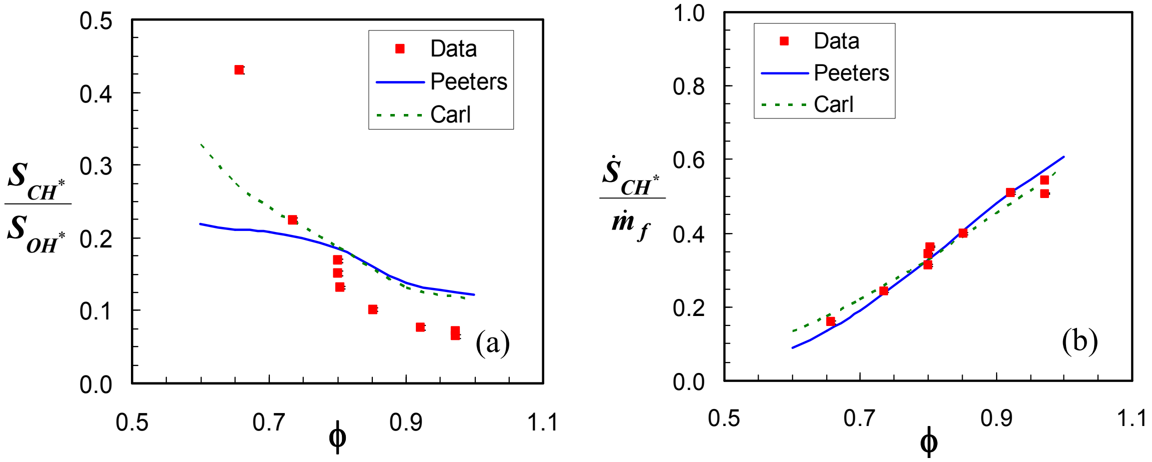

Figure 5.13. Comparison between experimental results and simulations for (a) CH*/OH* chemiluminescence intensity ratio and (b) normalized CH* emission in methane flames at 10 atm and 298 K.

experiments compared to the Peeters mechanism. However, the failure of the OH* mechanism makes the comparison problematic. So the variation of normalized CH* chemiluminescence is considered to further investigate the CH* mechanisms.

The normalized signals are shown in Figure 5.13b; the C_{CH^*} for both simulations were chosen based on a least-square error fit. Both the Carl and Peeters mechanisms predict the experiments with excellent accuracy, within the experimental uncertainty, despite their inherent differences in the temperature dependence of reactions R6 and R7. The deviation of the models from the experiments is at most ~15%. Still, the Carl mechanism slightly outperforms the Peeters mechanism, which over predicts the equivalence ratio dependence. So, the Carl mechanism is used further to examine CH* chemiluminescence in methane flames.

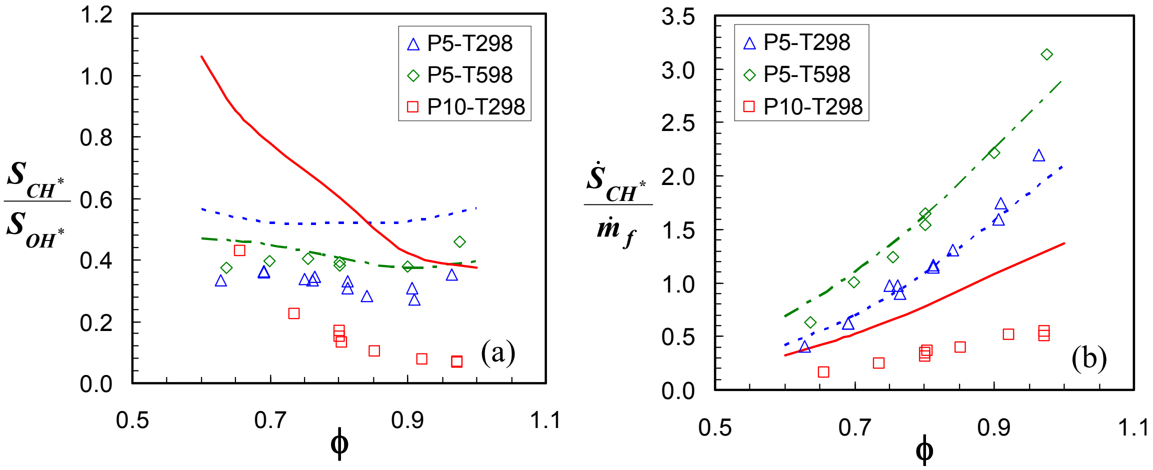

Figure 5.14. Validation of CH* chemiluminescence model in methane flames at elevated pressure: (a) CH*/OH* intensity ratio and (b) normalized CH* chemiluminescence signal. Experimental data represented by symbols and model predictions depicted by lines: dashed line for 5 atm-298 K cases, dot dashed line for 5 atm-598 K case and solid line for 10 atm-298 K case.

Results for all the experimental data obtained in the high pressure methane flames are shown in Figure 5.14, both CH*/OH* intensity ratios (Figure 5.14a) and normalized signals (Figure 5.14b). The simulations qualitatively agree with the change in the

CH*/OH* dependence on ϕ with pressure. At 1 atm, the signal ratio was seen to increase with ϕ, at high pressures this is reversed. The scaling constant C_{CH*} for the normalized signals is chosen to best match the experimental data at 5 atm without preheat. It can be seen in Figure 5.14b that the variation of the normalized CH* signal with ϕ is in good agreement with the experiments at 5 atm, with and without preheat. In addition, the model correctly captures the chemiluminescence increase caused by preheating. However, the CH* model predictions do not capture the drop in signal when the pressure is increased to 10 atm. This disagreement between the experiments and the model predictions can be due to several reasons. One of the important reasons could be due to the lack of accurate quenching rate information of CH* radicals at high temperature conditions [38]. The very small concentrations of ground state CH present in flames eliminates the possibility of self-absorption of CH* chemiluminescence by ground state CH radicals. Another possibility is that the San Diego mechanism has significant uncertainty in predicting the profiles for C_2H, the precursor for CH*. So, the San Diego mechanism predictions are compared with GRI Mech 3.0 in methane-air flames at similar pressure and temperature conditions. It can be seen in Figure 5.15 that the San Diego mechanism over-predicts the GRI Mech estimates for the normalized CH* signal. The CH* signals predicted by the mechanisms also do not scale well at different operating conditions. For example at 1 atm, the scaling constant to match the CH* signal predicted by San Diego mechanism with that of the GRI Mech 3.0 results is ~0.4. This scaling constant changes to ~0.65 at 5 atm and ~0.85 at 10 atm. Moreover, the variation of the CH* signal with equivalence ratio is also different for both mechanisms. At 10 atm and room temperature conditions, GRI Mech 3.0 predicts an increase of ~7.5 while the San

Diego mechanism estimates an increase of ~4 in the 0.6-1 equivalence ratio range. So, even though the reaction mechanisms match in their estimates of flame properties such as the laminar flame speeds or ignition delays with 10-15% accuracy, they could have significant disagreement in their estimates of flame chemiluminescence signals.

It can be concluded that given the experimental and modeling uncertainties, the CH* mechanism is able to qualitatively predict the experimental results satisfactorily. The CH* model predictions could be used for a particular pressure and temperature condition but the model predictions should be scaled with caution for other operating conditions.

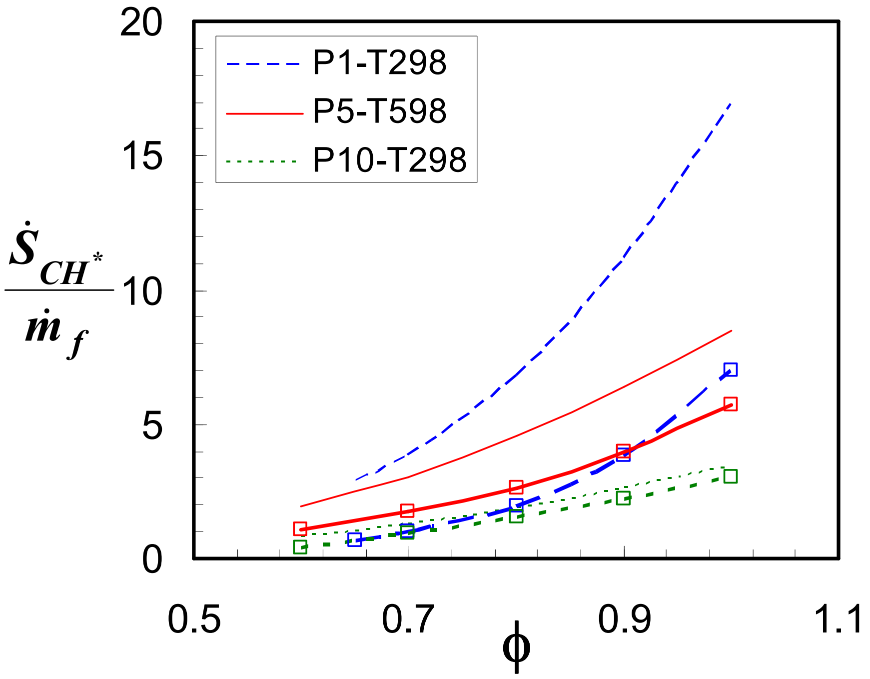

Figure 5.15. CH* model predictions with San Diego (lines) and GRI Mech 3.0 (lines with symbols) reaction mechanisms in methane air flames at various pressure and temperature conditions.

5.1.3 Thermal OH*

Thermal OH* results for the methane experiments are shown in Table 5.2. The relative contribution of thermal OH* to the total OH* signal was calculated as before using Eq. 4. Thermally excited OH* increases exponentially with temperature. So, two equivalence ratios were considered for the analysis: ϕ=0.7 and 1.0. It can be seen that thermal excitation becomes important at high pressure and temperature conditions particularly for near stoichiometric conditions. For example, the thermal pathway can contribute as much as quarter of the total OH* signal at 5atm and 600 K. Of course, these calculations are very simplified based on the assumption that thermal equilibrium exists at every point in the flame.

Table 5.2. Thermal OH* contribution (as percentage of the total OH* signal) in methane experiments.

Methane and Oxidizer	**Operating Conditions**	**% Thermal OH (L_i=10mm)**	
		ϕ = 0.7	**ϕ = 1.0**
CH_4/Air	1 atm, 300 K	<0.1	1
CH_4 (O_2/He)	5 atm, 300 K	1.3	16
CH_4 (O_2/He)	5 atm, 600 K	10	25
CH_4 (O_2/He)	10 atm, 300 K	2.7	25

5.1.4 Thermal CH*

Thermal excitation of CH is also possible, though generally negligible due to the very low concentrations of CH radical in the flame. Thermal CH* is calculated for the experimental methane flames using Eq. 6. The values in Table 5.3 verify this. So, for all practical purposes the contribution from thermally excited CH in the experimentally investigated flames is negligible.

Table 5.3. Thermal CH* contribution (as percentage of the total CH* signal) in methane experiments.

Methane and Oxidizer	Operating Conditions	% Thermal CH (L_i=10mm)	
		$\phi = 0.7$	$\phi = 1.0$
CH_4/Air	1 atm, 300 K	0.006	0.054
CH_4 (O_2/He)	5 atm, 300 K	0.001	0.018
CH_4 (O_2/He)	5 atm, 600 K	0.004	0.034
CH_4 (O_2/He)	10 atm, 300 K	0.001	0.025

5.1.5 Self-Absorption

Estimates of self-absorption are calculated for all the methane flames that were experimentally investigated. Self-absorption was computed in the same manner described in Chapters 2 and 4. While it was estimated to be at most a ~10-15% effect in the high pressure syngas flames, it can be seen in thus absorption changes with flame location. For example, there is difference in self absorption from the side facing the detector and from the rear of the flame, as the path lengths and spatial distribution of the OH* radicals are different. However, this computation gives order of magnitude estimates that can be compared across different conditions.

Table 5.4 that OH* self absorption is more significant in the high pressure methane flames, especially near stoichiometric conditions. It can also be observed that the reduction in OH* signal by absorption increases with the integration length (residence time). Moreover, it can be seen that absorption is a function of pressure, temperature and equivalence ratio. This has immediate implications for the scaling constant (C_{OH*}). According to the results in the table, the scaling constant can change as much as 2 times across the equivalence ratio range. However, this change was not observed in the experiments. It should be noted that this calculation is a worse case estimate, as it uses a peak absorption coefficient. Also the actual flame is axisymmetric rather than 1-d, and thus absorption changes with flame location. For example, there is difference in self absorption from the side facing the detector and from the rear of the flame, as the path lengths and spatial distribution of the OH* radicals are different. However, this computation gives order of magnitude estimates that can be compared across different conditions.

Table 5.4. Fraction of OH* signal absorbed in methane experiments.

Methane and Oxidizer	Operating Conditions	% Absorption (L_i=10 mm)		% Absorption (L_i=5mm)	
		$\phi = 1.0$	$\phi = 0.7$	$\phi = 1.0$	$\phi = 0.7$
CH_4/Air	1 atm, 300 K	5	3	5	2
CH_4 (O_2/He)	5 atm, 300 K	30	13	20	8
CH_4 (O_2/He)	5 atm, 600 K	41	31	21	14
CH_4 (O_2/He)	10 atm, 300 K	39	20	24	9

5.2 Jet-A Validation

5.2.1 Atmospheric Pressure

Jet-A is a primary fuel in aeropropulsion applications, and as a light oil fuel is relevant in many other combustion applications. In spite of its importance, there have been very few studies that investigated flame chemiluminescence applications in Jet-A systems. The preliminary results presented in this thesis represents an effort to validate CH* and OH* chemiluminescence mechanisms in this complex fuel.

5.2.1.1 CO_2* Chemiluminescence

Jet-A is a complex, multi-component heavy hydrocarbon fuel that has a widely varying composition. The apparent underlying "blue continuum" observed in H_2-CO flame spectra in the wavelength range 200-700 nm is primarily due to CO_2* chemiluminescence while there are claims of contribution from other sources such as H_2O_2, H_2O etc. though negligibly. However, in the combustion of complex hydrocarbon fuel such as Jet-A, there may be other sources (such as HCO) which might corrupt this "*CO_2* background*" and the model for CO_2* chemiluminescence would no longer be valid.

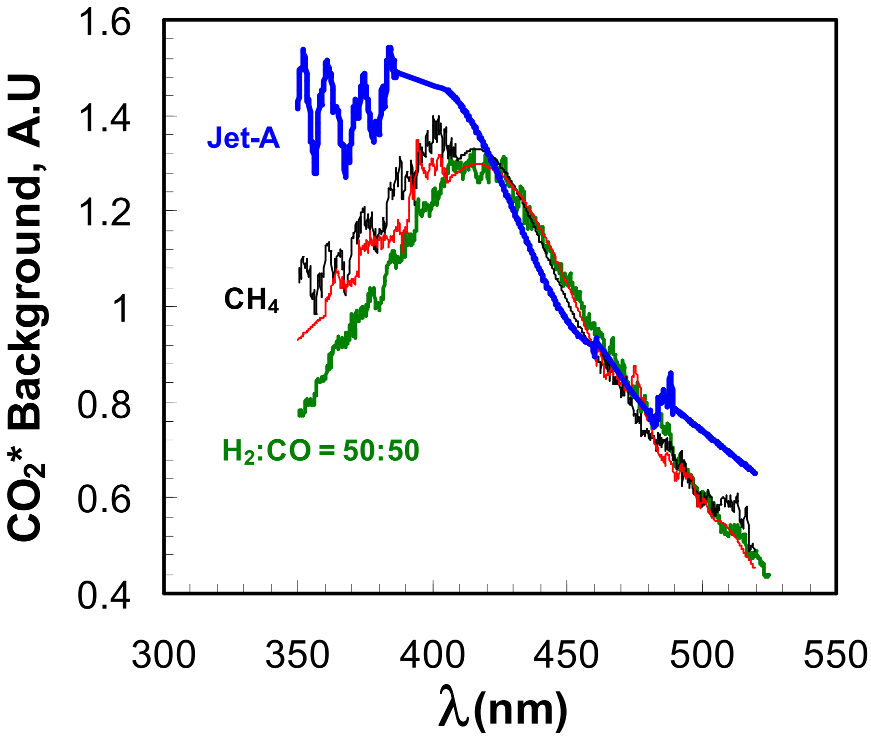

Figure 5.16. Nominal "CO_2* background" spectral shape in typical premixed flames of syngas mixtures, methane and Jet-A fuels at atmospheric pressure conditions.

To appreciate this issue, the spectral shape of the "*CO_2* background*" in a typical syngas mixture (H_2:CO=50:50), methane and Jet-A flame are compared in Figure 5.16.

The CO_2* spectral profiles correspond to an equivalence ratio of 0.7. The CH* and C_2*bandheads are removed from the spectra wherever necessary and their corresponding backgrounds are fitted with cubic polynomials and shown in Figure 5.16. It can be clearly seen that the CO_2* spectral shape in Jet-A flames is very different from that of either syngas or methane flames. In fact, clear large peaks can be seen in the ultraviolet-blue region of the Jet-A flame spectrum, indicating that there may be other emitters in Jet-A flames that might cause this huge difference in the spectral shape. Hence, CO_2* chemiluminescence at 375 nm is not investigated further for Jet-A flames.

5.2.1.2 OH* and CH* Chemiluminescence

Flame chemiluminescence was acquired in laminar premixed prevaporized Jet-A flames at atmospheric pressure and 450 K reactant preheat conditions. Two mechanisms each for OH* and CH* chemiluminescence are considered. For OH*, the two mechanisms in Table 5.1 are used, while for CH*, the Carl and Peeters mechanisms are considered. As before, we consider the variation of normalized OH* and CH* chemiluminescence signals with equivalence ratio to assess the accuracy of the models in

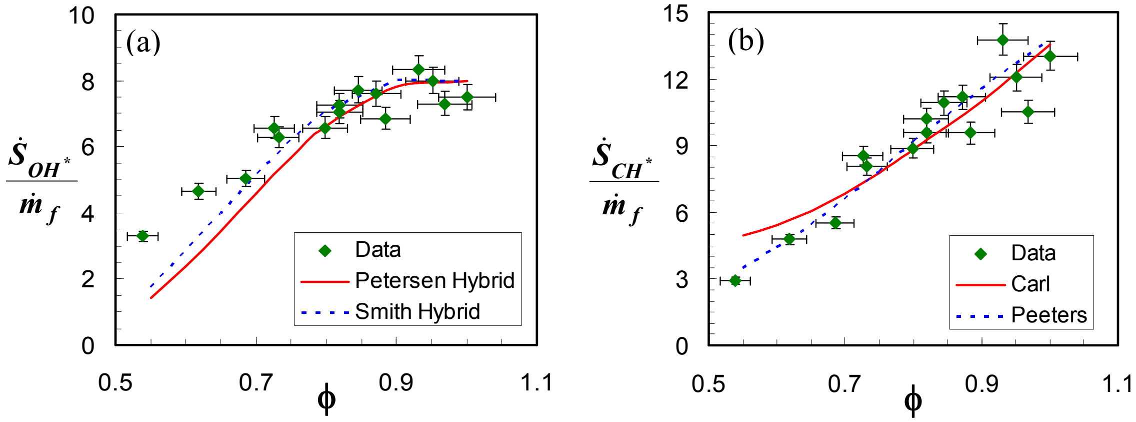

Figure 5.17. Comparison between measured and simulated normalized chemiluminescence for a) OH* emission and b) CH* emission in Jet-A flames.

Jet-A flames. Results for normalized OH* and CH* emission signals are given in Figure 5.17, and they are compared with simulations using Eq. 19 and Eq. 21.

It can be seen in Figure 5.17a that the OH* chemiluminescence model predictions show significant deviation in the leaner equivalence ratio regime. However, the Smith hybrid performs marginally better than the Petersen hybrid in this region. So, the OH* mechanisms should be used with caution for predictions in lean equivalence ratios but they can give excellent estimates for the near stoichiometric mixtures. The discrepancy found in the lean equivalence ratios could be due to the inaccurate estimates of the OH* precursors (such as O, H, CH and O_2) by the Jet-A reduced mechanism itself. It is also possible that there is another OH* formation mechanism that is not accounted in the present analysis. Finally, lack of information about the collisional quenchers in this flame and their quenching rates could be the cause.

The CH* chemiluminescence results are shown in Figure 5.17b; both the Peeters and Carl mechanisms produce very good agreement with the experimental data, as in the methane validations. The two mechanisms provide essentially identical results, except below ϕ~0.7, where the Peeters mechanism appears to provide a better match. However, the difference between the two is not large, and possible errors in the reduced mechanism preclude identifying an optimum mechanism. However, it is interesting to note that the simulations indicate that for near stoichiometric conditions, R2 and R3 contribute almost equally to the CH* signal in the Carl mechanism, while R2 dominates R3 for the Peeters mechanism. In spite of these differences, it is remarkable to find excellent agreement between the two. In summary, preliminary experimental results indicate that the CH* chemiluminescence can be predicted with models employing formation reactions R6 and

R7, as in methane flames. Furthermore, it is interesting to note that despite the significant variation in k_2/k_3 for the two mechanisms, they again provide similar results at atmospheric pressure. However, more experiments have to be performed at various pressure and preheat conditions to test the robustness of the Jet-A combustion mechanism as well as the OH* and CH* chemiluminescence mechanisms.

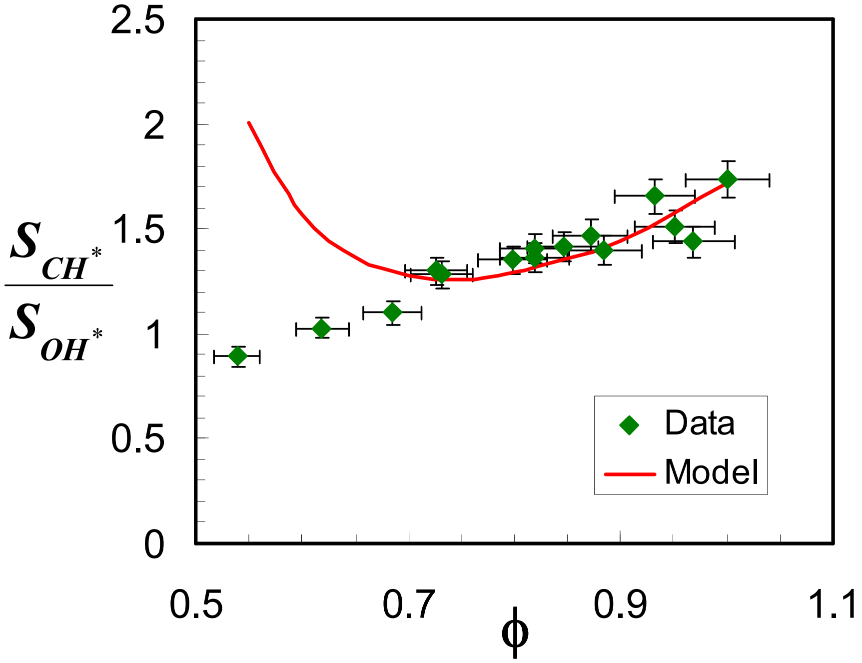

Figure 5.18. CH*/OH* chemiluminescence intensity ratio variation with equivalence ratio in a premixed, prevaporized and preheated (450K) Jet-A flame at 1 atm.

The CH*/OH* chemiluminescence signal ratios are considered next for the sake of completeness. The measured chemiluminescence signal ratio is related to the simulated ratio through the expression given in Eq. 21. OH* chemiluminescence is modeled with the Smith hybrid mechanism, and CH* chemiluminescence is modeled with the Peeters mechanism. The experimental and simulated CH*/OH* ratios are shown in Figure 5.18. It can be noticed that the simulations produce good agreement at the near stoichiometric conditions but start deviating from the experimental data in the leaner equivalence ratios.

This can be explained based on the results in Figure 5.17. OH* is significantly underestimated in the lean regime while CH* is predicted excellently throughout the equivalence ratio range. Hence, the steep increase found in the simulated ratios in the leaner equivalence ratios.

In summary, mechanisms for OH*, CO_2* and CH* chemiluminescence have been validated in two hydrocarbon fuels. The CO_2* global mechanism validated in the syngas tests provides an excellent match to the atmospheric methane data. However, in high pressure methane flames and Jet-A flames there is significant interference from other emission sources. The validated OH* mechanism adds one more formation step (R3) to the mechanism validated in Chapter 4. The temperature dependence given in [45] for k_3 provided the best results. In addition, the ratio k_1/k_3 was estimated by comparing the syngas and methane atmospheric data. As the literature shows a reasonable agreement on the magnitude for k_1, this ratio was used to provide an improved estimate for the pre-exponential factor (i.e., the *A* coefficient) for k_3. The validated OH* mechanism captures the ϕ and pressure dependence well, but failed to capture the reactant preheat effect at high pressure. A mechanism for CH* was also validated, though two sets of rate constants (Carl and Peeters) were able to predict the methane and Jet-A experimental data. The Peeters rate constants produced a better match for the ϕ dependence in the atmospheric flames, while the Carl values provided slightly better ϕ and preheat temperature dependence results at elevated pressure. As in the syngas case, there are possible systematic errors in the high pressure simulations due to inaccuracies in the flame reaction mechanisms employed here. In addition, radiative trapping and thermal OH* production are likely error sources for the high pressure experiments. Excellent agreement between the global chemiluminescence measurements in the laminar and swirl methane flames was observed. The fact that the swirl combustor conditions are likely in the corrugated flamelet or thin reaction zone regimes suggests that the dependence of chemiluminescence on conditions in laminar flames have relevance in a number of turbulent flames.

CHAPTER 6

IMPLICATIONS FOR COMBUSTION SENSING

The goal of this chapter is to examine chemiluminescence using the mechanisms for OH*, CO_2* and CH* validated in the previous chapters. Specifically, the effect of pressure, reactant preheat, aerodynamic strain rate, fuel-air ratio and product recirculation on chemiluminescence signals are examined for lean premixed methane and syngas flames. The fundamental aspects of OH*, CH* and CO_2* chemiluminescence in premixed flames are investigated in the first section. The usefulness of flame chemiluminescence for sensing important combustion parameters, specifically heat release rate and reaction zone equivalence ratio, are examined next. As part of the heat release studies, the CO_2* background is estimated at the OH* and CH* detection wavelengths and its implications are presented. This is followed by a discussion on the relative contributions of thermal and chemical sources to OH* in the final section. While the findings presented in this chapter are based on laminar data and simulations, the agreement between the swirl combustion experiments and the laminar results described in Chapter 5, suggest the findings presented here are likely relevant to many practical turbulent combustors.

6.1 Basic Aspects of Chemiluminescence

In syngas flames, we have seen that excited state OH* is formed via R1 while in methane combustion, both R1 and R3 are active. Similarly CH* is produced in methane flames primarily by reactions R6 and R7. Before proceeding further, we begin by considering the zone where chemiluminescence is produced and the relative branching between the formation reactions for OH* and CH* for varying operating pressure and temperature. Additionally, these issues for CO_2* chemiluminescence are considered, but only in syngas flames.

6.1.1 OH* Chemiluminescence

Methane and a representative syngas mixture with equi-molar fractions of H_2 and CO are considered with air as the oxidizer. The operating conditions correspond to three pressures (1, 5 and 15 atm) and two reactant preheat temperatures (~500 and 700 K). First, spatially integrated OH* emission (I_{OH*}) in syngas flames is considered. An equivalence ratio of 0.8 is considered for the analysis. For each condition, the OH* profile is normalized by the value attained at L_i=5 cm.

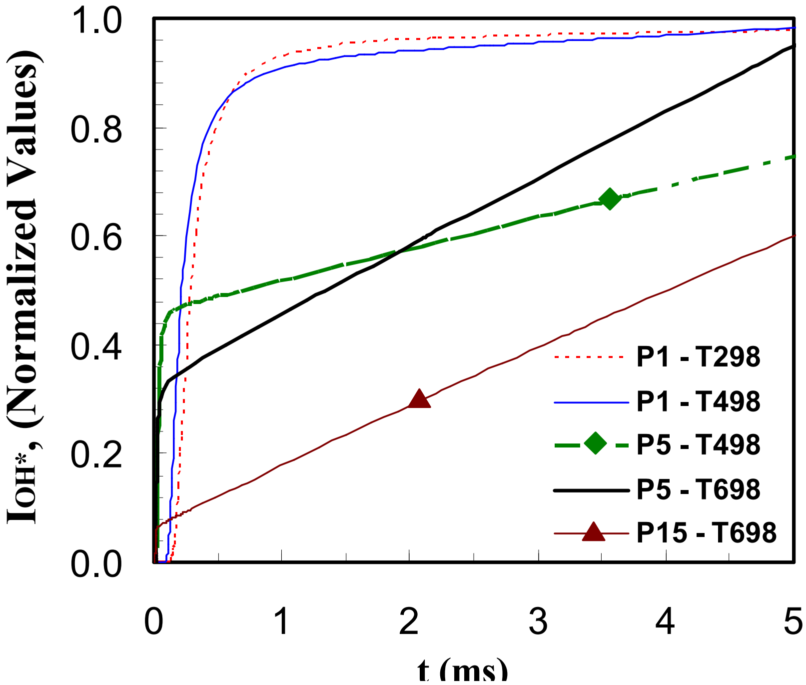

Figure 6.1. Spatially integrated OH* chemiluminescence in syngas (H_2:CO=50:50) flames at various pressure and temperature conditions.

Results for the normalized I_{OH*} plotted against residence time in the combustor is shown in Figure 6.1. It can be seen that the contribution of the exhaust zone to OH* production significantly increases with pressure. In atmospheric systems, most of the OH* is produced in the reaction zone while in high pressure systems this contribution decreases rapidly.

For example, even at 5 atm and 700 K, the reaction zone produces a mere 30 % of the total OH* signal with the remainder coming from the hot exhaust products. So, in high pressure systems, any changes to the exhaust zone environment can drastically effect the OH* signal intensity. For example in many gas turbine engines, cooling/dilution air is added downstream and this could significantly lower the OH* signal for syngas fuels. The OH* signal increases almost linearly in the exhaust zone, as the products of combustion are approaching equilibrium concentrations. In other words, the nearly constant conditions in the exhaust products produce a nearly constant local chemiluminescence rate. The effect of pressure is also seen to dominate the influence of reactant preheat. This may be due to the decrease in reaction zone thickness and radical superequilibrium levels as pressure is increased. Both effects will tend to reduce the relative amount of OH* chemiluminescence from the primary heat release zone. Residence time of the product gases in the combustor is another important factor that effects the OH* signal output. For example, at 15 atm and 700 K, an increase in residence time from 1 ms to 3 ms increases the OH* signal by 20 %.

A similar, but less pronounced effect is seen in methane flames. Figure 6.2 shows that most of the OH* signal is produced in the reaction zone at lower pressures (1-5 atm), while at higher pressures, the contribution from the hot product zone becomes significant.

For example for room temperature reactants at atmospheric pressure, 95% of the OH* signal comes from the primary heat release zone, whereas at 15 atm and 700 K it is only 25%. Product zone emission is due to formation reaction R1, as R3 requires CH, which is not present in significant levels in the exhaust gases, whereas the R1 reactants include O and H, which are general dissociation products of H_2O and O_2. Thus we see that R1 becomes more prominent at high pressures. Moreover, R1 is a three body reaction, which is greatly enhanced by pressure.

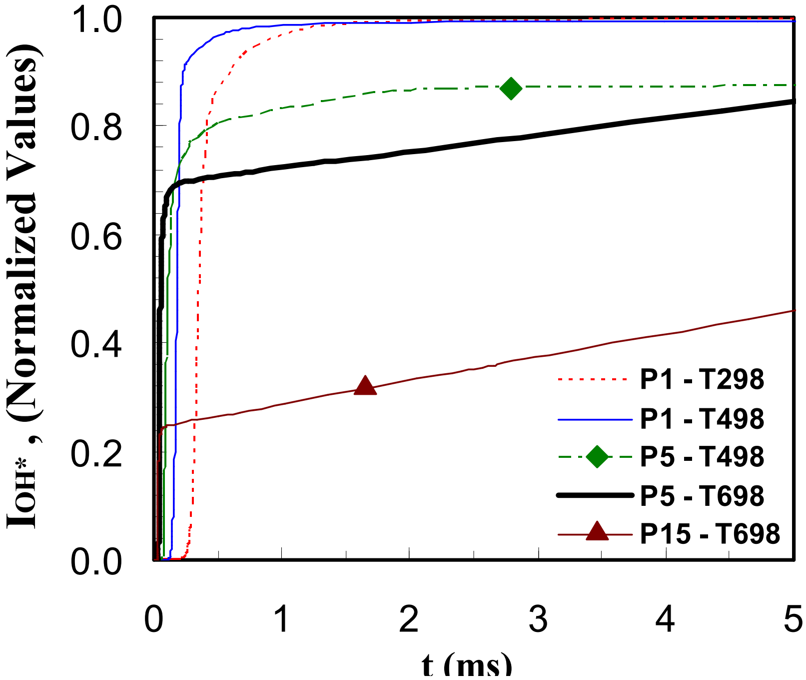

Figure 6.2. Spatially integrated OH* chemiluminescence in methane flames at various pressure and temperature conditions.

These observations are further illustrated in Figure 6.3, which shows the local emission intensity profile for a laminar methane-air flame at 5 atm with reactants at 700 K and ϕ=0.8. While R3 dominates in the thin reaction zone, the contribution of R1 in the potentially wider product/exhaust zone can become more important. To further

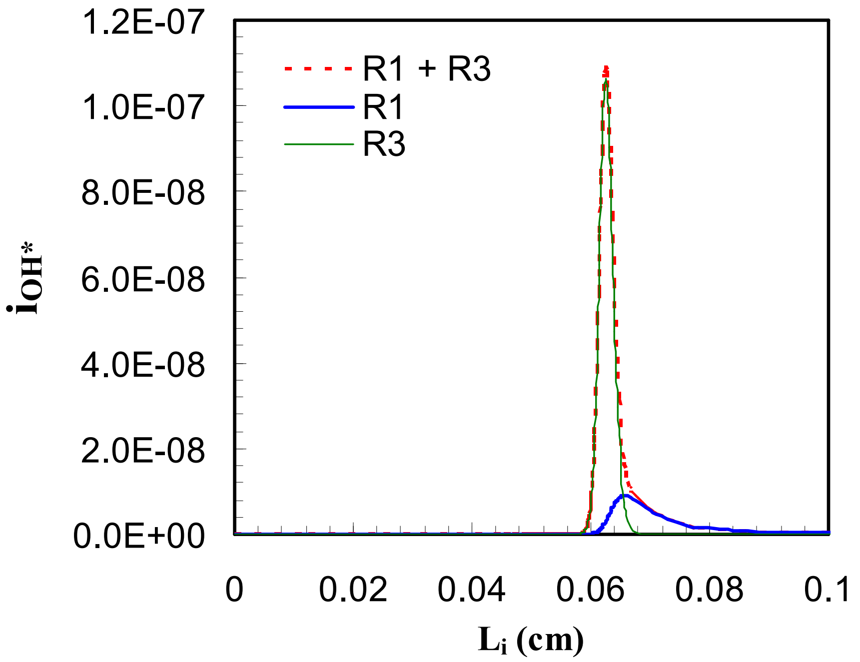

Figure 6.3. Comparison between the volumetric photon emission rate (i_{OH^*}) for OH* produced by R1 and R3, in a methane-air flame at 5 atm, 700 K (ϕ=0.8).

investigate the OH* branching, i.e., the relative contributions of R1 and R3 to the total OH* signal, we compare the integrated OH* signal intensity produced by R1 and R3 (Table 6.1).

Table 6.1. Fractional contribution of OH* formation reaction R1 to the total OH* chemiluminescence signal in methane-air flames at different temperature and pressure conditions, based on residence time for an equivalence ratio of 0.8.

Operating Conditions	End of Reaction Zone	t=0.5 ms	t=2 ms	t=5 ms
1 atm, 300 K	17%	5%	17.6%	18%
1atm, 500 K	20%	17%	22%	22.5%
5atm, 500 K	18%	19.3%	20.3%	22%
5atm, 700 K	21%	26%	29%	37%
15atm, 700 K	22%	28%	43%	57%

As suggested previously, R3 is the dominant OH* production pathway in atmospheric pressure flames, contributing about 80% of the OH* signal. While the analysis is presented for an equivalence ratio of 0.8, the results are similar for other lean stoichiometries as well. In addition, R1 never dominates the methane primary heat release zone; its contribution is approximately 20% of the total OH* chemiluminescence by the end of the reaction zone for all the operating conditions studied here. Thus under most conditions, OH* is mainly produced via R3 in the primary heat release zone. The overall contribution of R1 increases with residence time of the combustor, as expected. However, the increase is most rapid in the 15 atm, 700 K flame, with the R1 contribution reaching almost 60% at a residence time of 5ms. Though not shown here, R1 contributes ~80% of the OH* signal for near stoichimetric flames at these conditions, but <25% for flames with $\phi<0.7$.

Table 6.2. Peak concentrations of relevant species in OH* formation reactions, in methane-air flames at different pressure and temperature conditions. The equivalence ratio is 0.8 and the concentration units are mol/cm^3.

Operating Conditions	[H]	[O]	[O_2]	[CH]
1 atm, 300 K	1.9×10^{-8}	2.0×10^{-8}	7.9×10^{-6}	5.5×10^{-12}
1atm, 500 K	2.8×10^{-8}	2.9×10^{-8}	4.7×10^{-6}	1.2×10^{-11}
5atm, 500 K	3.4×10^{-8}	4.8×10^{-8}	2.4×10^{-5}	1.6×10^{-11}
5atm, 700 K	5.6×10^{-8}	7.6×10^{-8}	1.7×10^{-5}	3.9×10^{-11}
15atm, 700 K	5.9×10^{-8}	9.0×10^{-8}	5.1×10^{-5}	4.1×10^{-11}

High pressure and high preheat temperature have competing effects on the R1 formation rate, with higher temperatures favoring dissociation (O and H), whereas high pressure discourages dissociation, though enhancing the third body concentration in R1. If the peak concentrations for the above species are considered, as in Table 6.2, it can be seen that an increase in preheat by 200 K, increases the peak [O] and [H] by ~50% and doubles the peak [CH]. However, an increase in preheat decreases the peak [O_2] due to dissociation. Increasing pressure at constant preheat does not appreciably increase the peak concentrations of the radical species [O], [H] and [CH], while the peak [O_2] and [M] increase proportionally.

In summary for high pressure and high temperature reactants, the contribution of the exhaust zone to the total OH* signal via reaction R1 is significant, in both methane and syngas flames. This effect is more prominent in near stoichiometric flames. In methane-air flames, R3 is dominant in the flame reaction zone but becomes insignificant in the exhaust zone. Thus, the total OH* signal captured can become dependent on the residence time of the hot product region in the combustor.

6.1.2 CH* Chemiluminescence

As CH* is not produced in syngas combustion, only methane-air flames are considered in this section. Both CH* formation reactions, R6 and R7, contain C_2H as one of the reactants, which is a fuel radical and therefore exists only in the primary reaction zone for lean hydrocarbon flames. As a consequence, CH* is confined to the primary zone as can be seen in Figure 6.4, which is based on the kinetic parameters from the Carl mechanism. The two formation steps are nearly coincident within the primary heat release zone, though the CH* produced by R6 peaks later than the R7 contribution due to the relative increase in [O] compared to [O_2] there. Because CH* is confined to the primary reaction zone, the total CH* signal should be nearly independent of the residence time within the combustor, unless the residence time is less than that needed for the primary fuel combustion steps to be completed.

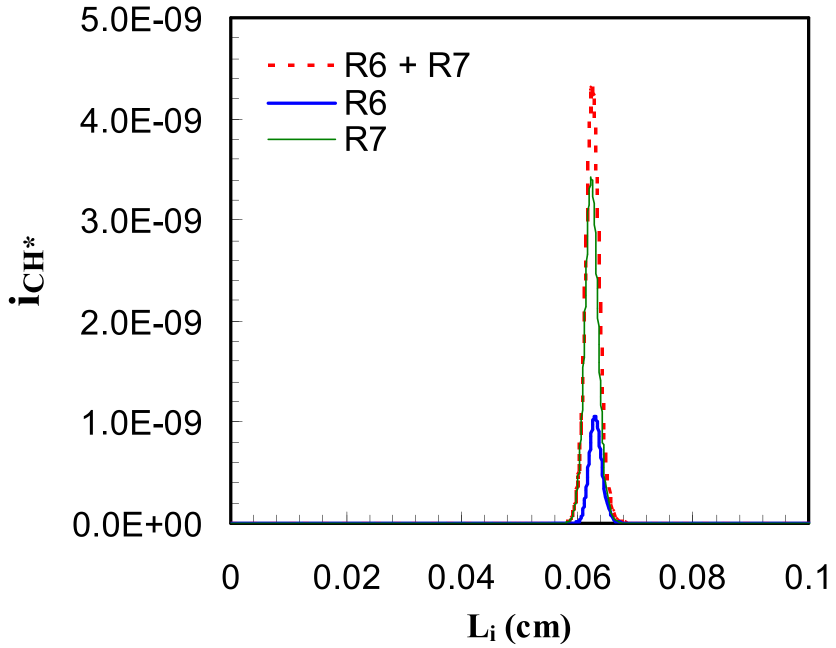

Figure 6.4. Comparison between the volumetric photon emission rate (i_{CH^*}) for CH* produced by R6 and R7, in methane-air flame at 5atm, 700 K (ϕ=0.8).

Next, we consider the relative contributions of R6 and R7 to the total CH* signal at different pressures and temperatures. For this analysis, an arbitrary residence time of 2 ms is used, and the results are presented in Table 6.3. R7 is the dominant CH* production pathway in methane-air flames, and even more so at high pressure and temperature conditions. Pressure has a stronger effect than temperature on the branching ratio between the reactions. The reason lies in the manner by which pressure and temperature influence the O and O_2 concentrations. High pressures tend to lower the $[O]/[O_2]$ ratio, thus decreasing the contribution from R6. Similarly, higher temperatures increase the ratio and the R6 formation step. Thus it should be expected that the contribution from R6 would further decrease at higher pressures and for very lean (low temperature) conditions.

Table 6.3. Fractional contribution of CH* formation reaction R6 to the total CH* chemiluminescence signal in methane-air flames at different temperature and pressure conditions (ϕ=0.8).

Operating Conditions	t=2 ms
1 atm, 300 K	37%
1atm, 500 K	40%
5atm, 500 K	19%
5atm, 700 K	22%
15atm, 700 K	11%

6.1.3 CO_2* Chemiluminescence

CO_2* chemiluminescence occurs in syngas as well as methane flames. However, as the photon emission rate given by the current CO_2* mechanism is based on experimental data from syngas systems, and also due to the observed discrepancies in methane flames (Chapter 5), CO_2* chemiluminescence is investigated here only for syngas flames, with a nominal H_2:CO=50:50 mixture analyzed. As CO_2* is formed from CO and O, it can be expected to be produced in the product gases as well as the primary reaction zone. Normalized and spatially integrated CO_2* chemiluminescence profiles are shown versus residence time in Figure 6.5.[*] Most of the CO_2* is produced in the reaction zone at atmospheric pressure.

---

[*] For each condition, the CO_2* profile is normalized by the spatially integrated value attained at the residence time corresponding to 5 cm beyond the beginning of the reaction zone.

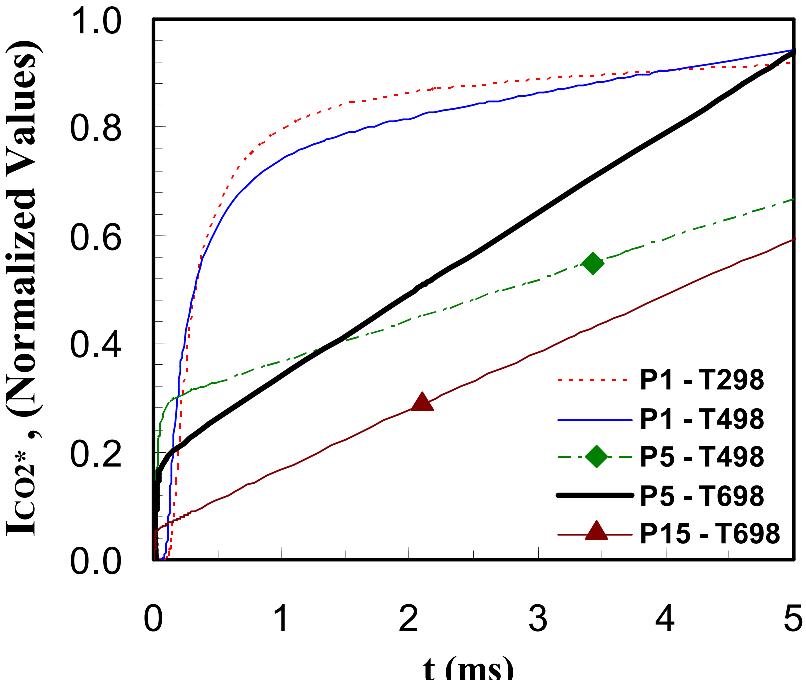

Figure 6.5. Normalized spatially integrated CO_2* chemiluminescence in H_2:CO=50:50 syngas mixture at various pressure and temperature conditions (ϕ=0.8).

However, as the pressure is increased, more and more of the CO_2* is produced in the hot product region. For example, at 5 atm and 500 K preheat, almost 70% of the CO_2* signal is produced downstream of the primary heat release zone. Thus at high pressures, the CO_2* chemiluminescence signal will depend considerably on the residence time of the hot product zone in a combustor. For example, for the 5atm and 700 K case, the CO_2* signal increases by ~32% between 1 and 3 ms, whereas it increases by a mere 8% for the atmospheric pressure and room temperature reactant flame. Thus if the conditions of the exhaust zone are modified (e.g., by introduction of dilution air or radiant heat losses), the CO_2* chemiluminescence signal can be drastically affected.

6.2 Combustion Sensing Applications

Flame chemiluminescence is used for various diagnostic purposed in combustion, for example for sensing fuel-air ratio and as a measure of heat release rate. These sensing applications are explored here using the developed chemiluminescence models, with special attention given to the impact of varying operating conditions, specifically pressure, reactant preheat, strain rate and exhaust gas recirculation (EGR).

6.2.1 Heat Release Sensing

To examine heat release sensing, it is convenient to normalize the emission intensities with the heat release rate per unit flame area, q (W cm^{-2}), which is given for the simulations by

$$q = \int_0^L q' dx \tag{22}$$

where q' (W cm^{-3}) is the volumetric heat release rate at a point in the flame and L again is the integration length. Here, L is chosen such that it corresponds to a post-flame residence time of 2.5 ms, which is characteristic of many practical combustors. For sensing heat release rate, one would ideally like this normalized chemiluminescence signal (I_C/q) to be a constant, i.e., only a weak function of other flame conditions, such as equivalence ratio, pressure and preheat temperature. In the following, the calculated normalized chemiluminescence emission intensities were scaled by a single constant to make their values convenient for plotting. Experimental results for chemiluminescence signals normalized with fuel mass flow rate (I_C/m_f) are also used for interpreting the modeling results, wherever necessary. It should be noted that in lean flames, q is proportional to mass flow rate of the fuel.

6.2.1.1 Syngas

A representative H_2:CO=50:50 syngas mixture is considered for this study, and normalized OH* (I_{OH*}/q) and CO_2* (I_{CO_2*}/q) chemiluminescence signals are analyzed.

6.2.1.1.1 Effect of Pressure and Temperature

Results for normalized OH* chemiluminescence signals are shown in Figure 6.6a as a function of equivalence ratio (limited to lean operation) for different pressures and preheat conditions, with the range representative of gas turbine conditions. It is clear that the normalized OH* signal is a strong function of equivalence ratio, with as much as a five times increase from ϕ=0.5 to 1 at lower pressures and almost a factor of 70 increase at 15 atm. At higher pressures with preheat, the equivalence ratio dependence changes abruptly at ϕ~0.7. The reason for this rapid increase is due to the rapid increase in the formation rate as compared to the quenching rate of the excited species. The quenching rate does not significantly change across the equivalence ratio considered while the formation rate increases many fold in this range. However, the flame thickness also decreases with equivalence ratio, which affects the integrated chemilumincescence intensity (I_c). Therefore, it is the complex interplay between flame thickness, OH* formation and OH* quenching that decides the magnitude of the signal.

The simulation results also reveal that the normalized OH* chemiluminescence generally decreases with pressure for lean mixtures, except at near stoichiometric conditions. At this point, the general decrease in signal from the primary heat release region is starting to be offset by the effect of emission from the product gases for the 2 ms integration time chosen. The effect of preheat on the normalized OH* signal is more uniform in that it causes an overall increase in the OH* signal throughout the equivalence ratio range. Thus we find that the relative amount of OH* chemiluminescence per unit heat release is greatly enhanced at high temperatures. The above results comparing values across different pressures and preheat temperatures should be interpreted cautiously, as the models may not be accurate in such comparisons. Still, the general trends should hold.

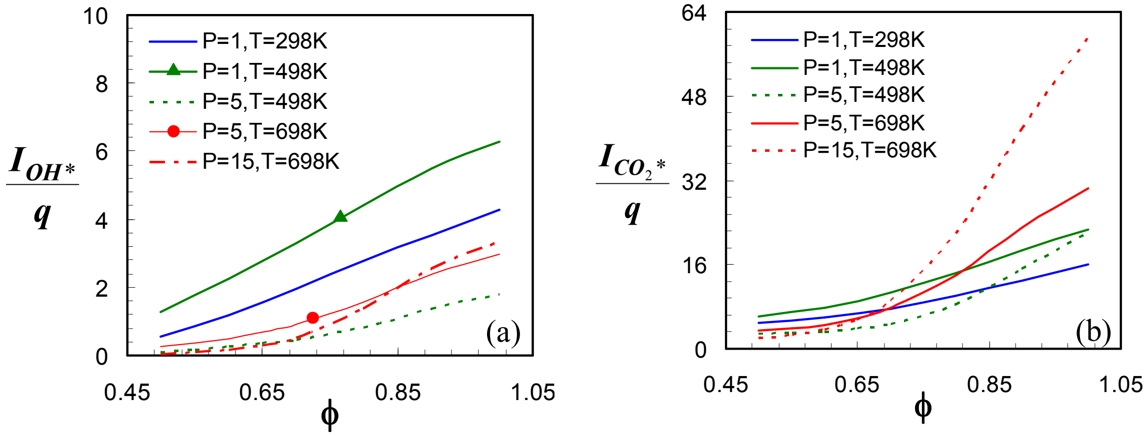

Figure 6.6. Variation of (a) OH*, (b) CO_2* chemiluminescence with equivalence ratio at various pressure and preheat conditions.

The normalized CO_2* signal, Figure 6.6(b), also depends strongly on equivalence ratio but usually to a lesser degree compared to OH* chemiluminescence. It increases across the ϕ=0.5-1 range by about 3.5 times at atmospheric pressure and by ~30 times at 15 atm. However, most of this change occurs for ϕ>0.7 for all the pressure and temperatures considered. Thus for very lean syngas mixtures, CO_2* chemiluminescence has some advantage for heat release rate sensing compared to OH* chemiluminescence, as minor variations in equivalence ratio and preheat temperature would cause smaller changes in the chemiluminescence signal. For example, a ±5% variation of equivalence ratio at ϕ=0.6 at 15 atm and 700 K, would produce a ±18% change in the CO_2* signal per unit heat release. The same change would produce nearly twice the change (± 30%) in the OH* signal per unit heat release. The rapid increase in I_{CO2*}/q for higher equivalence ratios is attributed to the rapid increase in the formation rate of CO_2* caused by the rapid rise in temperature and [O]. It also results from significant amounts of CO_2* produced downstream of the primary reaction zone in the hot products (again when temperature and [O] are high). This would be even more important in combustors with longer residence times, as observed earlier (Figure 6.5). In syngas flames as noted previously, this also occurs for OH*. However, the contribution from the post-flame zone is not as significant as for CO_2*.

The pressure dependence of the normalized CO_2* signal is also different. Only at very lean equivalence ratios does the normalized CO_2* signal consistently decrease with pressure as observed for OH*. Otherwise there appears to be a non-monotonic pressure effect; an increase in pressure from 1-5 atm reduces I_{CO2*}/q, while a further increase to 15 atm produces a significant rise in the normalized signal. At a given pressure, however, the CO_2* signal per unit heat release responds like the OH* signal to a rise in reactant temperature; it increases throughout the equivalence ratio range.

6.2.1.1.2 Effect of Aerodynamic Strain Rate

Aerodynamic strain is an important aspect of turbulent flames, and therefore it is relevant to most practical combustors with high volumetric efficiency. Up to this point in the thesis, only unstrained laminar flames were simulated. Aerodynamic strain modifies the residence times of the various species in the flame front, and impacts the diffusion rates of species and energy. So it is important to gain some understanding on the dependence of chemiluminescence signals on strain rate for interpreting chemiluminescence data in practical devices.

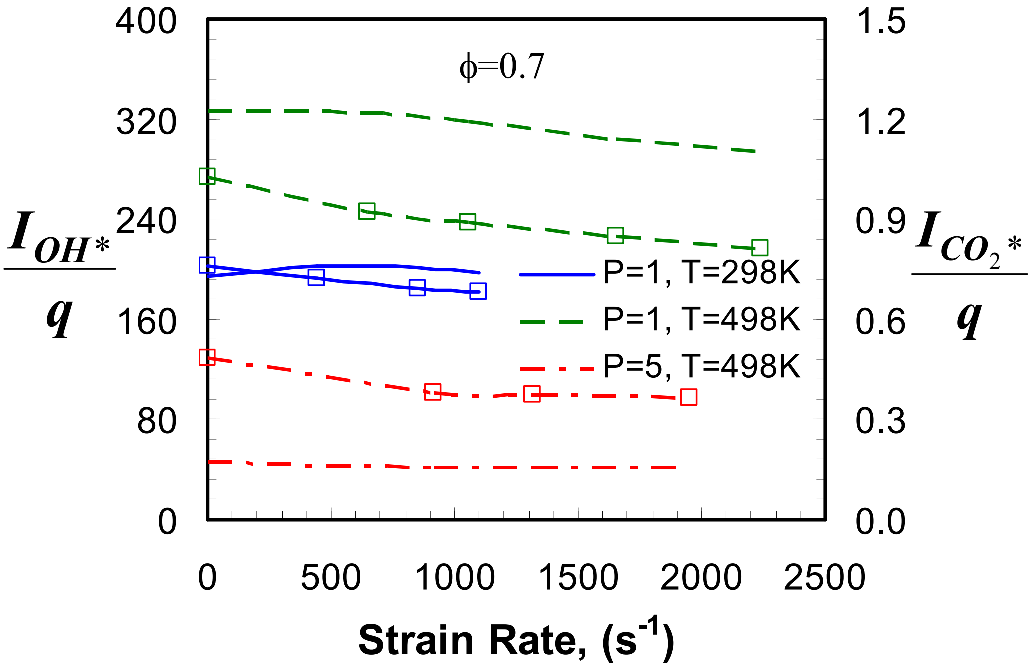

Figure 6.7. Strain rate dependence of OH* (solid lines) and CO_2* (symbols on lines) chemiluminescence in H_2:CO=50:50 syngas mixture.

A framework for numerical modeling of chemiluminescence in opposed flow, laminar, premixed strained flames has been previously demonstrated [10]. That approach is employed here, with the OH* and CO_2* signals again normalized by the heat release rate per unit flame area. However, in this case, the volumetric heat release rate (*q'*) profile is integrated up to the stagnation plane.

Simulation results for OH* and CO_2* chemiluminescence with varying strain rate, at different pressure and preheat conditions, are shown in Figure 6.7. The equivalence ratio of the mixture is fixed at 0.7. The zero strain solution corresponds to that of the one-dimensional laminar premixed flame. The CO_2* signal per unit heat release continuously decreases with strain for the atmospheric pressure cases. However for the higher pressure case, the CO_2* signal is essentially independent of strain, except for an initial drop from the zero strain solution. This drop may be due to the difference in the calculation approaches for the zero strain and strained flames rather than being indicative of a strain effect. Preheating the reactants does not seem to effect the behavior of the normalized CO_2* signal with strain (other than to increase I_{CO2*}/q as noted previously). Since q decreases with strain, the results show that the CO_2* signal decreases faster than q with strain. The normalized OH* signal (included in Figure 6.7) also decreases continuously with strain, except for the room temperature and pressure case. Furthermore, I_{OH*}/q is less sensitive to strain, decreasing by no more than 11% for the conditions examined, whereas I_{CO2*}/q changes by 30% for the same strain rate range.*

Summarizing the findings up to this point, OH* chemiluminescence can be identified as a better heat release marker for turbulent premixed syngas flames at near stoichiometric conditions. It has a lower strain dependence and is less sensitive to equivalence ratio variations for these conditions. For leaner conditions, heat release measurements employing CO_2* may be advantageous, due to the lower dependence on changes in ϕ and preheat temperature, even though the strain dependence is somewhat greater.

6.2.1.1.3 *Effect of Reactant Product Mixing*

The influence of hot products mixing with reactants before combustion occurs is another aspect of practical combustors that needs to be considered. Exhaust gas

---

*Thus the results also suggest that the chemiluminescence ratio I_{CO2*}/I_{OH*} will also decrease with strain.

recirculation (EGR) is a popular strategy for NOx control in many practical combustion devices [79-81]. In addition, reactant-product mixing can also occur as part of the stabilization processes in combustors. For example in gas turbine combustors, swirl stabilization and partial lifting of lip- or dump- stabilized flames can produce zones where product-reactant mixing can occur prior to combustion. Therefore, we examine the effect of product recirculation on flame chemiluminescence. The fraction of product gas in the reactants is commonly quantified by an EGR ratio, specifically the mass ratio of recycled gases to the total mass of the mixture.

Adiabatic product recirculation (denoted *hot EGR* here) was examined for a syngas equivalence ratio of 0.7, and for EGR ratios of 5, 11 and 20%. Note, as the EGR ratio is increased, the inlet temperature of the reactants increases but the final product temperature remains constant since adiabatic product recirculation is simulated. Results are shown for the normalized OH* and CO_2* chemiluminescence in Figure 6.8. Neither I_{OH*}/q nor I_{CO2*}/q is appreciably affected by product recirculation. The normalized OH* signal does increase somewhat with recirculation (by ~10%) for the two atmospheric pressure cases. For example at 11% EGR, I_{OH*}/q increases by about 6% at 298 K and 9% at 500 K compared to the 0% EGR case. The effect at higher pressure is even smaller, I_{OH*}/q is practically constant at 5 atm. The CO_2* signal (I_{CO2*}/q) varies only slightly (a few percent), increasing at 1 atm and decreasing at 5 atm. Reactant preheating does not change this result. In summary, product recirculation does not appear to significantly impact the ability of OH* or CO_2* chemiluminescence to provide measurements of heat release in syngas fuels.* It is interesting to note that for a given operating condition, the temperature at which the OH* profile (i_{OH^*}) peaks, did not change significantly over the EGR ratios considered. The same was observed for the CO_2* profile.

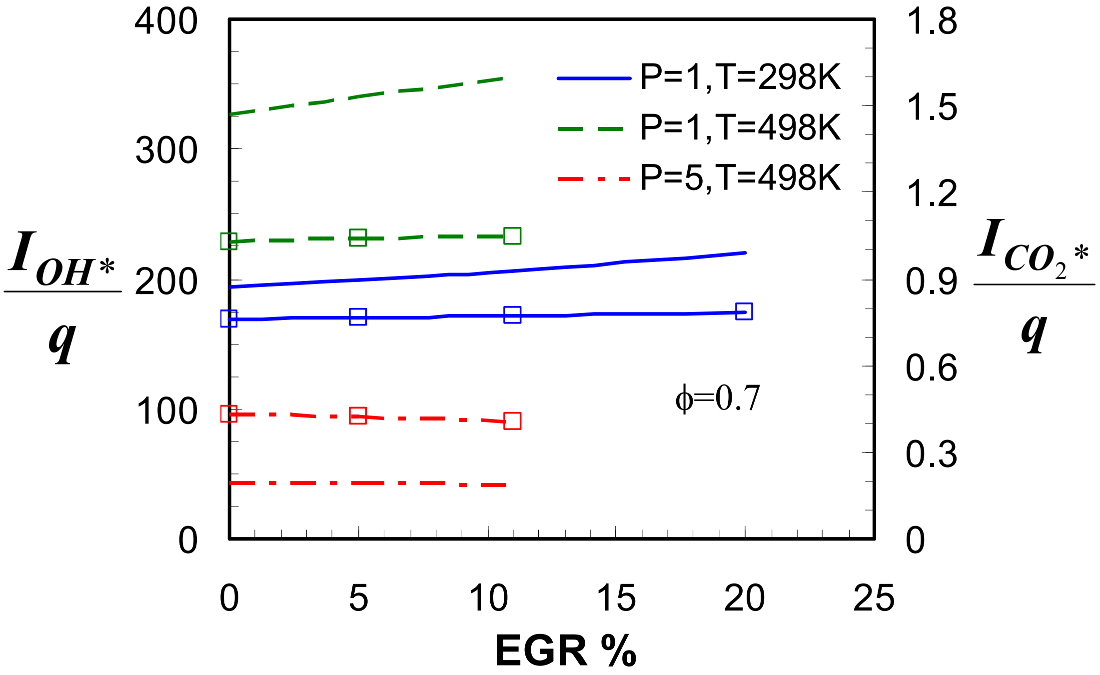

Figure 6.8. Dependence of OH* (solid lines) and CO_2* (symbols on lines) chemiluminescence on product recirculation in a H_2:CO=50:50 (ϕ=0.7) syngas mixture.

6.2.1.2 Methane

While chemiluminescence from OH*, CH* and CO_2* occur in methane-air, the CO_2* signal is more readily corrupted in practical combustors, for example by other broadband sources such as HCO chemiluminescence and blackbody radiation sources, e.g., soot and combustor walls. So, only the normalized OH* (I_{OH^*}/q) and CH* (I_{CH^*}/q) chemiluminescence signals are considered in this analysis.

---

*This also suggests that product recirculation would have little effect on the ratio I_{CO2^*}/ I_{OH^*}..

6.2.1.2.1 Effect of Pressure and Reactant Preheat

Simulation results for OH* chemiluminescence are presented in Figure 6.9, and it can be seen that the normalized OH* signal is a strong function of equivalence ratio, as in the syngas case. I_{OH^*}/q increases by six times at atmospheric pressure for $0.6<\phi<1$. At high pressure (15 atm), the dependence is even greater, with an increase of ~70 times for the same equivalence ratio range.

Pressure in general, decreases the normalized OH* signal over the entire ϕ range. However, this decrease is more pronounced for leaner mixtures. This effect has been observed in an earlier experimental study [19]. At a given equivalence ratio and pressure, preheating also increases the normalized OH* signal, and again the increase is more pronounced for leaner conditions. Overall, the variation with pressure over typical operating conditions is more significant than the preheating effect. However, experimental results in methane-O_2/He flames at elevated pressures only indicate a decrease of OH* signal with pressure consistent with the model predictions but otherwise reveal a negligible effect of reactant preheat as shown in Figure 5.10.

These results can be explained by examining the OH* formation and destruction rates. As shown above, R3 dominates the overall formation in low pressure environments, responsible for almost 80% of the OH* signal at atmospheric pressure. As R3 formation occurs in the primary reaction zone and because increasing pressure reduces the flame thickness, the normalized integrated OH* signal associated with R3 decreases with pressure (the actual OH* signal increases, but q increases faster). While it is true that the contribution from R1 in the product gases increases with pressure (representing ~50% of the total OH* production at 15 atm), the limited residence time assumed in this simulation limits its effect. Also, lower temperatures for leaner equivalence ratios reduces mole fractions of the radicals (CH, O and H) necessary for OH* formation.

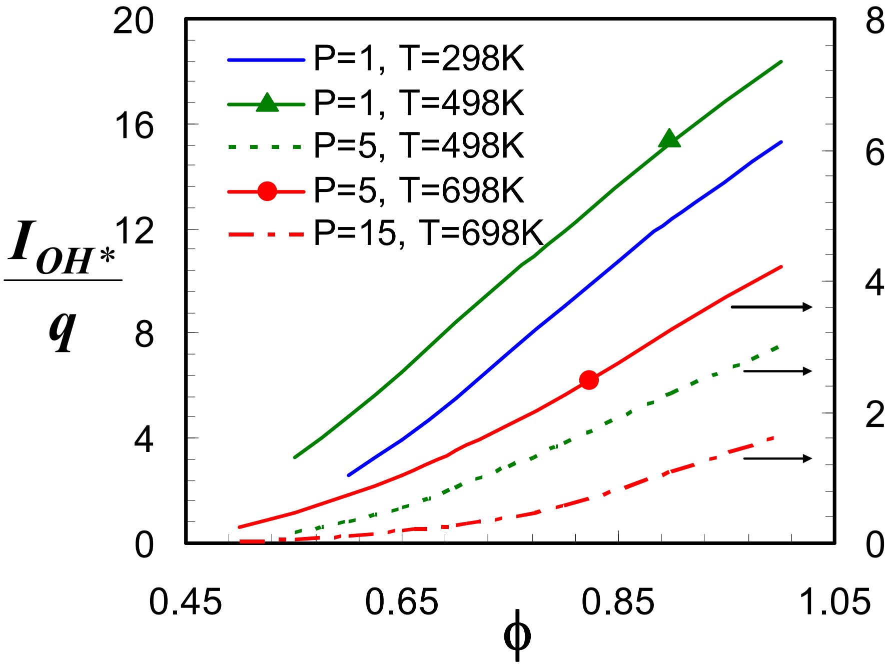

Figure 6.9. OH* chemiluminescence in methane at various pressure and preheat; the high pressure results are scaled to the right axis.

The dependence of OH* chemiluminescence-based heat release sensing of equivalence ratio fluctuations can be determined from Figure 6.9. In general, there is less dependence at near stoichiometric conditions. For example at 15 atm, a ±5% equivalence ratio fluctuation around a mean value of ϕ=0.9 would cause a ±20% change in the sensitivity of chemiluminescence to heat release rate. The same ±5% fluctuation at ϕ=0.55, would cause a larger (±30%) change. Similarly for reactant preheat and pressure fluctuations, the relation between OH* chemiluminescence and heat release shows less variation at near stoichiometric conditions. For example at 5 atm and a 200 K preheat change, I_{OH^*}/q increases by 35% at ϕ=1.0 whereas it increases by twice that (70%) at ϕ=0.7. However, as shown in Figure 5.10, the experiments suggest that at elevated pressures, the effect of reactant preheat may not be significant and any fluctuations in preheat would not change the OH* chemiluminescence signal appreciably.

The results for CH* chemiluminescence are shown in Figure 6.10. The normalized CH* signal increases by as much as 15 times at atmospheric conditions but only by four times at 15 atm for 0.6<ϕ<1. Thus in contrast to OH* chemiluminescence for methane-air flames, the equivalence ratio dependence is reduced for CH* at high pressure. Experimental results for methane-O_2/He flames in Figure 5.13and Figure 5.10 at 10 atm-298 K indicate an increase of ~4 times in CH* signal as compared to ~20 times increase in OH* signal in 0.66<ϕ<1, consistent with the modeling predictions.

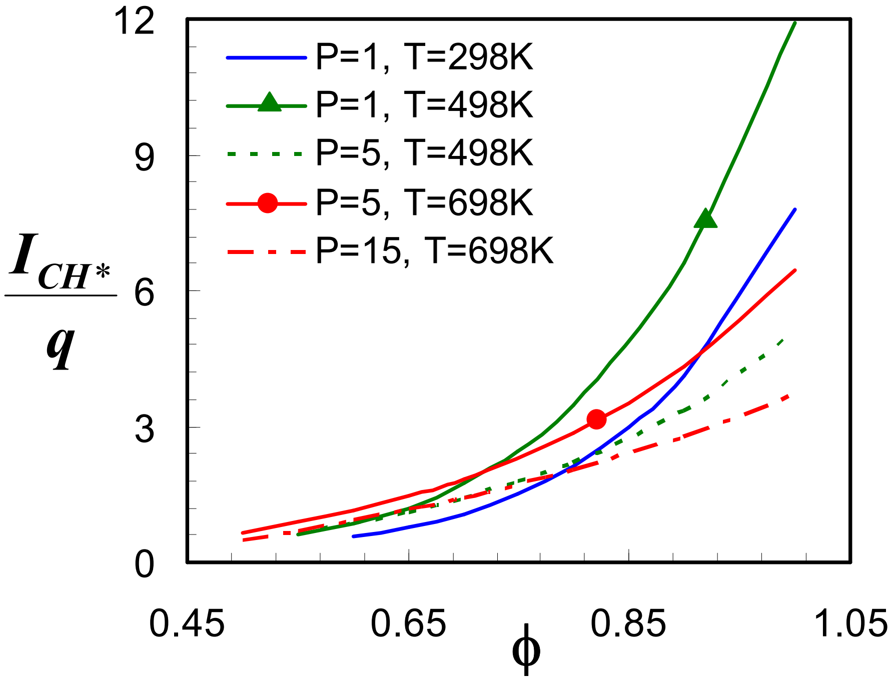

Figure 6.10. CH* chemiluminescence in methane at various pressure and preheat conditions.

Model predictions indicate that reactant preheat produces a uniform increase in I_{CH*}/q throughout the equivalence ratio range, by 1.5 times at atmospheric pressure.

However at 5 atm, a 200 K preheat enhances I_{CH*}/q more for leaner mixtures. Also for a given temperature and equivalence ratio, pressure decreases I_{CH*}/q, with the decrease more pronounced near ϕ=1.0. For example raising the pressure from 5 to 15 atm results in a drop in I_{CH*}/q of 43% at ϕ=1.0, but only 20% at ϕ=0.6. These observations were also verified experimentally in methane-O_2/He flames at elevated pressures. At 5 atm, reactant preheating clearly increased the CH* chemiluminescence signal in Figure 5.14. Similarly, comparing the 5 atm and 10 atm results, it can be seen in Figure 5.14 that the CH* signal decreased by ~4 times, almost uniformly, with increase in pressure. Similar trends were also observed in an earlier experimental effort [30].

To compare CH* to OH* for heat release sensing under unsteady conditions, e.g., combustion instability, we examine the dependence of I_{CH*}/q to fluctuations in equivalence ratio and reactant temperature. For equivalence ratio oscillations at 15 atm, a ±5% change in equivalence ratio produces a ±15% change in I_{CH*}/q. However similar fractional changes in equivalence ratio would produce a ±20% fluctuation at ϕ=0.9 and a ±30% change at ϕ=0.55 in OH* signal at 15 atm. This suggests that CH* is better suited for high pressure applications of heat release sensing compared to OH*. However, the current experimental results in the methane-O_2/He flames show that preheating has a weaker effect on I_{OH*}/q compared to I_{CH*}/q (see Figure 5.10 and Figure 5.13).

6.2.1.2.2 Effect of Aerodynamic Strain

Simulation results for the normalized OH* and CH* signals in an opposed flow (strained) flame are shown in Figure 6.11 for an equivalence ratio of 0.7. I_{CH*}/q is somewhat more dependent on strain at atmospheric conditions than I_{OH*}/q. Reactant pre-

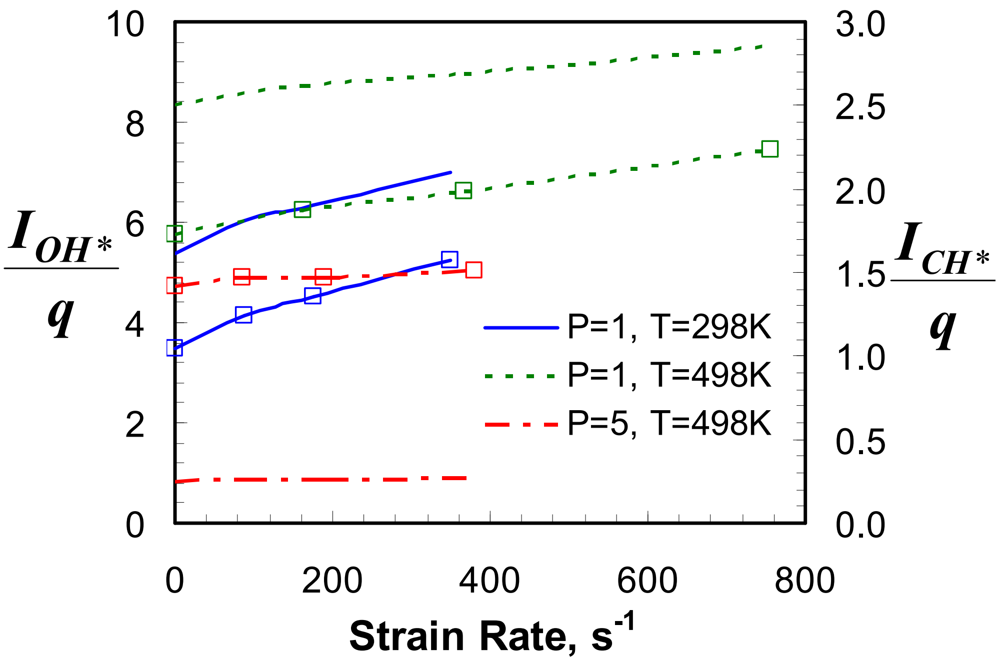

Figure 6.11. Strain rate dependence of OH* (lines) and CH* (lines with symbols) chemiluminescence in methane-air flames at ϕ=0.7.

heating makes both signals less dependent on strain. For the high pressure case, both signals are practically independent of strain. This may be because both preheat and pressure result in thinner flames, which require higher strain rates to influence the reaction zone. Similar trends were observed for calculations with a stoichiometric mixture.

It is interesting to examine the effect of aerodynamic strain rate on the individual production pathways of OH* and CH*. Simulation results for the relative contributions of R1 and R3 to the normalized OH* signal and their dependence with strain rate are shown in Figure 6.12 for an equivalence ratio of 0.7. The OH* production from R1 generally decreases with strain, whereas strain enhances production for the R3 path.

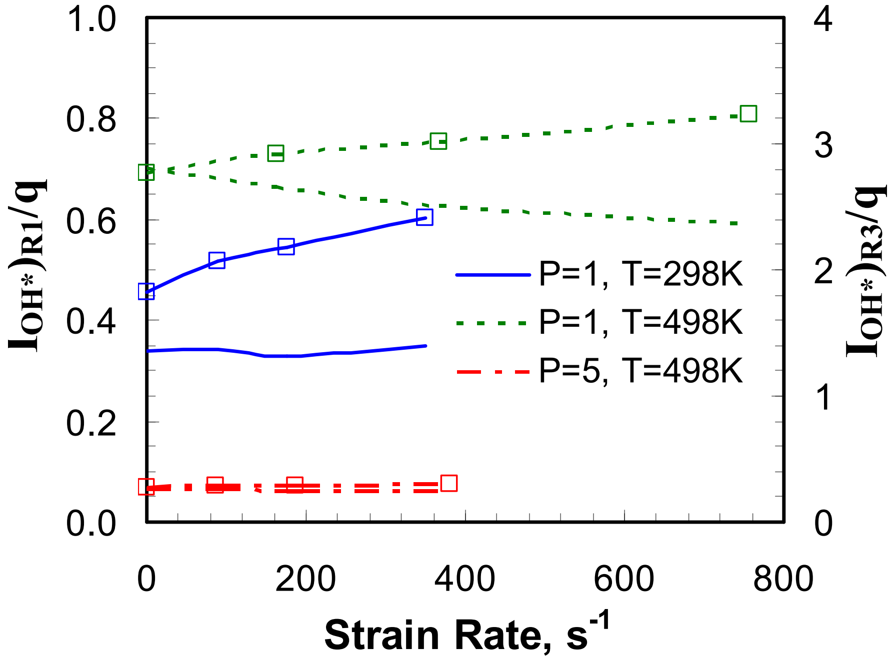

Figure 6.12. Strain rate dependence of OH* chemiluminescence produced via R1 (lines) and R3 (lines with symbols) in methane-air flames (ϕ=0.7).

This is because as strain rate increases, the residence time decreases, and OH* production via R1 being a strong function of residence time results in a reduction of OH* signal, as discussed earlier (Table 6.1). Moreover, this residence time effect is more prominent in near stoichiometric flames. So under stoichiometric conditions, the normalized OH* signal decreases by as much as 50% compared to the unstrained case, even at high pressure. Whereas, in case of R3, q decreases faster than I_{OH*} which causes the increase in the normalized OH* signal. This is because the q' (heat release rate) profile is wider than OH* (i_{OH*}) profile in the flame, and therefore strain effects q' more than i_{OH*}. Similarly results for the strain dependence of reactions R6 and R7 for CH* production are given in Figure 6.13. In this case, I_{CH*}/q produced by either R6 or R7 increases with strain irrespective of the pressure and temperature conditions. CH* is only produced in the reaction zone, which causes the increase in the normalized CH* signal due to reasons similar to those given above.

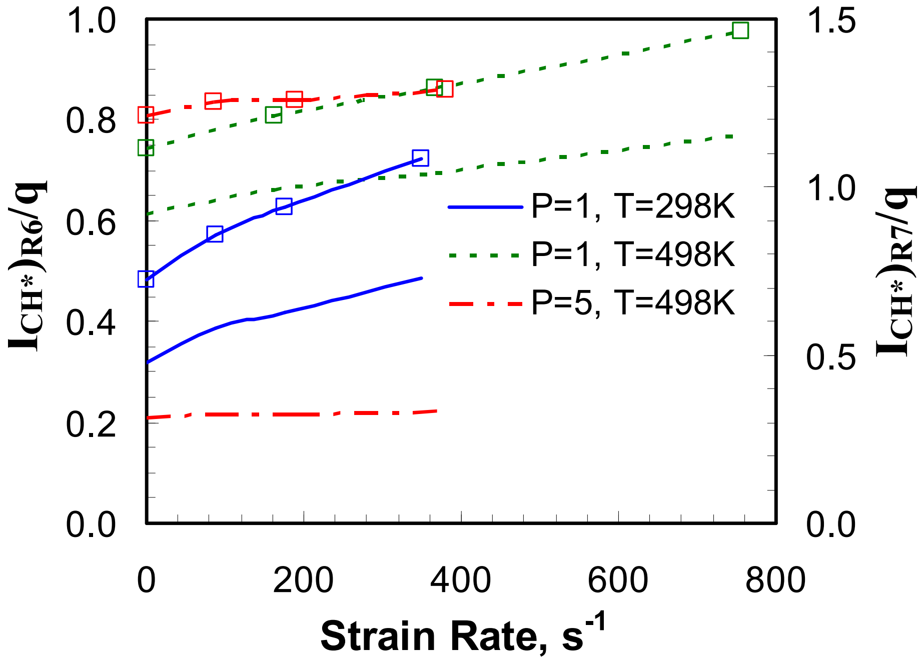

Figure 6.13. Strain rate dependence of CH* chemiluminescence produced via R6 (lines) and R7 (lines with symbols) in methane-air flames (ϕ=0.7).

6.2.1.2.3 Effect of Reactant Product Mixing

Results for OH* and CH* with adiabatic product recirculation are shown in Figure 6.14 at an equivalence ratio of 0.7. As in the syngas case, the normalized OH* signal is practically unaffected by product recirculation at the pressure and preheat conditions studied here. On the other hand, the normalized CH* signal is significantly affected; it increases by as much as 50% for the 20% EGR case. Higher pressures inhibit this increase in CH* signal with EGR. In these cases, q increases only by ~5% in the range of EGR ratios considered. This implies that I_{CH*} increases faster than q. Similar behavior of OH* and CH* signals is also observed in near stoichiometric flames. EGR, unlike aerodynamic strain rate, affects the OH* (R1 and R3) and CH* (R6 and R7) production pathways similarly, increasing both. The contributions from R1 and R3 for OH* increase slightly with EGR, while contributions from R6 and R7 increase as much as 50% for the atmospheric conditions, in the range of EGRs considered.

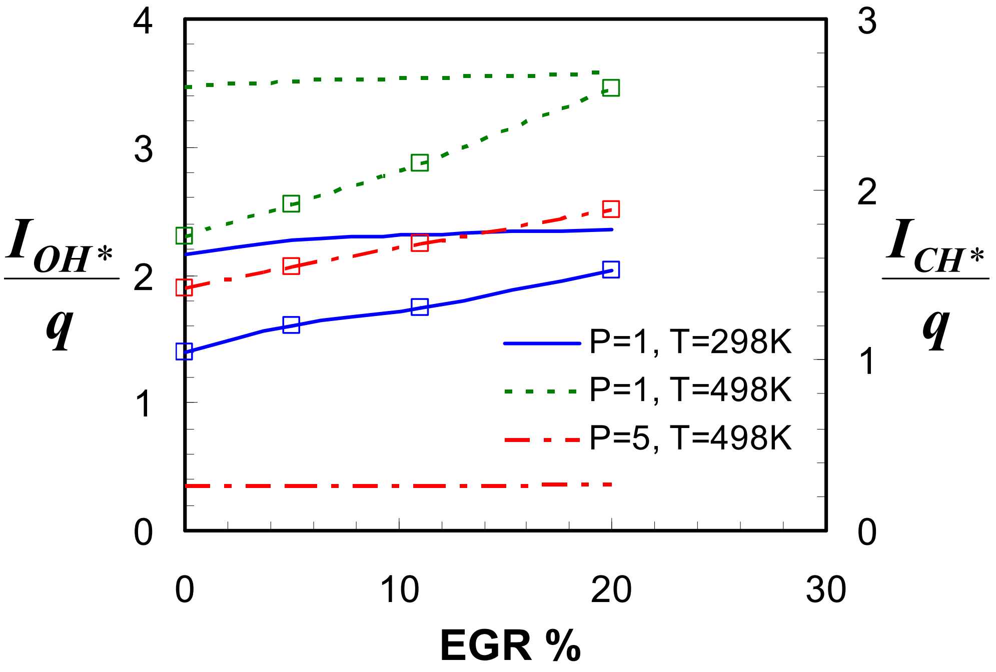

Figure 6.14. Dependence of OH* (solid lines) and CH* (lines with symbols) chemiluminescence on product recirculation in methane-air flames (ϕ=0.7).

Most of the OH* is produced by R3, which has CH as one of its reactants. Both R6 and R7 responsible for production of CH* have C_2H as one of its reactants. However, OH* is weakly affected by EGR while CH* signal increases noticeably. This only proves that EGR favors C_2H more than CH. It can be seen in Table 6.4 that peak [C_2H] increases as much as 42%, while peak [CH] only increases by 6% , at 1atm 500 K, for a 5%-20% increase in EGR.

Table 6.4. Percentage increase in [CH] and [C_2H] peak concentrations for a 5% to 20% increase in EGR for an equivalence ratio of 0.7. Concetration units in mol/cm^3.

Operating Conditions	[CH]	[C_2H]
1 atm, 300 K	9.6%	35%
1atm, 500 K	6%	42%
5atm, 500 K	5%	23%

6.2.2 Equivalence Ratio Sensing

As previously noted, experiments reported in the literature for some hydrocarbon flames at certain conditions showed the variation of chemiluminescence intensity ratios, such as CH*/OH* or C_2/OH*, with equivalence ratio be promising for equivalence ratio sensing. For this sensing application, it would be preferable that this variation be monotonic with a good sensitivity (steep slope) for greater reliability and accuracy. The variation of chemiluminescence intensity ratios in methane and a H_2:CO=50:50 syngas mixture are studied over a range of operating conditions. Experimental results are used to interpret the modeling results wherever applicable.

6.2.2.1 Syngas

In syngas flames, CO_2*/OH* ratio is the only ratio that can be measured. The computed emission ratios for the syngas mixture considered (H_2:CO=50:50) were scaled with to match the validation data at atmospheric conditions (Chapter 4). For syngas-air flames at atmospheric conditions, this scaling constant (C_{det}) had a value of 20. However, for syngas flames with O_2/He as the oxidizer, at elevated pressure and temperature conditions, this scaling constant was found to be ~32. This suggests that the models either under predict CO_2* or over predict OH* in such conditions. So, the models can only be used to qualitatively interpret the behavior of the chemiluminescence intensity ratio CO_2*/OH* with equivalence ratio. The CO_2* and OH* profiles were spatially integrated such that they correspond to a combustor residence time of 2-3 ms, which is characteristic of a number of low NOx combustors.

6.2.2.1.1 Effect of Pressure and Temperature

It can be seen in Figure 4.3 and Figure 4.8 that the variation of CO_2*/OH* ratio with equivalence ratio is similar for syngas flames at various operating conditions. In general, the CO_2*/OH* ratio remains nearly constant for $\phi>0.7$ and then steeply increases for very lean flames, i.e., $\phi<0.7$. This makes the CO_2*/OH* signal ratio of little use for sensing equivalence ratio, except perhaps at very lean conditions. This is further illustrated with simulations for a H_2:CO=50:50 mixture at different pressure and temperature conditions (Figure 6.15). The simulated ratios were scaled to the baseline atmospheric case for convenience. Again, the results in Figure 6.15 should be interpreted primarily in regard to their ϕ variation.* Nevertheless, the results clearly indicate that I_{CO_2*}/I_{OH*} would make a poor choice for sensing equivalence ratio in the range of pressures and temperatures considered.

---

*For example, the experimental data for a H_2:CO~33:67 mixture at ϕ=0.6 (Figure 4.8), show the I_{CO_2*}/I_{OH*} ratio increasing with pressure, unlike the simulations.

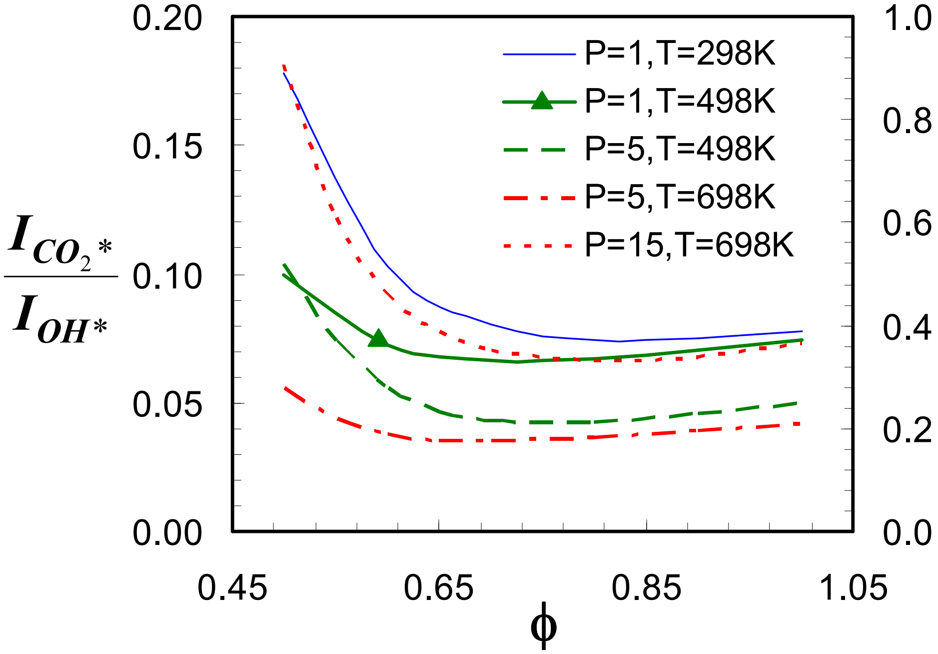

Figure 6.15. Variation of the CO_2*/OH* chemiluminescence ratio with equivalence ratio at various pressure and preheat conditions. The atmospheric results are scaled with the left axis; the rest of the data scale with the right axis.

6.2.2.2 Methane

In premixed methane flames, I_{CH*}/I_{OH*} has been shown to be a promising candidate for sensing equivalence ratio at various pressures [30].[*] As concluded in Chapter 5, the chemiluminescence models can be used to qualitatively predict the dependence of the CH*/OH* chemiluminescence intensity ratio with equivalence ratio. At atmospheric conditions, the computed $I_{\mathrm{CH*}}/I_{\mathrm{OH*}}$ values were scaled by a constant to match experimental validation data. This scaling constant is ~24 at room pressure and

---

[*] I_{CO_2*}/I_{OH*} results presented in Chapter 5 at atmospheric conditions show this ratio to be non-monotonic and only weakly sensitive to ϕ; thus it is not considered here.

temperature conditions in methane-air flames. However, at elevated pressure conditions (and with the He/O_2 oxidizer), this scaling constant was between 0.5 and 2.

6.2.2.2.1 Effect of Pressure and Temperature

In Chapter 5, the chemiluminescence intensity ratio I_{CH*}/I_{OH*} was seen to monotonically increase with equivalence ratio for atmospheric pressure conditions. However, the variation of I_{CH*}/I_{OH*} was not the same at elevated pressures. For example, it can be seen in Figure 5.14 that at 10 atm the ratio is decreasing, while at 5 atm it is closer to constant throughout the equivalence ratio range. Figure 6.16 provides further indication of this with simulation results at a range of pressure and temperature conditions for methane-air flames. The simulated chemiluminescence ratios are scaled with the C_{det} value determined from the baseline atmospheric results. At atmospheric pressure, $I_{\mathrm{CH*}}/I_{\mathrm{OH*}}$ monotonically increases as expected. At 5 atm, there is little change in $I_{\mathrm{CH*}}/I_{\mathrm{OH*}}$ with equivalence ratio (similar to what was observed in methane-He/O_2 flames), except for very lean conditions, i.e., $\phi<0.65$. This suggests that $I_{\mathrm{CH*}}/I_{\mathrm{OH*}}$ cannot be used for sensing equivalence ratio in some conditions. At even higher pressures (15 atm), $I_{\mathrm{CH*}}/I_{\mathrm{OH*}}$ again varies significantly with ϕ, now decreasing monotonically (again in agreement with the methane-He/O_2 validation experiments). According to Figure 6.16, pressure generally increases the magnitude of the $I_{\mathrm{CH*}}/I_{\mathrm{OH*}}$ ratio, at a given equivalence ratio, whereas the validation experiments indicated the opposite effect. Similarly, the models predict that preheating generally has a decreasing effect on the $I_{\mathrm{CH*}}/I_{\mathrm{OH*}}$ ratio, though the decrease is less than 20% for most of the cases considered. However, in the high pressure experiments, preheating produced an increase in $I_{\mathrm{CH*}}/I_{\mathrm{OH*}}$. In summary, $I_{\mathrm{CH*}}/I_{\mathrm{OH*}}$ can be used for sensing equivalence ratio only at certain conditions, and the changing relationship between I_{CH*}/I_{OH*} and ϕ with pressure must be taken into account. Such trends have been observed experimentally without reactant preheating [30].

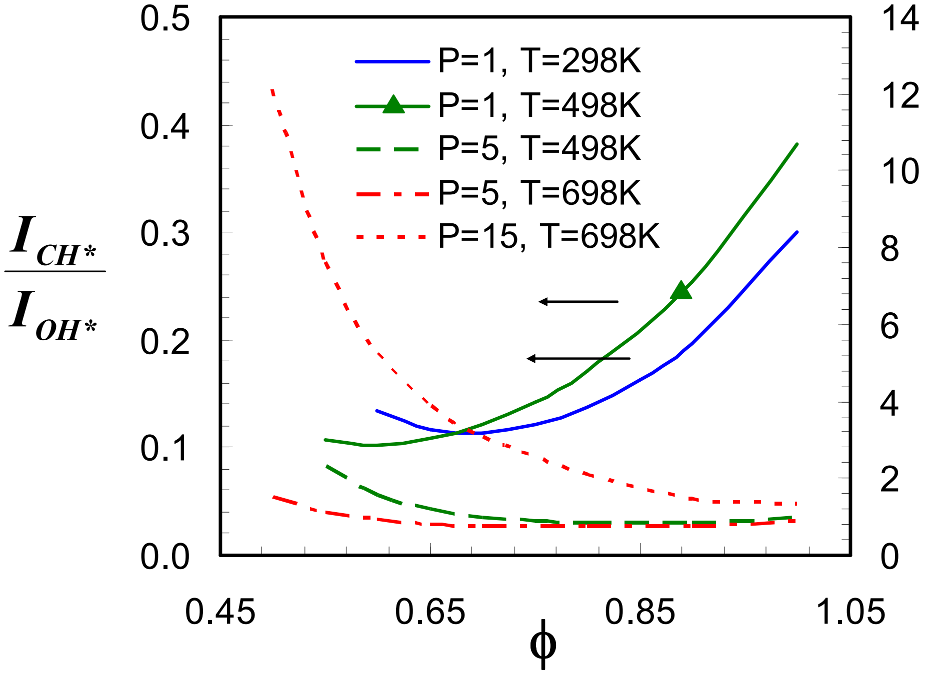

Figure 6.16. CH*/OH* chemiluminescence ratio in methane-air flames at various pressures and preheat; the high pressure results are scaled to the right axis.

6.2.2.2.2 *Effect of Aerodynamic Strain*

Results for I_{CH*}/I_{OH*} variations with strain rate are given in Figure 6.17 at ϕ=0.7 and 1. It was noted in Chapter 5 that CH* chemiluminescence is more dependent on strain than OH*. This is clearly evident here, where I_{CH*}/I_{OH*} increases with strain rate. For a given strain rate, the increase in I_{CH*}/I_{OH*} is almost the same for both equivalence ratios considered, except at high pressure. The maximum increase of 13% occurs at ambient pressure conditions, while for the higher pressure and preheat case, I_{CH*}/I_{OH*} ratio increases by 1% for the lean case and increases by about 10% for the stoichiometric case. However, with I_{CH*}/I_{OH*} varying by only 10% over a wide range of strain rates, it can be concluded that I_{CH*}/I_{OH*} is not very sensitive to strain rate. This is supported by the agreement between results in laminar and turbulent flames at atmospheric conditions presented in Chapter 5 for conditions away from the lean blow out limit of the swirl combustor.

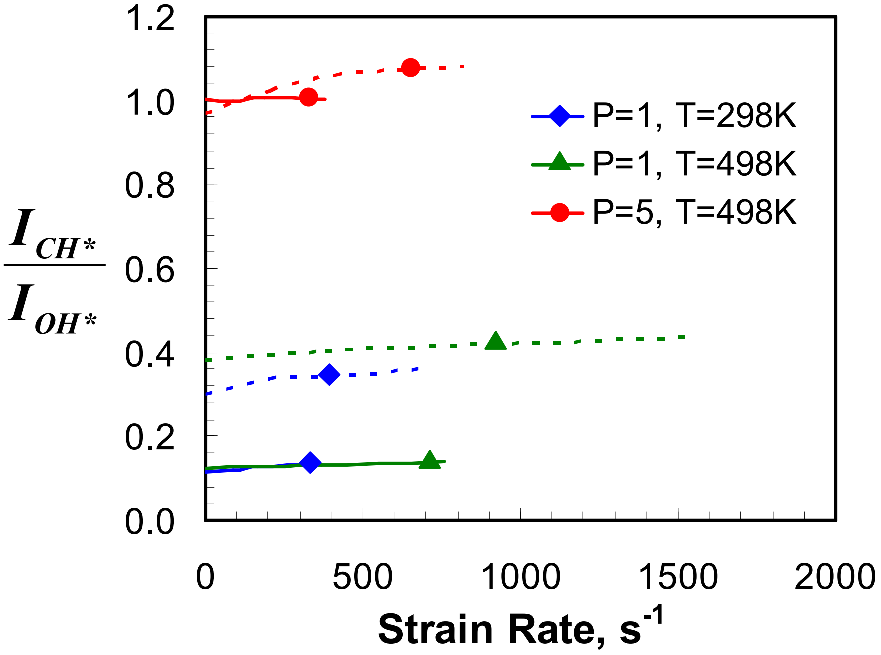

Figure 6.17. Dependence of CH*/OH* ratio with strain rate for ϕ=1 (dashed line) and ϕ =0.7 (solid line).

6.2.2.2.3 Effect of Exhaust Gas Recirculation

Results for I_{CH^*}/I_{OH^*} variation with product recirculation are shown for the same two equivalence ratios, 0.7 and 1. It was demonstrated above that the CH* signal increases with product recirculation while OH* signal is practically unaffected by it. It can be see that I_{CH^*}/I_{OH^*} increases with product recirculation. For ϕ=0.7 and 20% EGR, I_{CH^*}/I_{OH^*} increases by 27% at 5 atm and 498 K, while at 1 atm and for both 298 and 498 K reactant temperatures, the ratio increases more. Similar results are observed for the stoichiometric case. However, for lower levels of product mixing (EGR<5%), the effect on I_{CH^*}/I_{OH^*} is negligible.

6.3 Other Considerations

6.3.1 Thermal Excitation

As mentioned earlier, in addition to chemical formation of the excited states, thermal excitation can also occur. The contribution of thermal OH* and CH* emission for sensing is therefore analyzed here. The procedure for calculating the upper estimate of thermal OH* based on equilibrium calculations is already outlined (Chapters 4 and 5). That methodology along with the assumption that the formation reactions are accurate in predicting the absolute concentrations of OH* and CH* is used to estimate the thermal contributions in methane-air flames.

Table 6.5. Thermal OH* contribution (as percentage of the total OH* signal) in methane-air flames for different residence times and equivalence ratios.

Pressure and Temperature	**% Thermal OH for 2-3 ms**		**% Thermal OH for 10 ms**	
	$\phi = 0.7$	$\phi = 1.0$	$\phi = 0.7$	$\phi = 1.0$
1 atm, 298 K	0.01	0.43	0.035	2.63
1 atm, 498 K	0.08	1.62	0.30	8
5 atm, 498 K	0.51	12	2	29
5 atm, 698 K	3.1	23.7	10.9	39
15 atm, 698 K	11.5	38	28.7	46

Results for thermal OH* as a fraction of the total OH* emission for premixed methane flames are presented in Table 6.5. The thermal OH* is seen to be a function of residence time and the equivalence ratio of the combustor (as thermal OH* is formed primarily in the hottest regions). However, the thermal contribution to the total OH* signal also rises significantly with pressure.* Hence in high pressure combustors, especially combustors with long residence times and near stoichiometric conditions, the OH* emission has to be treated carefully.

Results for thermal CH* as a fraction of the total CH* for premixed methane-air flames are presented in Table 6.6. As CH and CH* exist primarily in the thin reaction zone for lean flames, a residence time of 2-3 ms was considered, which is more than sufficient to capture the complete reaction zone in all cases. It can be clearly seen that thermal CH* is practically negligible at these conditions, as expected. Thermal CH* may become important in oxy-methane flames [32].

Table 6.6. Thermal CH* contribution (as percentage of the total CH* signal) in methane-air flames.

Pressure and Temperature	**% Thermal CH for 2-3 ms**	
	$\phi = 0.7$	$\phi = 1.0$
1 atm, 298 K	0.006	0.06
1 atm, 498 K	0.012	0.08
5 atm, 498 K	0.007	0.13
5 atm, 698 K	0.02	0.19
15 atm, 698 K	0.012	0.24

6.3.2 OH* Self-Absorption

Example calculations are shown in Table 6.7 for the effect of self-absorption on OH* emission in methane-air combustion at various temperature and pressure conditions for a residence time of 2.5 ms. A conservative estimate of these values is computed using

---

[*] As described in a previous section, the chemical formation of OH*, normalized by heat release, decreases at high pressures.

Eq. (3) (Chapter 2) and peak absorbance coefficient is used for the R-branch bandhead of the OH (A-X) (0,0) transition without considering the line shapes/profiles. However, this calculation is useful to access the conditions in which self-absorption may be important. It can be seen that the impact of self-absorption can be important at elevated pressures and temperature conditions, particularly near stoichiometric equivalence ratios. It should be expected that self-absorption would increase with the simulated residence time of the combustor (which is used here to determine the emission path length). So, it would be wise to place the sensor/detector on the reactants side of the flame.

Table 6.7. Fraction of OH* signal absorbed in methane-air flames at different pressure and temperature conditions.

Methane/Air Flames	**% Absorption (t=2.5ms)**	
	$\phi = 1.0$	**$\phi = 0.7$**
1atm-300K	7	1
1atm-500K	11	3.7
5atm,-500K	18	3.2
5atm-700K	34	11
15atm-700K	39	13

6.3.3 CO_2* Background

In most sensing and combustion diagnostic applications, flame chemiluminescence is acquired with spectral filters placed in front of detectors such as photomultiplier tubes, photodiodes or CCD cameras. At best (e.g., for interference filters), their bandpass is ±5-10 nm about the center wavelength. It is also well known that CO_2* background is present in the 200-600 nm region [55]. Thus, it underlies the other (OH* and CH*) emission signals. So unless a spectrometer or additional detector is used to monitor the CO_2* background, its contribution can not be removed from the detected signal. Thus it is interesting to estimate the contribution of the CO_2* background to the total signal at OH* and CH* wavelengths. For this purpose, the resolved flame spectra from the swirl-stabilized methane combustor at atmospheric pressure and laminar CH_4-O_2/He flames at elevated pressure are analyzed to study the CO_2* background. The OH* signal, S_{OH*}, was found by integrating the (0,0) band over a 5 nm bandwidth centered at the OH* peak (~309 nm). The CH* signal, S_{CH*}, was found by integrating the 430 nm CH band over a bandwidth of 5 nm. The CO_2* background over the same 5 nm bandwidths was approximated by the means of a cubic polynomial. The area under this polynomial was taken as the estimate for the CO_2* background. Results for atmospheric swirl flame and laminar flames at elevated pressure are shown in Figure 6.18.

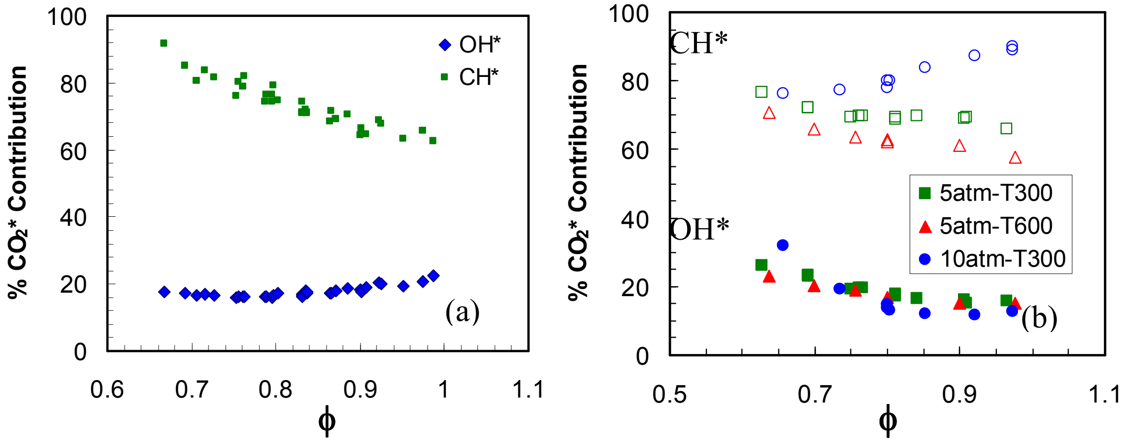

Figure 6.18. CO_2* contribution in methane flames to OH*(309±5nm) and CH* (431±5nm) signals; (a) atmospheric pressure and (b) elevated pressure.

It is evident that the CO_2* background affects the CH* signal more than the OH* signal. For example at $\phi=0.8$ at atmospheric conditions, only 30% of the total signal at the CH* wavelength is from CH* chemiluminescence, while OH* chemiluminescence makes up 80% of its total signal. Moreover, the CO_2* background has a weaker equivalence ratio dependence for OH* chemiluminescence than for CH*. At elevated pressures, this dependence is reduced for CH* too, but interestingly the CO_2* background increases with ϕ at 10atm. Another interesting aspect is to consider the variation of chemiluminescence intensity ratio with equivalence ratio, which has a direct bearing on ϕ sensing. It can be seen in Figure 6.19 that the background corrected S_{CH*}/S_{OH*} has a higher sensitivity, i.e., it varies by a factor of ten in the ϕ range considered. Whereas, S_{CH*}/S_{OH*} without background correction only varies by a factor of two. So, a sensor based on the background corrected ratios would be more sensitive to changes in ϕ. The high pressure experimental data also support this fact. Moreover, S_{CH*}/S_{OH*} is almost constant near the lean blow out regime of the swirl combustor if background correction is not considered and as such cannot be used to sense the proximity of the combustor to lean blow off..

It is possible, though, that the uncorrected normalized signals could have a different ϕ dependence which might make them more advantageous to use for heat release sensing than the background corrected normalized chemiluminescence signals. To verify this possibility, both background corrected and uncorrected signals are considered for OH* and CH* in Figure 6.20. The uncorrected signals are multiplied by a single multiplier so as to minimize the least square difference between the two signals. As seen in Figure 6.20a, there is practically no difference in the ϕ dependence for the OH* signal without background correction. However for CH* chemiluminescence, failing to correct for the background at 10 atm increases the systematic error for heat release sensing associated with ϕ changes (Figure 6.20b).

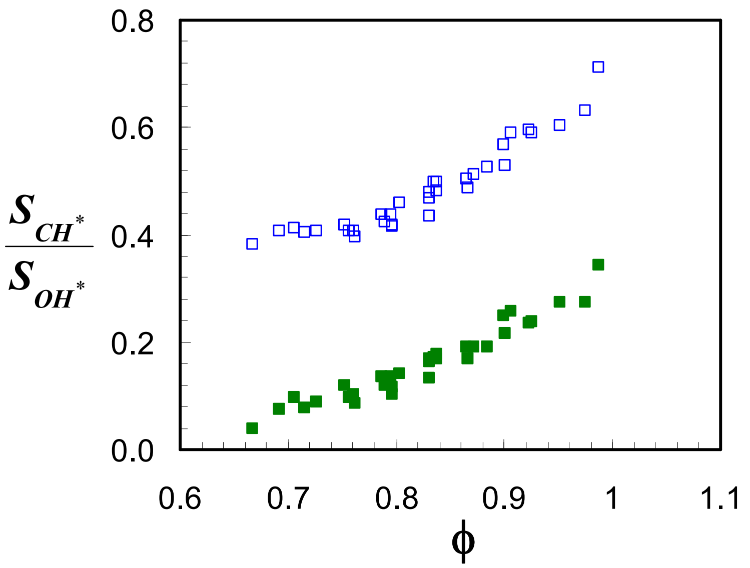

Figure 6.19. Comparison of chemiluminescence intensity ratio for CH* and OH*: with background correction (closed symbols); without background correction (open symbols).

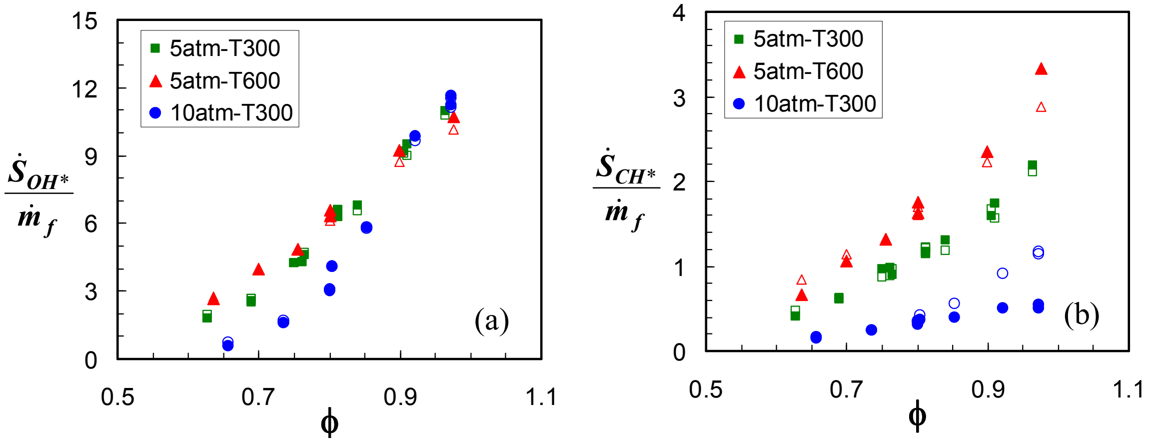

Figure 6.20. Variation of normalized (a) OH* and (b) CH* chemiluminescence signals at elevated pressure conditions. Background corrected signals (closed symbols) and uncorrected signals (open symbols).

CHAPTER 7

CONCLUSIONS AND RECOMMENDATIONS

7.1 Summary and Conclusions

The primary objective of this thesis was to identify and validate existing chemiluminescence mechanisms for OH*, CH* and CO_2* for combustion conditions. This involved a comparison of experimental data with simulation results based on the different mechanisms. Systematically acquiring global (spatially integrated) OH*, CH* and CO_2* chemiluminescence data from simple laminar premixed flames formed the main focus of the experimental investigation. Experiments were carried out for a range of operating conditions, including variations in pressure, reactant preheat temperature, equivalence ratio (ϕ), dilution, and fuel composition: H_2-CO syngas mixtures, methane and Jet-A; to test the robustness of the chemiluminescence mechanisms. Detailed numerical simulations for unstrained, 1-d laminar flames were performed with leading chemical kinetic mechanisms relevant to the above fuels. The spatially resolved simulation results were integrated to provide a comparison to the experimental data. Laminar flames were used in part to provide a meaningful comparison between the experiments and simulations. Global chemiluminescence intensity ratios and global chemiluminescence signals normalized with fuel mass flow rate were used for validating the chemiluminescence mechanisms.

For CO_2* chemiluminescence, a global reaction rate was derived, based on the spectral data of Slack *et al.* [55], for the photon emission rate at 375 nm, which is given by the following.

$$i'_{CO_2^*} = 3.3(\pm 0.3) \times 10^3 \exp[\frac{-2300K}{T}][CO][O] \frac{mol}{cm^3 \cdot s \cdot nm}$$

This model produced excellent agreement with the experimental data for syngas (both atmospheric and high pressure) and methane (atmospheric) flames. While this mechanism produced the correct variation with equivalence ratio at high pressure, it did not produce the correct scaling for a given ϕ with pressure. This is attributed to inaccuracies in the basic chemical reaction mechanism used in the high pressure simulations, as well as signal loss due to radiative trapping (by species such as CO_2 and H_2O). For the Jet-A flames and high pressure methane flames, the CO_2* background at 375 nm had significant interferences from other emitters, possibly HCO and water.

Two OH* formation reactions were found to be needed to accurately predict the validation results. R1 (O+H+M) is the dominant formation reaction in H_2 systems and in the post-flame product gases of hydrocarbon flames, while R3 (CH+O_2) dominates in the reaction zone for hydrocarbon fuels. The rate constants for both reactions are summarized in Table 7.1. The temperature dependence for k_1 was chosen to be the expression given in [37] as it provided the best results in the syngas tests. The pre-exponential factor given is based on the range of k_1 values reported in the literature. The k_3 temperature dependence determined from the atmospheric methane-air and Jet-A flame validations is the expression given in [45]. From comparison of the atmospheric syngas and methane results, the ratio k_1/k_3 was estimated, and used to determine the pre-exponential factor for k_3 shown in Table 7.1. This mechanism was able to accurately predict OH* chemiluminescence variations with equivalence ratio and pressure, but failed to correctly model the influence of reactant preheating (at least in the high pressure methane flames studied). Possible sources for this discrepancy include radiative trapping of the OH* emission and the formation of OH* via thermal excitation in the high pressure conditions.

For CH*, two formation reactions, R6 (C_2H+O) and R7 (C_2H+O_2), were sufficient to predict the experimental data in the lean flames studied here. Two sets of rate constants (attributed to Peeters [64] and Carl [66]) performed well in the methane and Jet-A validations, and both are reported in Table 7.1. Both predicted the equivalence ratio and preheat dependence, though the Peeters rate constants performed better for very lean atmospheric conditions, while the Carl rates provides a better match at high pressure. However, both failed to capture the pressure dependence, which might be due to the lack of accurate quenching data or inaccuracies in the basic reaction mechanism for estimating the precursor species (e.g., C_2H). Because CH* is formed from C_2H, it is only produced

Table 7.1. Validate formation reactions and rate constants for OH* and CH* chemiluminescence. Rate coefficients are expressed as $k = A\ T^b \exp(-E_a/RT)$ with E_a in units of cal mol^{-1} and AT^b in cm^{3}mol^{-1}s^{-1} for two body reactions or cm^{6}mol^{-2}s^{-1} for three body reactions (with T in K units).

#	Reaction	*A*	*b*	E_a
OH*				
R1	$H + O + M \leftrightarrow OH^* + M$	$4.3(\pm1.7) \times 10^{14}$	0.0	6940
R3	$CH + O_2 \leftrightarrow OH^* + CO$	$8.3(\pm3.4) \times 10^{13}$	-0.4	4150
CH* (Peeters)				
R6	$C_2H + O \leftrightarrow CH^* + CO$	$1.08(\pm0.4) \times 10^{13}$	0	0
R7	$C_2H + O_2 \leftrightarrow CH^* + CO_2$	$2.17(\pm0.8) \times 10^{10}$	0	0
CH* (Carl)				
R6	$C_2H + O \leftrightarrow CH^* + CO$	$6.02(\pm3.0) \times 10^{12}$	0	457
R7	$C_2H + O_2 \leftrightarrow CH^* + CO_2$	6.02×10^{-4}	4.4	-2285

in the reaction zone (at least for lean flames). Moreover, thermal excitation of CH* was negligible for the experimental conditions.

With the validated chemiluminescence mechanisms, there is now a way to analyze the fundamental behavior of chemiluminescence in combustion systems. Therefore, the second objective of this thesis was to use the simulation (and experimental) results to evaluate chemiluminescence for sensing heat release and equivalence ratio at various operating conditions. The influences of pressure, reactant preheat, strain and (adiabatic) exhaust gas recirculation were studied for a syngas fuel (H_2:CO=50:50) and for methane. Even though laminar flame data and simulations were used to analyze chemiluminescence sensing, the excellent agreement between the laminar methane and turbulent swirl flame experiments suggests that the findings reported here have relevance to many practical combustor systems. For highly turbulent combustors where questions regarding the validity of flamelet approaches arise, the validated mechanisms can be incorporated into detailed turbulence simulations (incorporating appropriate detailed chemistry) in order to study chemiluminescence in those systems.

In the syngas mixture, both the normalized OH* and CO_2* signals vary significantly with equivalence ratio, which implies that neither are ideal for heat release sensing. The simulations indicate that both product recirculation and aerodynamic strain rate do not have any significant effect on either OH* or CO_2* chemiluminescence signals at high pressure and temperature conditions. With respect to heat release rate sensing in syngas fuels, CO_2* appears to be a better option at very lean equivalence ratio conditions ($\phi < 0.7$), as it has the least sensitivity to equivalence ratio, pressure and temperature changes. At near stoichiometric conditions, OH* would be a better heat release marker as it is less sensitive to ϕ variations at these conditions. The chemiluminescence intensity ratio CO_2^*/OH^* would be of little use for sensing equivalence ratio in syngas combustion, except perhaps at very lean conditions.

In methane-air flames, the normalized OH* signal is a strong function of equivalence ratio, as in the syngas case, and hence not ideal for heat release sensing. Pressure in general, decreases the normalized OH* signal over the entire ϕ range, with the decrease more pronounced for leaner mixtures. The simulations indicate that reactant preheating increases the normalized OH* signal throughout the equivalence ratio range, though this was not observed in the experiments. For CH*, the ϕ dependence is reduced at high pressure, unlike OH*, which is consistent with the experimental observations. Reactant preheating also increases the CH* chemiluminescence normalized by the heat release. Also, the normalized CH* signal decreases with an increase in pressure. Both normalized OH* and CH* signals increase with strain rate at atmospheric conditions, but are practically independent of strain rate at high pressure and preheat conditions. Product recirculation has practically no effect on the normalized OH* signal but the normalized CH* signal increases by as much as 50% for a 20% EGR at an equivalence ratio of 0.7. These results suggest that CH* is better suited for high pressure applications of heat release sensing compared to OH*, but the current experimental results in methane-O_2/He flames show that preheating has a weaker effect on I_{OH^*}/q compared to I_{CH^*}/q.

The CH*/OH* ratio can be used for equivalence ratio sensing only at certain conditions in methane combustion as this ratio can change from monotonically increasing (at atmospheric conditions) to monotonically decreasing (at very high pressure), with an intermediate pressure region that shows little sensitivity to ϕ. Strain rate has a negligible effect on the chemiluminescence intensity ratio, while %EGR was shown to increase the magnitude of the CH*/OH* ratio.

The contribution of thermally produced OH* to the overall OH* signal was also calculated based on equilibrium conditions for methane systems. It was found that the thermal pathway is not very significant at atmospheric and intermediate pressures, but it becomes increasingly important at high pressures with large residence times and near stoichiometric conditions. On the other hand, thermal CH* is practically negligible even at high pressure and high temperature conditions. The conditions favorable for thermal OH* production are also favorable for OH* self absorption. So, a sensor placed on the reactant side of the combustor will be less prone to errors due to radiative trapping. Still, the OH* signal should be carefully interpreted in high pressure systems with long optical path lengths.

The contribution of CO_2^* background to the total signal at the OH* and CH* wavelengths was studied for methane. For the conditions considered, the CO_2^* background made up only a small fraction (~20%) of the total OH* signal, but contributed as much as 70-90% of the nominal CH* signal. The uncorrected normalized OH* and CH* chemiluminescence signals do not offer any advantage for heat release sensing applications. Similarly, the background corrected S_{CH*}/S_{OH*} ratio has a higher sensitivity to ϕ compared to measurements without background correction. Thus, it is advisable to use background corrected OH* and CH* signals for sensing purposes.

For very high pressure combustion, such as in gas turbines (20-50 atm) and rockets (70 atm and higher), the signal per unit heat release drastically decreases with pressure. This might be an issue, especially for CH*, if background corrected signals are not used. For OH*, self-absorption and thermal excitation may become increasingly significant. Moreover, OH* would be produced predominantly in the product gases rather than the reaction zone (where most of the heat release happens) and hence, may not be useful for sensing heat release at these conditions.

7.2 Recommendations for Future Work

For chemiluminescence modeling to be applicable for a wide range of operating conditions, it is necessary for the mechanisms to be robust and well-validated. There is still some ambiguity in choosing the CH* chemiluminescence mechanism as both the very different Peeters and Carl rate constants produce excellent agreement with the experimental data for most of the conditions. As it is necessary to identify the correct rate constants, more experiments should be carried out, preferably in flames that have a different $[O]/[O_2]$ distribution compared to atmospheric methane-air flames. To select one of the two mechanisms will require experiments at elevated pressures, or possibly with a different oxidizer. For example, simulation results for normalized CH* in methane flames with an equimolar mixture of O_2-N_2 as oxidizer are shown in Figure 7.1. The simulations with Carl and Peeters mechanisms were scaled by the same constants that were used for matching the atmospheric experimental data in methane-air flames. It can be seen that these conditions clearly differentiate the mechanisms especially for the near-stoichiometric equivalence ratios.

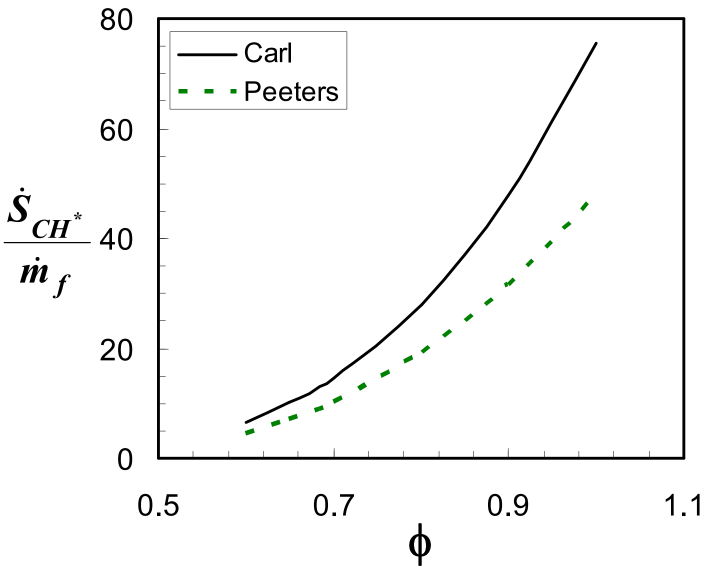

Figure 7.1. Normalized CH* chemiluminescence in oxy-methane flames at atmospheric pressure and temperature. Suggested approach for differentiating CH* chemiluminescence mechanisms. Oxidizer is an equi-molar mixture of O_2 and N_2.

Most of the data presented in this work at elevated pressure and temperatures was preliminary and more extensive investigation has to be undertaken to understand various issues affecting the flame chemiluminescence at these conditions and the inability of chemiluminescence mechanisms to predict the experimental results quantitatively. The reason may lie in the failure to accurately model the relative affects of the following processes: thermal excitation, radiative trapping and collisional quenching of the excited species. However, accurately estimating the concentration profiles of the relevant precursor species is also very important. Therefore, more data at different pressure and temperature conditions would aid in further understanding of these issues.

To apply chemiluminescence modeling to realistic combustors, it is necessary to understand the dependence of chemiluminescence on the degree of turbulence. So, more experiments have to be performed in turbulent flames.

Very limited chemiluminescence data is presented for laminar premixed prevaporized Jet-A flames, in this thesis. Jet-A fuel being very relevant in aero-propulsion devices demands further investigation. More experiments should be performed at different conditions to validate the OH* and CH* chemiluminescence mechanisms as well as the basic chemistry for Jet-A combustion. Whether, the mechanisms provide good agreement or not, these experiments will provide valuable chemiluminescence data for Jet-A flames at various operating conditions that can be investigated for ϕ and heat release sensing applications.

C_2* is another prominent emitter in rich methane flames and for higher order hydrocarbon fuels in the UV-VIS region of the electromagnetic spectrum. The chemiluminescence intensity ratio C_2*/OH* and C_2*/CH* has been shown previously to be useful for equivalence ratio sensing in hydrocarbon flames (see Appendix A). However, most of the experimental investigation was carried out in methane flames at atmospheric conditions. There exists a need to study C_2* chemiluminescence for ϕ and heat release sensing at different operating conditions and in liquid fuels of interest such as Jet-A. Additionally, little progress has been made in modeling C_2* chemiluminescence in flames and currently only one low pressure flame study has suggested a complete C_2* mechanism [82]. However, the mechanism has huge uncertainties and needs to be validated further.

APPENDIX A

C_2* BACKGROUND

The blue green Swan band emission system is typically found in hydrocarbon flames and is also of great interest in astrophysics as it is part of the emission spectra from comets and deep space [1]. C_2 kinetics are responsible for the production of C_2H, which in turn is an important precursor for the formation of excited CH ($A^2\Delta$) species. The following reactions are identified as the possible formation reactions:

$$CH + CH \rightarrow C_2^* + H_2 \qquad (R8)$$

$$C + CH \rightarrow C_2^* + H \qquad (R9)$$

$$C + CH_2 \rightarrow C_2^* + H_2 \qquad (R10)$$

$$C_3 + O \rightarrow C_2^* + CO \qquad (R11)$$

$$C + C_2O \rightarrow C_2^* + CO \qquad (R12)$$

R8 has been ruled out in flames [83]. A shock heated methane study favors R9 and R10 [84]. A flow discharge study in $C_2H_2/O/H$ system confirms R10 as the main production step [61]. R11 and R12 are also reported to occur [85, 86]. The quenching rate information of the excited C_2 species is not well known and is limited to some noble gases and simple species such as Ar, H, H_2, O_2 etc [87]. Recently, collisional cross-sections for collisional quenching of $C_2(d^3\Pi)$ by n-alkanes (n=1-8) were measured at room temperature and low pressure (15 torr) conditions [88].

Though the Swan band system was extensively investigated, very little progress has been made in the development of a C_2 chemiluminescence mechanism, modeling the formation and destruction kinetics of the excited C_2 radical. In a recent laser-induced fluorescence study, collisional quenching rates of the excited state $C_2(d^3\Pi)$ were derived based on the measured fluorescence decay rates, which were then used to deduce the rate constants for the excited state $C_2(d^3\Pi)$ formation reactions from low pressure flame studies [82]. Rate constants for R10 and R11 were determined along with an estimation of the overall quenching rate. However, there is significant uncertainty in the rates of these reactions. This study also estimated the reaction rate parameters for important reactions of C_3, C_3H, C_3H_2 and C_2O along with the addition of C and C_2 chemistry to GRI Mech 3.0 mechanism. However, further improvements for the C_2* kinetics are needed to model C_2* chemiluminescence accurately.

The chemiluminescence intensity ratio C_2*/CH* and C_2*/OH* can be used to sense equivalence ratio in liquid and gaseous systems with the ratio C_2*/OH* observed to be more sensitive to changes in ϕ [89]. However, a recent study in counterflow premixed natural-gas flames indicates that C_2*/CH* is strongly affected by strain rate and may not be suitable for sensing equivalence ratio [24]. Likewise, if the normalized C_2* chemiluminescence signal variation with ϕ was considered, it was shown that C_2* would be more advantageous than OH* or CH* for sensing heat release rate for lean conditions at room pressure and temperature conditions [24]. Most of the C_2* chemiluminescence results are confined to atmospheric methane flames. Experimental data for C_2* chemiluminescence is severely lacking at elevated pressure and preheat conditions.

APPENDIX B

SPECTRAL RESPONSIVITY

Spectral responsivity of the spectrometer, ICCD camera system was estimated based on intensity measurements from a calibrated Oriel^{TM} QTH 1000W FEL tungsten halogen light source. The calibration of the light source is accurate to within ±15%. Acton Spectra-Pro 300i spectrometer with 300 grooves/mm grating (500 nm blaze angle) coupled with a 16-bit, 1024×256 intensified CCD camera (PI-MAX, 25 mm intensifier) constitutes the detection system. A fiber optic array consisting of four bundles, each bundle having three 200μm fused silica fibers with a numerical aperture of 0.22 was connected to the entrance slit of the spectrometer. The optical fibers have negligible transmission losses (~1-3%) in the UV-VIS wavelength region of interest (300-500 nm). The slit width of the spectrometer was set to 100 μm. The intensifier gain was set to 80 and the exposure time was 10 μs. Flatfield function for each fiber bundle was also measured as part of this study using a 632.8 nm He-Ne laser and moving the spectrometer grating such that the He-Ne laser peak traversed across the horizontal pixel range (32-952). The pixels 1-31 and 953-1024 were ignored as they are very close to the edge of the CCD chip. It should be noted that the flatfield function is only dependent on the spatial location of the detector pixel and not on wavelength. Moreover, for each fiber, a rectangular region of 1024×50 pixels was binned vertically to form one composite strip (1024×1). The flatfield function and the spectral responsivity of the system were estimated for this composite strip. So, for a given incident beam with energy $E_{o,\lambda}$, the spectrometer-ICCD camera would output a beam with energy is given by

$$\frac{E_\lambda}{E_{o,\lambda}} = FF(x)SR(\lambda)\,. \tag{23}$$

where, FF(x) is the absolute flatfield function which only depends on the spatial location of the beam image on the detector and SR(λ) is the absolute spectral responsivity of the system. However, the flatfield function was estimated relative to the center pixel i.e. pixel 512 for each fiber and similarly spectral responsivity of the system was estimated relative to that at 407nm. Theoretical spectral responsivity (TSR) was also calculated based on the nominal quantum efficiency of the ICCD camera and the typical efficiency of the spectrometer grating (both obtained from the manufacturer). TSR is the product of these efficiencies either based on photon (intensity) or power (energy) units. It can be seen in Figure B.1 that the normalized experimental and theoretical spectral responsivity values (based on power) have a reasonable agreement. It can be observed that the spectral responsivity can change by a factor of 2 at most from ~300 nm (OH* chemiluminescence) to ~430 nm (CH* chemiluminescence).

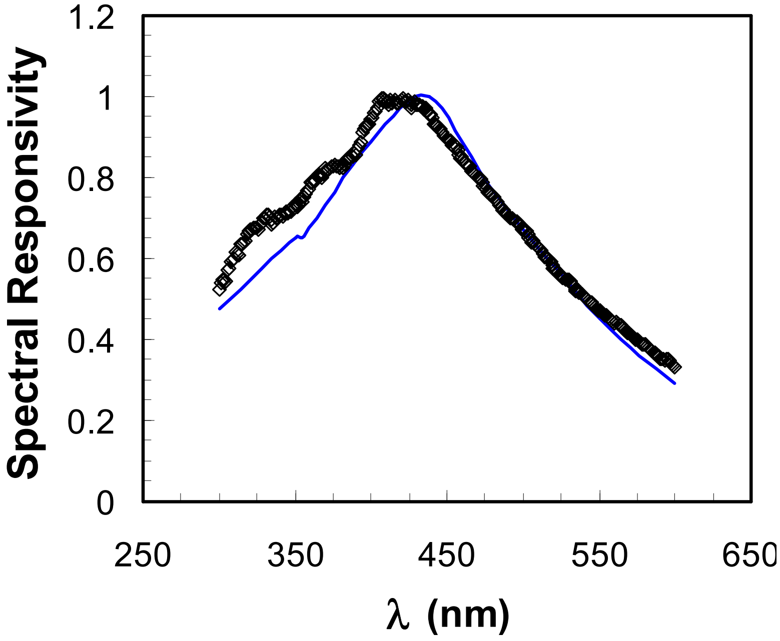

Figure B.1. Relative spectral responsivity of the spectrometer-ICCD camera detector system. Theoretical (lines); Experiments (symbols).

REFERENCES

1 Gaydon, A. G. and Wolfhard, H. G., "Flames: Their Structure, Radiation, and Temperature," Fourth edition, Chapman and Hall, 1978.

2 Stojkovic, B. D., Fansler, T. D., Drake, M. C. and Sick, V., "High-speed imaging of OH* and soot temperature and concentration in a stratified-charge direct-injection gasoline engine," *Proceedings of the Combustion Institute*, vol. 30, pp. 2657-2665, 2005.

3 Schefer, R. W., "Flame sheet imaging using CH chemiluminescence," *Combustion Science and Technology*, vol. 126 (1-6), pp. 255-270, 1997.

4 Muruganandam, T. M., Kim, B.-H., Morrell, M. R., Nori, V., Patel, M., Romig B. W. and Seitzman, J. M., "Optical equivalence ratio sensors for gas turbine combustors," *Proceedings of the Combustion Institute*, vol. 30, pp. 1601-1609, 2005.

5 Lee, J. G., Kim, K. and Santavicca, D. A., "Measurement of equivalence ratio fluctuation and its effect in heat release during unstable combustion," *Proceedings of the Combustion Institute*, vol. 28, pp. 415-421, 2000.

6 Luque, J., Jeffries, J. B., Smith, G. P., Crosley, D. R., Walsh, K. T., Long, M. B. and Smooke, M. D., "CH(A-X) and OH(A-X) optical emission in an axisymmetric laminar diffusion flame," *Combustion and Flame*, vol. 122, pp.172-175, 2000.

7 Smith, G. P., Luque, J., Park, C., Jeffries, J. B. and Crosley, D. R., "Low pressure flame determinations of rate constants for OH(A) and CH(A) chemiluminescence," *Combustion and Flame*, vol. 131 (1-2), pp. 59-69, 2002.

8 Kojima, J., Ikeda, Y. and Nakajima, T., "Basic aspects of OH(A), CH(A), and C_2(d) chemiluminescence in the reaction zone of laminar methane-air premixed flames," *Combustion and Flame*, vol. 140, pp. 34-45, 2005.

9 Haber, L. C., Vandsburger, U.,. Saunders, W, R. and Khanna, V. K., "An examination of the relationship between chemiluminescent light emissions and heat

release rate under non-adiabatic conditions," *Proceedings of International Gas Turbine Institute*, 2000.

10 Samaniego, J. M., Egolfopoulos, F. N. and Bowman, C. T., "CO_2* chemiluminescence in premixed flames," *Combustion Science and Technology*, vol. 109, pp. 183-203, 1995.

11 Gaydon, A. G. and Wolfhard, H. G., "Comparison of the spectra of turbulent and laminar flames," *Fuel*, vol. 33 (3), pp. 286-290, 1954.

12 John, R. R., Wilson, E. S. and Summerfield, M., "Studies of the mechanism of flame stabilization by a spectral intensity method," *Jet Propulsion*, vol. 25 (10), pp. 535-537, 1955.

13 Clark, T. P., "Studies of OH, CO, CH and C_2 radiation from laminar and turbulent propane-air and ethylene-air flames*,"* *NACA TN 4266*, 1958.

14 Kojima, J., Ikeda, Y. and Nakajima, T., "Spatially resolved measurement of OH*, CH* and C_2* chemiluminescence in the reaction zone of laminar methane/air premixed flames", *Proceedings of the Combustion Institute*, vol. 28, pp. 1757-1764, 2000.

15 Docquier, N., Lacas, F. and Candel, S., "Closed-loop equivalence ratio control of premixed combustion using spectrally resolved chemiluminescence measurements", *Proceedings of the Combustion Institute*, vol. 29, pp 139-145, 2002.

16 Yamazaki, M., Ohya, M. and Tsuchiya, K. *Int. Chem. Eng.* vol. 30, pp. 160-168, 1992.

17 Brown, M. S., Meyer, T. R., Sturgess, G. J., Zelina, J. and Gord, J. R., "Chemiluminescence as a measurement of local equivalence ratio," *AIAA 2002-3865, 38th AIAA/ASME/SAE/ASEE Joint Propulsion Conference and Exhibit*, July 2002.

18 Cheng, T.S., Wu, C. –Y., Li, Y. –H. and Chao, Y.-C., "Chemiluminescence measurements of local equivalence ratio in a partially premixed flame," *Combustion Science and Technology*, vol. 178 (10-11), pp. 1821-1841, 2006.

19 Higgins, B., McQuay, M. Q., Lacas, F., Rolon, J. C., Darabiha, N. and Candel, S. "Systematic measurements of OH chemiluminescence for fuel-lean, high-pressure, premixed, laminar flames," *Fuel*, 80, pp. 67-74, 2001.

20 Price, R., Hurle, I. and Sugden, T., "Optical studies of the generation of noise in turbulent flames," *Proceedings of the Combustion Institute*, vol. 12, pp. 1093-1102, 1968.

21 Hurle, I., Price, R., Sugden, T. and Thomas, A., "Sound emission from open turblent premixed flames," *Proceedings of the Royal Society of London-Series A*, vol. 303, pp. 409-427, 1968.

22 aschereit, C., Gutmark, E. and Weisenstein, W., "Excitation of thermoacoustic instabilities by the interaction of acoustics and unstable swirling flow," *AIAA Journal*, vol. 45 (4), pp. 108-117, 1998.

23 Bloxsidge, G., Dowling, A. and Langhorne, P., "Reheat buzz: an acoustically coupled combustion instability. part 2. theory," *Journal of Fluid Mechanics*, vol. 193, pp. 445-473, 1988

24 Hardalupas, Y. and Orain, M., "Local measurements of the time-dependent heat release rate and equivalence ratio using chemiluminescent emission from a flame," *Combustion and Flame*, vol. 139 (3), pp.188-207, 2004.

25 Hardalupas, Y., Panaoutsos, C. S. and Taylor, A. M. K. P., "Heat release rate measurements in premixed flames using chemiluminescence and reaction rate imaging," *AIAA 2006-1450, 44th AIAA Aerospace Sciences Meeting and Exhibit*, 2006.

26 Najm, H., Paul, P., Mueller, C. and Wyckoff, P., "On the adequacy of certain experimental observables as measurements of flame burning rate," *Combustion and Flame*, vol. 113, pp. 312-332, 1998.

27 Ayoola, B. O., Balachandran, R., Frank, J. H., Mastorakos, E. and Kaminski, C. F., "Spatially resolved heat release measurements in turbulent premixed flames," *Combustion and Flame*, vol. 144, pp. 1-16, 2006.

28 Lee, J. G. and Santavicca, D. A., "Experimental diagnostics for the study of combustion instabilities in lean premixed combustors," *Journal of Propulsion and Power*, 19 (5), pp. 735-750, 2003.

29 Bellows, B. D., Zhang, Q., Neumeier, Y., Lieuwen, T. and Zinn, B. T.,"Forced response studies of a premixed flame to flow disturbances in a gas turbine combustor," *AIAA Paper 2005-1164*, Jan. 2005.

30 Higgins, B., McQuay, M. Q., Lacas, F. and Candel, S., "An experimental study on the effect of pressure and strain rate on CH chemiluminescence of premixed fuel-lean methane/air flames," *Fuel*, vol. 80 (11), 1583-1591, 2001.

31 Docquier, N., Belhafaoui, S., Lacas, F., Darabiha, N. and Rolon, J-C., "Experimental and numerical study of chemiluminescence in methane/air high-pressure flames for active control applications," *Proceedings of the Combustion Institute*, vol. 28, pp. 1765-1774, 2000.

32 De Leo, M., Saveliev, A., Kennedy, L.A., and Zelepouga, S. A., "OH and CH luminescence in opposed flow methane oxy-flames," *Combustion and Flame*, vol. 149, pp. 435-447, 2007.

33 Carrington, T., "Electronic quenching of OH ($^2\Sigma^+$) in flames and its significance in the interpretation of rotational relaxation," *Journal of Chemical Physics*, vol. 30 (4), pp. 1087-1095, 1959.

34 Kaskan, W. E., "Abnormal excitation of OH in $H_2/O_2/N_2$ flames," *Journal of Chemical Physics*, vol. 31 (4), pp. 944-956, 1959.

35 Belles, F. E. and Lauver, M. R., "Origin of OH chemiluminescence during the Induction Period of the H_2-O_2 reaction behind shock waves," *Journal of Chemical Physics*, vol. 40 (2), pp.415-417, 1964.

36 Hidaka, Y., Takahashi, S., Kawano, H., Suga, M., and Gardiner, W. C. Jr., "Shock-tube measurement of the rate constant for excited OH ($A^2\Sigma^+$) formation in the hydrogen-oxygen reaction," *Journal of Physical Chemistry*, vol. 86 (8), pp. 1429-1433, 1982.

37 Petersen E. L. and Kalitan, D. M., "Calibration and chemical kinetics modeling of an oh chemiluminescence diagnostic," *AIAA 2003-4493*, *39th AIAA/ASME/SAE/ASEE Joint Propulsion Conference and Exhibit*, Huntsville, Alabama, July 2003.

38 Tamura, M.; Berg, P. A., Harrington, J. E., Luque, J., Jeffries, J. B., Smith, G. P. and Crosley, D. R., "Collisional quenching of CH(A), OH(A), and NO(A) in low pressure hydrocarbon flames," *Combustion and Flame*, vol. 144, pp. 502-514, 1998.

39 Gutman, D., Lutz, R. W., Jacobs, N. F. and Hardwidge, E. A., "Shock-tube study of OH chemiluminescence in the hydrogen-oxygen reaction," *The Journal of Chemical Physics*, vol. 48 (12), pp. 5689-5694, 1968.

40 Smith, G. P., Park, C. and Luque, J., "A Note on chemiluminescence in low-pressure hydrogen and methane-nitrous oxide flames," *Combustion and Flame*, vol. 140, pp. 385-389, 2005.

41 Krishnamahari, S. and Broida, H., "Effect of molecular oxygen on the emission spectra of atomic oxygen-acetylene flames," *The Journal of Chemical Physics*, vol. 34 (5), pp. 1709-1711, 1961.

42 Becker, K., Kley, D. and Norstrom, R., "OH chemiluminescence in hydrocarbon atom Flames," *Proceedings of the Combustion Institute*, vol.14, pp 405-411, 1977.

43 Dandy, D. and Vosen, S., "Numerical and experimental studies of hydroxyl radical chemiluminescence in methane-air flames," *Combustion Science and Technology*, vol. 82, pp. 131-150, 1992.

44 Carl, S. A., Poppel, V. M. and Peeters, J., "Identification of the $CH + O_2 \rightarrow OH$ (A) + CO reaction as the source of OH(A-X) chemiluminescence in $C_2H_2/O/H/O_2$ atomic flames and determination of its absolute rate constant over the range T = 296 to 511 K", *Journal of Physical Chemistry A*, vol. 107, pp. 11001-11007, 2003.

45 Hall, J. M. and Petersen, E. L., “An optimized kinetics model for oh chemiluminescence at high temperatures and atmospheric pressures,” *International Journal of Chemical Kinetics*, vol. 38 (12), pp. 714-724, 2006.

46 Lester, M. I., Loomis, R. A., Schwartz, B. L. and Walch, S. P., “Electronic quenching of OH A (2) Sigma (+) (v' = 0, 1) in complexes with hydrogen and nitrogen,” *Journal of Physical Chemistry A*, vol. 101, p. 9195, 1997.

47 Anderson, D. T., Todd, M. W. and Lester, M. I. J., “Reactive quenching of electronically excited OH radicals in collisions with molecular hydrogen,” *Chemical Physics*, vol. 110, p. 11117, 1999.

48 Dempsey, L. P., Murray, C. and Lestera, M. I., “Product branching between reactive and nonreactive pathways in the collisional quenching of OH($A^2\Sigma^+$) radicals by H_2,” *J. Chemical Physics*, vol. 127 (15), p. 151101, 2007.

49 Singla, G., Scouflaire, P., Rolon, C. and Candel, S., “Planar laser-induced flouroscence of OH in high-pressure cryogenic LO_x/GH_2 jet flames,” *Combustion and Flame*, 144, pp. 151-169, 2006.

50 Davidson, D. F., Roehrig, M., Petersen, E. L., Di Rosa, M. D. and Hanson, R. K., “Measurements of the OH *A-X* (0,0) 306 nm absorption bandhead at 60atm and 1735K,” *Journal of Quantitative Spectroscopy and Radiative Transfer*, vol. 55 (6), pp. 755-762, 1996.

51 Schulz, C., Jeffries, J. B., Davidson, D. F., Koch, J. D., Wolfrum, J. and Hanson, R. K., “Impact of UV absorption by CO_2 and H_2O on NO LIF in high-pressure combustion applications,” *Proceedings of the Combustion Institute*, vol. 29, pp. 2735-2742, 2002.

52 Okabe, H., “The Photochemistry of Small Molecules,” John Wiley and Sons, New York, 1978.

53 Baulch, D. L., Drysdale, D. D., Duxbury, J. and Grant, S. J., “Evaluated Kinetic Data for High Temperature Reactions,” Vol. 3, Butterworths, London, 1976.

54 Pravilov, A. M. and Smirnova, L. G., "Temperature-dependence of the spectral distribution of the rate-constant of chemiluminescence in the reaction $O(^3P)+CO \rightarrow CO_2+h\nu$," *Kinetics and Catalysis*, vol. 22 (4), pp. 832-838, 1981.

55 Slack, M. and Grillo, A., "High-temperature rate coefficient measurements of CO + O chemiluminescence*,"* *Combustion and Flame*, vol. 59 (2), pp. 189-196, 1985.

56 Myers, B. F. and Bartle, E. R., "Shock-tube study of the radiative processes in systems containing atomic oxygen and carbon monoxide at high temperature," *The Journal of Chemical Physics*, vol. 47 (5), pp. 1783, 1967.

57 Vaidya, W. M., "Isotope effect in hydrocarbon flame bands (deuterium substitution)," *Proceedings of the Royal Society of London-Series A*, vol. 279 (137) pp.572-581, 1964.

58 Padley, P. J., "The origin of the blue continuum in the hydrogen flame," *Transactions of the Faraday Society*, vol. 56, pp. 449-454, 1960.

59 Vanpee, M. and Mainiero, R.J., "Spectral distribution of the blue hydrogen flame continuum and its origin in hydrogen-nitric oxide flames," *Combustion and Flame*, vol. 34, pp. 219-230, 1979.

60 Brenig, H. H., Ph.D. Thesis, Wuppertal, 1981.

61 Grebe, J. and Homann, K. H., "Kinetics of the species $OH(A^2\Sigma^+)$, $OH(X^2\Pi)$ and $CH(X^2\Pi)$ in the system C_2H_2-O-H," *Ber. Bunsenges. Phys. Chem*. vol. 86, pp. 581-587, 1982.

62 Glass, G. P., Kistiakowsky, G. B., Michael, J. V. and Niki, H., *Proceedings of the Combustion Institute*, vol. 10, pp. 513-522, 1965.

63 Hall, J. M., De Vries, J., Amadio, A. R. and Petersen, E.L., "Towards a kinetics model of CH chemiluminescence," *AIAA Paper 2005-1318*, *43rd AIAA Aerospace Sciences Meeting and Exhibit*, Reno, Nevada, 2005.

64 Devriendt, K., Van Look, H., Ceursters, B. and Peeters, J., "Kinetics of formation of chemiluminescent CH($A^2\Delta$) by the elementary reactions of $C_2H(X^2\Sigma^+)$ with O (P-3) and O_2 ($X^3\Sigma^{g-}$): A pulse laser photolysis study," *Chemical Physics Letters*, vol. 261 pp. 450-456, 1996.

65 Renlund, A. M., Shokoohi, F., Reisler, H. and Wittig, C. J., "Reaction of C_2H with O_2 - chemi-luminescent products," *Journal of Physical Chemistry*, vol 86 (21), pp. 4165-4170, 1982.

66 Elsamra, R. M. I., Vranckx, S. and Carl, S. A., "CH($A^2\Delta$) formation in hydrocarbon combustion: the temperature dependence of the rate constant of the reaction $C_2H+O_2 \rightarrow CH(A^2\Delta)+CO_2$," *Journal of Physical Chemistry*., **109,** 2005, pp. 10287-10293.

67 Chen, C., Wang, F., Chen, Y. and Ma, X., "Temperature effect on quenching of CH($A^2\Delta$)," *Chemical Physics*, vol. 230, pp. 317-325, 1998.

68 Garland, N. L. and Crosley, D. R., "Collisional quenching of CH A^2-Δ,v'=0 at 1300 K, *Chemical Physics Letters*, vol. 134, pp. 189-194, 1987.

69 Renfro, M. W., Venkatesan, K. K. and Laurendeau, N, M., "Cross sections for quenching of CH ($A^2\Delta$, v'=0, by N_2 and H_2O from 1740 to 2160 K," *Proceedings of the Combustion Institute*, vol. 29, pp. 2695-2702, 2002.

70 Becker, K. H., Engelhardt, B., Geiger, H., Kurtenbach, R. and Wiesen, P., "Temperature-dependence of the reactions of CH radicals with NO, NH_3 and N_2O in the range 200-1300-K," *Chemical Physics Letters*, 210, 1993, p. 135.

71 Natarajan, J., Lieuwen, T. and Seitzman, J., "Laminar flame speeds of H_2/CO mixtures: effect of CO_2 dilution, preheat temperature and pressure," *Combustion and Flame*, vol. 151, pp. 104-119, 2007.

72 Natarajan, J., Kochar, Y., T. Lieuwen and J. Seitzman, "Laminar flame speed measurements of $H_2/CO/CO_2$ mixtures up to 15 atm and 600 K preheat temperature," *GT2008-51364, ASME Turbo Expo 2008: Power for Land, Sea and Air*, Berlin, Germany.

73 Sun, H. Y., Yang, S. I., Jomass, G., and Law, C. K., "High pressure laminar flame speeds and kinetic modeling of carbon monoxide/hydrogen combustion." *Proceedings of the Combustion Institute*. vol. 31, pp. 439-446, 2006.

74 Smith, G. P., Golden, D. M., Frenklach, M., Moriarty, N. W., Eiteneer, B., Goldenberg, M., C. T. Bowman, C. T., Hanson, R. K., Song, S., Gardiner, W. C. Jr., Lissianski, V. V., Qin, X., http://www.me.berkeley.edu/gri_mech/mech/

75 Li, J., Zhao, Z., Kazakov, A., Chaos, M., Dryer, F. L. and Scire Jr, J. J., "A Comprehensive kinetic mechanism for CO, CH_2O, and CH_3OH combustion." *Int. J. Chem. Kin.,* vol. 39 (3), pp. 109-136, 2007.

76 "Chemical-Kinetic Mechanisms for Combustion Applications, San Diego Mechanism web page", Mechanical and Aerospace Engineering (Combustion Research), University of California at San Diego. http://maeweb.ucsd.edu/~combustion/cermech/

77 Elliott, L., Ingham, D. B., Kyne, A. G., Mera, N. S., Pourkashanian, M. and Wilson, C. W., "A novel approach to mechanism reduction optimisation for aviation fuel/air reaction mechanism using a genetic algorithm," *Paper GT2004-53053, Proceedings of the ASME Turbo Expo*, Vienna, Austria, 2004.

78 Bowman, C. T., *Proceedings of the Combustion Institute*, vol. 15, p.869, 1975.

79 Ladommatos, N., Abdelhalim, S. M., Zhao, H. and Hu. Z., "The effects of carbon dioxide in exhaust gas recirculation on diesel engine emissions," *Proceedings of the Institution of Mechanical Engineers, Part D-Journal of Automobile Engineering*, vol. 212 (D1), pp. 25-42, 1998.

80 Abd-Alla, G. H., "Using exhuast gas recirculation in internal combustion engines: a review," *Energy Conversion and Management*, vol. 43 (8), pp. 1027-1042, 2002.

81 Zheng, M., Reader, G. T. and Hawley, J. G., "Diesel engine exhaust gas recirculation - a review on advanced and novel concepts," *Energy Conversion and Management*, vol. 45 (6), pp. 883-900, 2004.

82 Smith, G. P., Park, C., Schneiderman, J. and Luque, J., "C_2 swan band laser-induced fluorescence and chemiluminescence in low-pressure hydrocarbon flames," *Combustion and Flame*, vol. 141, pp. 66-77, 2005.

83 Bulewicz, E. M., Padley, P. J. and Smith. R. E., "Spectroscopic studies of C_2, CH and OH radicals in low pressure acetylene+oxygen flames," *Proceedings of the Royal Society of London-Series A*," vol. 135, pp.129-148, 1970.

84 Bowman, C. T. and Seery, D. J., "Chemiluminescence in high-temperature oxidation of methane," *Combustion and Flame*, vol. 12, pp. 611-614, 1968.

85 Savadatti, M. I. and Broida, H. P., "Spectral study of flames of carbon vapor at low pressure," *Journal of Chemical Physics*, vol. 45 (7), pp. 2390-2396, 1966.

86 Kunz, C., Harteck, P. and Dondes, S., "Mechanism for excitation of c2 high-pressure bands $C+C_2O \rightarrow C_2(A^3\Pi)+CO$," *Journal of Chemical Physics*, vol. 67 (10), pp. 4157-4158, 1967.

87 Luque, J., Juchmann, W. and Jeffries, J. B., "Spatial density distributions of C_2, C_3, and CH radicals by laser-induced fluorescence in a diamond depositing dc-arcjet," *Journal of Applied Physics*, vol. 82 (5), pp. 2072-2081, 1997.

88 Wang, H. L., Zhu, Z. Q., Zhang, S. H., Pei, L. S. and Chen, Y., "Time-resolved kinetic studies on quenching of C_2 ($d^3\Pi_g$) by alkanes and substituted methane molecules," *Chemical Physics Letters*, vol. 407, pp. 217-221, 2005.

89 Morrell, R., Seitzman, J., Wilensky, M., Lee, J., Lubarsky, E. and Zinn, B., "Interpretation of optical flame emissions for sensors in liquid-fueled combustors," *paper AIAA-2001-0787, 39th AIAA Aerospace Sciences Meeting*, Reno, NV, 2001.